

NLO Corrections and Parton Shower Effects on Electroweak Higgs Production in Association with Two Jets

Dissertation

der Mathematisch-Naturwissenschaftlichen Fakultät
der Eberhard Karls Universität Tübingen
zur Erlangung des Grades eines
Doktors der Naturwissenschaften
(Dr. rer. nat.)

vorgelegt von

Johannes Scheller
aus Kassel

Tübingen
2022

Gedruckt mit Genehmigung der Mathematisch-Naturwissenschaftlichen Fakultät der
Eberhard Karls Universität Tübingen.

Tag der mündlichen Qualifikation:	06.02.2023
Dekan:	Prof. Dr. Thilo Stehle
1. Berichterstatterin:	Prof. Dr. Barbara Jäger
2. Berichterstatter:	Prof. Dr. Werner Vogelsang
3. Berichterstatter:	Prof. Dr. Robert Harlander

Zusammenfassung

Nach dem großen Erfolg, den die Entdeckung des Higgs-Bosons im Jahr 2012 für die Teilchenphysik darstellte, konzentriert sich die Forschung in diesem Fachgebiet mittlerweile darauf, das Standardmodell der Teilchenphysik mit höchster Präzision zu testen. Dahinter steht unter anderem die Hoffnung, Aussagen darüber treffen zu können, ob das Standardmodell tatsächlich als die fundamentale Theorie der Teilchenphysik anzusehen ist oder ob ihm eine umfassendere Theorie zugrunde liegt, die auch neue Physik jenseits dieses Modells beschreibt.

Besonderer Fokus liegt in der aktuellen Forschung auf den verschiedenen Produktionsprozessen des Higgs-Bosons. Im Rahmen dieser Dissertation wird einer dieser Prozesse untersucht, namentlich die elektroschwache Produktion des Higgs-Bosons in Assoziation mit zwei harten Jets. Dieser Prozess zeichnet sich einerseits durch seine klare experimentelle Signatur aus und gilt andererseits als besonders sensitiv gegenüber den Effekten neuer Physik. Zentraler Bestandteil der Untersuchung in dieser Dissertation ist eine Rechnung, die Korrekturen in der nächstführenden Ordnung sowohl der starken, als auch der elektroschwachen Kopplung berücksichtigen kann. Diese Rechnung wird als Nutzerprozess im frei verfügbaren Programm POWHEG BOX RES implementiert. Durch den POWHEG-Formalismus wird eine Verknüpfung der Matrixelemente für den harten Streuprozess mit einem sogenannten Partonschauer ermöglicht, welcher die Berechnung von exklusiven Observablen erlaubt, die besonders für den Vergleich mit experimentellen Analysen große Relevanz besitzen.

Die in dieser Arbeit präsentierte Implementierung stellt in Bezug auf den wichtigen Subprozess der Vektorbosonfusion (VBF) die erste frei verfügbare Rechnung in nächstführender Ordnung der elektroschwachen Kopplung dar, die mit einem QED-Schauer kombiniert werden kann. Gleichzeitig verzichten wir auf die weit verbreitete "VBF-Näherung", in der nur dieser Subprozess betrachtet wird und der Subprozess der Higgsstrahlung vernachlässigt wird. Der Verzicht auf diese Näherung erlaubt es uns, Vorhersagen in einem deutlich weiter gefassten Bereich des Phasenraums mit hoher Präzision zu treffen.

Unsere neue Implementierung ermöglicht es, praktisch beliebige kinematische Verteilungen des Prozesses zu generieren. Beispielhaft werden in dieser Arbeit einige dieser Verteilungen präsentiert und diskutiert. Dabei zeigt sich, dass wir in der Lage sind, bekannte Ergebnisse in nächstführender Ordnung der starken Kopplung und mit Partonschauer zu reproduzieren. Darüber hinaus unterstreichen die Ergebnisse die Wichtigkeit der Korrekturen in der nächstführenden Ordnung der elektroschwachen Kopplung, während sich Effekte durch einen QED-Schauer als vergleichsweise gering herausstellen.

Abstract

While every particle predicted by the Standard Model of particle physics has been observed since the Higgs boson was finally discovered in 2012, researchers in the field continue to test the predictions by this very successful theory with enormous precision. Their hope is to be able to determine whether the Standard Model is actually the fundamental theory of the elementary particles, or whether it is part of a more comprehensive theory.

Since its discovery, the properties of the Higgs boson and its various production channels have drawn special attention in the scientific community. This thesis focusses on one of these production modes, namely the electroweak production of a Higgs boson in association with two hard jets. This process is known for its high signal-to-background ratio and is expected to be particularly sensitive to the effects of new physics beyond the Standard Model. We present an implementation of this process in the publicly available framework of the `POWHEG BOX RES`. This implementation includes corrections at the next-to-leading order of both the strong as well as the electroweak coupling and can be matched to a so-called parton shower, therefore allowing for the calculation of exclusive distributions that can be compared to experimental results.

Regarding the sub-process of vector boson fusion (VBF), we present the first calculation that allows for the matching of a parton shower with a precision calculation at the next-to-leading order of the electroweak coupling. Furthermore, we do not rely on the widely used VBF approximation, which neglects contributions corresponding to the sub-process of Higgsstrahlung. We are thus able to perform precision calculations in a significantly larger part of the phase space than previous implementations in the `POWHEG` framework that were limited to the VBF approximation.

Using our new implementation, one can calculate arbitrary kinematic distributions of the final state particles. In this thesis, this is demonstrated by a phenomenological study featuring selected important distributions. We thereby not only confirm the ability of our code to reproduce existing results at the next-to-leading order of the strong coupling, but we are also able to show the importance of corrections at next-to-leading order of the electroweak coupling. In contrast, the influence of a QED shower turns out to have only a mild influence.

List of Corresponding Publications

- [1] B. Jäger, A. Karlberg, S. Plätzer, J. Scheller and M. Zaro, *Parton-shower effects in Higgs production via Vector-Boson Fusion*, *Eur. Phys. J. C* **80** (2020) 756 [2003.12435].
- [2] B. Jäger and J. Scheller, *Electroweak corrections and shower effects to Higgs production in association with two jets at the LHC*, *JHEP* **09** (2022) 191 [2208.00013].

Contents

1	Introduction	1
2	The Standard Model (and Beyond)	7
2.1	Quantum Field Theory and the Standard Model of Particle Physics . . .	7
2.2	Limitations of the SM and BSM Physics	9
2.3	The Electroweak Sector and the Higgs Mechanism	11
3	From QFT to Precision Calculations	18
3.1	Cross Sections	19
3.1.1	A Few Words about Non-Perturbative QCD	20
3.2	NLO Corrections	25
3.2.1	Ultraviolet Divergences And Renormalisation	27
3.2.2	Infrared Divergences	32
3.3	Parton Showers	37
3.3.1	The POWHEG Method	41
4	The EW Hjj Production Process	45
5	Implementation	53
5.1	The POWHEG-BOX-RES	53
5.1.1	The Treatment of Resonances	56
5.1.2	EW Corrections and the POWHEG-BOX-RES	57
5.1.3	The Matching and Vetoing Procedure	58
5.2	RECOLA	59
5.3	Tests	60
6	Phenomenology	62
6.1	Setup	62
6.2	Numerical Results	66
7	Conclusions and Outlook	89
A	Installing and Compiling the Code	92

B Input Parameters	94
C List of Abbreviations	98

Chapter 1

Introduction

Dass ich erkenne, was die Welt
im Innersten zusammenhält

Johann Wolfgang von Goethe: *Faust –
eine Tragödie* [3].

Among the great questions that humanity has been eager to answer since the early days of philosophy are at least¹ two that are directly linked to contemporary particle physics: *What is our universe made of, what are the basic building blocks of matter?*, and *What are the elementary forces between the constituents of matter?* – or, to put it with Goethe’s words: *‘Whatever holds the world together in its inmost folds?’* [3].

The concept of small particles as basic building blocks of matter has been around for at least several thousand years. Even though such particles would remain a highly theoretical concept for millenia, the Greek philosopher Democritus coined the word *átomos*, meaning ‘uncuttable’, for the smallest components of matter in the 5th century BCE. His basic idea – all matter is made of solid, indivisible particles of different kinds – would remain the common doctrine for thousands of years, even though the models of atomic theory were updated several times (e.g. Dalton, 1808 [4]). The first hint to the fact that atoms might actually not be the most basic constituents of matter was the discovery of the electron by J. J. Thomson in 1897 [5], which led to his famous *plum pudding model* (1904 [6]). In the 20th century, the model of the atom was revised several times (Rutherford, 1911 [7]; Bohr, 1913 [8]; Sommerfeld, 1916 [9]), accounting for new theoretical concepts and experimental findings. As a result, the idea of the atom being the fundamental particle was overcome.

Nevertheless, other particles, partly being constituents of the atom themselves, took over its role. While the introduction of quantum mechanics has shaken the very concept of particles to its foundations and also blurred the border between matter and interactions,

¹There are a lot of questions from the field of philosophy that, if one takes a closer look, resemble the key research questions of today’s particle physicists. For example, the big question of how our universe evolved, especially in the very beginning, not only concerns cosmology, but is also subject to particle physics, to only name one more.

we still assume the existence of point-like, indivisible *elementary particles* in contemporary particle physics.

Today, the basic constituents of every kind of matter that we encounter in our day-to-day life² and three of the four fundamental forces between them can be described by the *Standard Model* (SM) of particle physics. This theoretical model was developed in the second half of the 20th century, starting with the first non-Abelian gauge theory for the strong interactions by Yang and Mills (1954) [10]. Many more important milestones mark its development, among them the unification of electromagnetic and weak interactions (Glashow, 1961 [11]) and the incorporation of the Higgs mechanism³ in the theory of electroweak interactions by Steven Weinberg and Abdus Salam (1967/1968) [16, 17]. The success of the SM is not only a theoretical one, but manifests itself in numerous experiments which confirm the theoretical predictions to a very high degree of precision. The SM has been widely accepted since several decades and is considered to be complete since the existence of quarks was experimentally confirmed in the 1970s. The latest, spectacular success of the SM was the discovery of a new particle by the two experiments ATLAS [18] and CMS [19] at the CERN Large Hadron Collider (LHC) in 2012, which seems to possess all the properties of the Higgs boson as predicted by the SM, thus confirming the Higgs mechanism.

Never before has humankind been able to describe the structure of matter and elementary forces so precisely, making the SM one of the most tested and most successful theories in the whole field of physics. But while fundamental research and the hunt for answers to the very basic theoretical, even philosophical questions are still driving researchers all over the world, contemporary particle physics has not only shaped our understanding of the universe, but also led to inventions which have a very practical use in everyone's daily life. Among those innovations, important developments such as radiation therapy in medicine or the world wide web (which was developed by Tim Berners-Lee at CERN in 1991) have their origins in – or would at least not have been possible without – particle physics.

For several years, the focus of researchers in elementary particle physics has been shifting from trying to confirm the SM to stress testing it and to finding its limitations. While the SM as a theoretical model is self-consistent and its predictions have not been disproved yet, there are a few phenomena in particle physics that cannot be explained by the SM. Among them are the existence of dark matter in the universe or the non-vanishing masses of neutrinos, to name only a few. Moreover, it has some features that are often regarded as ‘unaesthetic’ from a theoretical point of view. All of this has

²One of the main drawbacks of the Standard Model is that it fails to describe more ‘exotic’ matter and energy, namely Dark Matter and Dark Energy. This fact is a key motivation for the search for new physics, which will be dealt with in Sec. 2.2.

³This mechanism, described in some detail in Sec. 2.3, was developed and published by three independent research groups almost at the same time [12, 13, 14, 15] whose contributions should not remain unnamed. The mechanism is therefore sometimes called Englert-Brout-Higgs-Guralnik-Hagen-Kibble mechanism or even Anderson-Brout-Englert-Guralnik-Hagen-Higgs-Kibble-’t Hooft (ABEGHHK’tH) mechanism, but I will stick to the more common term Higgs mechanism throughout this work for reasons of brevity and readability.

motivated researchers to find evidence for new physics beyond the SM (BSM), described by new, often more comprehensive, theories. Popular representatives of these are for example *string theory* and *supersymmetry* (SUSY). So far, none of these theories were able to replace the SM. The common challenge for all these theories is trying to explain effects not included in the SM, while at the same time having to reproduce all of its confirmed predictions. Most theories overcome this apparent contradiction by assuming the SM to be the ‘low-energy limit’ of these respective theories. Nevertheless, if they are investigated with sufficient precision or at higher energies, all BSM theories must naturally lead to different predictions than the SM.

Independent of the aim – be it the confirmation of the SM or contradicting it –, research in particle physics must be performed with a very high degree of precision nowadays. Thanks to decades of research, many parameters of the SM have been determined with a very high accuracy, and experimental observables can be predicted and measured to equally high precision. This requires even more accuracy for future experiments and calculations, no matter if they aim at refining parameters within the SM or at finding deviations between experimental results and theoretical predictions, possibly disproving the SM. On the experimental side, particle colliders (both lepton and hadron colliders) of enormous size with equally impressive particle detectors are one state-of-the-art technique to reach this goal. The LHC with a circumference of ~ 27 km at the CERN research site in Geneva is the largest and might as well be the most famous collider, and already several proposals for a – possibly even larger – successor are discussed in the scientific community. On the theory side, several complementary approaches are used to reach the required level of accuracy, e.g. lattice gauge theory and perturbation theory. The different approaches all have their advantages and disadvantages and are often used for different purposes. For example, perturbative calculations of cross sections of a hard scattering process at fixed order are an ideal tool for testing theoretical predictions by the SM at high precision. On the other hand, exclusive experimental observables are often calculated with the help of parton shower generators, computer programs designed for the detailed simulation of the final states of hadronic collisions. To get the best out of both worlds, the two approaches can even be combined, as it will also be done in this work.

All the aforementioned approaches have in common that they quickly lead to complex mathematical expressions that need to be evaluated, e.g. complicated phase space integrals. In most cases, these expressions cannot be calculated analytically, let alone by hand. Usually, numerical calculations on powerful computers, often based on pseudo-random numbers (‘Monte Carlo methods’), are employed. The increase in energy and luminosity of hadron colliders over the last decades and the accompanying growth in both the multiplicity of observed final states, but also in experimental precision, led to a need for more and more complex (numerical) calculations on the theoretical side. For the case of fixed order perturbative calculations, for example, the need for higher precision automatically meant that higher and higher orders in perturbation theory had to be considered. While a few years ago most relevant processes had only been calculated at next-to-leading order (NLO) of quantum chromodynamics (QCD), state of the art

calculations often include next-to-next-to-leading order (NNLO) or even higher order QCD corrections. But while traditionally a higher degree of precision in perturbative calculations was very often equivalent to a higher order in QCD, other corrections have become more relevant lately. For example, higher order corrections in the electroweak (EW) sector now play a crucial role for many processes under consideration in modern high energy physics (HEP). Since the relevant coupling for this sector, α , is roughly one order of magnitude smaller than the coupling of QCD, α_s , a naive estimate already shows that NLO-EW corrections are of similar magnitude than the NNLO corrections of QCD. In reality, certain kinematic configurations in some processes can even lead to much more pronounced effects by the EW corrections, comparable in size to NLO-QCD corrections.

Many BSM theories share the proposition of changes to the electroweak symmetry breaking and the Higgs sector of the SM. Therefore, the discovery of a particle compatible with the SM Higgs boson in 2012 opened up an important possibility to search for the effects of new physics, sometimes dubbed the *Higgs window to New Physics* [20, 21]. Since this sector is so sensitive to the influence of BSM physics, it is one of the most promising areas of contemporary particle physics. For this reason, the exact properties of the Higgs boson, e.g. its couplings to other particles, are of uttermost scientific interest and need careful and precise investigation. While in the first time after the Higgs boson's discovery, research focussed mostly on its dominant production mode via gluon fusion, the increase in luminosity of the LHC also brought other production channels to the centre of attention, amongst them the electroweak production of a Higgs boson in association with two hadronic jets. This class of processes consists of two sub-processes, vector boson fusion (VBF) and Higgsstrahlung (HV) processes, which are sometimes considered separately, but which both show great sensitivity to the exact form of the Higgs boson's couplings to the EW gauge bosons and therefore to EW symmetry breaking in general.

Even though they have a relatively short record of experimental evidence, the various electroweak production modes of a Higgs boson with two or more jets have been the subject of many theoretical studies. These span from fixed order calculation in NLO-QCD [22, 23, 24] and their implementations in Monte-Carlo generators [25, 26, 27] to NNLO-QCD calculations [28, 29, 30, 31, 32, 33, 34, 35, 36, 37, 38, 39] and even higher order corrections in QCD [40, 41]. These calculations are complemented by studies on the NLO-EW corrections to the process [42, 43, 44, 45, 46], which have also been implemented in Monte Carlo tools [47]. In part, the NLO calculations have been matched to a parton shower (PS), as it is the case for the NLO-QCD calculation of the VBF channel [48, 49, 50] and of the HV channel [51], for which even an NLO+PS implementation including EW corrections exists [52].

So, while both the NLO-EW corrections to VBF, as well as an implementation combining NLO-QCD corrections and a (QCD) PS for this process exist, no implementation combining the NLO-EW corrections with a QED parton shower has been published so far. This gap is even more striking considering that VBF is one of the processes in which the effects of EW corrections are especially pronounced for certain kinematic configurations due to so called Sudakov logarithms.

This work intends to close this gap. We developed an implementation [2] of the

electroweak production mode of a Higgs boson in association with two jets, including both the NLO-EW and the NLO-QCD corrections within the public program `POWHEG BOX` [53]. This program makes use of the `POWHEG` framework [54, 55], allowing to interface NLO calculations with a PS in a consistent manner. Our implementation is thus able to generate events at NLO-QCD or NLO-EW accuracy in the Les Houches event (LHE) format that can then be showered with any appropriate PS generator like `PYTHIA` [56]. It can also be used as a stand-alone generator for fixed-order calculations on the Born level or including either NLO-EW or NLO-QCD corrections. At the same time, our implementation is the first at NLO+PS accuracy that includes the full EW production of the Hjj final state and is not limited to either the production via vector boson fusion or Higgsstrahlung.

I will begin this thesis with an introduction to quantum field theory in general and the contemporary Standard Model of particle physics in particular in Chap. 2. The focus of said chapter will be on two aspects, namely on the electroweak sector of the Standard Model and the Higgs mechanism of electroweak symmetry breaking, and on the motivation to test the Standard Model with elaborate precision calculations and experiments.

In the next chapter, I will continue this thesis by showing how we can use perturbative precision calculations to derive theoretical predictions for observables that can be directly compared to experimental results. In particular, I will explain how cross sections for scattering processes at hadron collider facilities are computed, how higher order corrections are used for their improvement, and how non-perturbative effects enter into the calculation of these hadronic cross sections. In the same chapter, I will also briefly sketch why divergences can appear in the high- and low-energy limits of a perturbative calculation and how they can be treated in a systematic way. As a complement to fixed-order calculations, I will introduce the framework of parton shower Monte Carlo generators. In particular, I will introduce the so-called `POWHEG` method to combine parton showers with precision calculations at the next-to-leading order.

The exact definition and the properties of the electroweak production processes of the Hjj final state will be presented in Chap. 4. There I will put a strong emphasis on the motivation to examine this particular process, and how an implementation matching next-to-leading order calculations and a parton shower can be used to close a gap in the research concerning this process.

The actual implementation of our calculation in the framework of the `POWHEG BOX RES` will be presented in Chap. 5, where the structure of the `POWHEG BOX` is introduced and it is explained how the implementation of the process at hand differs from ordinary processes due to the higher order electroweak corrections and the involved structure of the phase space. I will also briefly introduce the external programs that our code is or can be interfaced with and that are used for some parts of the calculation. The chapter will be concluded with a description of the extensive tests that we performed on our code to validate its results and performance.

Finally, I will present numerical results generated with the newly developed tool in Chap. 6.2. These results will cover both the calculations with corrections of higher order in

the strong and the electroweak coupling, combined with parton showers. I will show how our code is able to reproduce effects that have been observed with existing calculations, as well as I will present results based on the new features of our implementation.

In the final chapter, I will summarise the results of the phenomenological study, draw conclusions from the findings and suggest possible approaches for future research based on our implementation and beyond. I will conclude by evaluating how our implementation has helped to fill the research gap that it was designed for.

Chapter 2

The Standard Model (and Beyond)

In this chapter, I will very briefly introduce the formalism of quantum field theory in general and the Standard Model (SM) of particle physics in particular in section 2.1. After showing some of the limitations of the SM and thus motivating the need for precision tests of its predictions in section 2.2, I will then put a special emphasis on the sector of this model that describes the electroweak interactions and the Higgs mechanism in section 2.3. In that context, I will also briefly explain why the Higgs boson and the electroweak sector are of particular interest when testing the SM.

2.1 Quantum Field Theory and the Standard Model of Particle Physics

For decades, the mathematical formalism to describe the dynamics of elementary particles and their interactions has been the framework of *quantum field theory* (QFT). It can be regarded as the combination of classical field theory, quantum mechanics and (special) relativity. QFT can be motivated by combining the central requirements of both quantum mechanics – the commutation relations between operators – and of special relativity, i.e. the invariance of the theory under Lorentz transformations. Historically, it turned out that it is not possible to formulate a consistent, relativistic theory of one-particle quantum mechanics. Instead, a consistent formalism has to offer the possibility to account for the generation and annihilation of particles. This is the case in QFT, where particles are described as excitations of fields. In contrast to classical field theory, which had been known since the 19th century and had proven to be very successful, e.g. for the description of electromagnetism, the fields in QFT are quantum-mechanical operators themselves and obey commutation or anti-commutation relations. The information about the dynamics of the fields is inscribed in their *Lagrangian* \mathcal{L} , and their equations of motion can be obtained using the Euler-Lagrange equations. In QFT, the Lagrangian usually contains three types of terms: kinetic terms for each field, which are bilinear in

this field and contain its time and space derivatives, possibly mass terms for each field, containing only the field operators itself and no derivatives, and finally interaction terms, which are the terms proportional to more than one field (or its derivatives).

In QFT, we usually deal with gauge theories, i.e. the dynamics of the fields are required to be invariant under certain symmetry transformations, the gauge transformations. This is the case when the Lagrangian does not change when a certain parameter of the theory is chosen arbitrarily. According to *Noether's theorem*, every such symmetry that a theory respects is associated with a charge that is conserved. A very prominent example is the electrical charge of quantum electrodynamics (QED), which is a consequence of the invariance of QED under $U(1)$ transformations. In general, the transformations between different choices for the free parameter, i.e. different *gauges*, form a Lie group.

The SM is the QFT that describes all known elementary particles and three of the four interactions between them. As sketched in the introduction of this thesis, it cannot describe the gravitational interaction between massive particles and cannot account for the existence of dark matter or dark energy either, but has otherwise proven to be very successful in the description of the matter particles and their interactions. Its symmetry groups are $U(1)_Y$, $SU(2)_L$ and $SU(3)_C$. They are associated with respective conserved charges, the weak hypercharge Y_W , the weak isospin I and the colour charge C . The part of the SM that describes the interactions of the $SU(3)_C$ group, often called *strong interactions*, is described by quantum chromodynamics (QCD). The interactions of the $U(1)_Y \times SU(2)_L$ symmetry are described by the EW sector. Below a certain energy scale, this symmetry is spontaneously broken as will be described in more detail in the next sector, and only a $U(1)_{em}$ symmetry remains. The respective interaction is described by QED.

The aforementioned symmetries are so-called *internal* symmetries, but the fields of the SM also underlie an *external* symmetry by the Poincaré group, which contains Lorentz boosts and rotations as well as translations in the Minkowski space. The fields of the SM can be characterised by their behaviour under these transformations, which determines their spin.

The fermions of the SM, which form the matter as we know it, have a spin of 1/2 and can be divided into particles with a colour charge (quarks) and without (leptons). Both leptons and quarks are usually further divided into three generations of two particles each. Within one generation, the particles differ by their behaviour under the electroweak interaction, for example in their electric charge. The fermions of different generations mainly differ by their mass, but couple in the same way to the electroweak and strong gauge bosons. To every quark and lepton¹ in the SM, there also exists an anti-particle with opposite charge.

The SM also includes 12 vector bosons with integer spin which mediate the interactions between the charged particles – four (W^+, W^-, Z, γ) electroweak gauge bosons and eight gluons g , gauge bosons of the strong interaction. While both the photon γ and

¹Some scholars have suggested that neutrinos, the electrically uncharged leptons, are their own anti-particles. Experimental proof of this assumption, e.g. through evidence for the existence of the neutrinoless double beta decay, has yet to be provided.

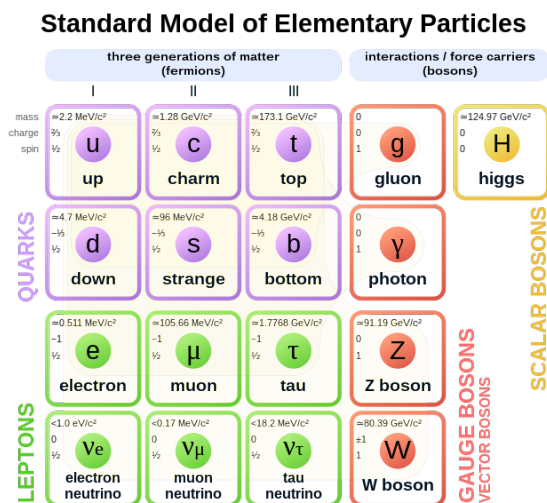


Figure 2.1: The particle content of the Standard Model, sometimes dubbed “particle zoo”. Image under public domain [57].

the gluons are massless, the W^\pm and Z bosons become massive through the process of electroweak symmetry breaking, as will be discussed in the next section. As a consequence of this process, another scalar particle is introduced: the Higgs boson with spin 0, which completes the content of the SM. All particles described by the SM, sometimes colloquially referred to as the “particle zoo”, are listed in Fig. 2.1.

2.2 Limitations of the SM and BSM Physics

As explained in Sec. 2.1, the SM has proven very successful in explaining and describing a wide range of phenomena in particle physics. Many of its predictions, e.g. the existence of the Higgs boson as a scalar particle with a mass of 125 GeV (see Sec. 2.3), have been confirmed with impressively high precision. Up until now, the results from scattering experiments do not show any evidence for deviations between the SM’s predictions and nature. However, it is widely believed nowadays that the SM might only be an *effective theory*, that is the approximate description of the low energy limit of some more fundamental theory. In this section, I will work out some of the reasons why this might be the case, and also introduce briefly some of the theories that have been suggested to describe the physics beyond the Standard Model (BSM). Since the process covered in this thesis is completely described within the SM and does not include any BSM physics, I will not go too deeply into the details of ‘new physics’. However, an introduction into the SM without at least mentioning its limitations would be incomplete. Moreover, as I will explain in Sec. 2.3, the Higgs sector of the SM is particularly sensitive to the effects of new physics, which is an important reason for the high interest researchers have in this sector.

Maybe the most obvious limitation of the SM, at least from a historical and philosophical point of view, is that it cannot describe all four (known) fundamental forces – gravity is missing. However, since this force is extremely weak in comparison with the other three forces, gravitational effects are completely negligible in experiments in particle physics, no matter how present the force of gravity is in our everyday life. Nevertheless, it would be elegant to find a QFT describing gravitational interaction and combine it with the SM to a *theory of everything* (TOE). However, gravity is not the only phenomenon not described by the SM: for example, it has been observed [58] that neutrinos can oscillate between the lepton flavour states ν_e , ν_μ and ν_τ as they propagate through space. The theoretical explanation for these neutrino oscillations implies that the three neutrinos differ in their mass, i.e. that at least two of them need to have a finite mass, which is not the case in the SM. Another prominent example for such a phenomenon is the existence of *dark matter*: there is strong evidence that the matter observed with conventional telescopes can only account for a small fraction of the total amount of gravitationally interacting matter in the universe. While there exist some theories to explain this dark matter abundance at least partially with the particle content of the SM, it is usually taken as a clear indication of the existence of BSM particles.

Finally, the SM fails to explain while the universe seems to consist of exceedingly more matter than anti-matter (*baryon asymmetry*). If we assume that the Big Bang produced equal amounts of matter and anti-matter, this asymmetry must have evolved during *baryogenesis*. This requires the *charge conjugation and parity symmetry* (CP-symmetry) to be violated. Although there exist corresponding processes in the SM, this CP violation is not strong enough to explain the observed baryon asymmetry. This list of phenomena not explained by the SM could be continued at will. Some of the ‘problems’ of the SM may seem of aesthetic nature, while others involve a more or less direct contradiction between the theoretical predictions and the observed phenomena. However, it has always to be kept in mind that most predictions of the SM have been realised and observed with astonishing precision. Direct discrepancies between a SM prediction for some parameter and the observed value are extremely rare, and even rarer are concrete indications of what BSM physics might look like. If we assume the SM to be just an effective field theory, i.e. the low-energy limit of an underlying, more comprehensive theory, we should see this approximation break down when the experimental energy scales approach the energy scale of the underlying theory. However, even with the current collision energies of 14 TeV at the LHC, we are still only able to set upper limits on any deviations from the SM parameters.

Even with the experimental limits becoming stricter over time, the variety of BSM models is inexhaustible. While some of them propose only small changes to the SM and aim at explaining only one or a few of the phenomena unexplained so far, there also exist several theories which introduce many new fields and symmetries, such as supersymmetric (SUSY) models like the minimal supersymmetric extension of the Standard Model (MSSM) [59]. There even exist a few theories proposing changes to the most fundamental concepts of the SM or introducing new dimensions, such as string theories. Despite their differences, all BSM theories have to fulfil two features: they have to be able to reproduce

the SM predictions for current experiments (within the theoretical and experimental uncertainties), since missing deviations would have made them obsolete otherwise, and they have to predict deviations from the SM at some point. Usually, this predicament can only be solved if such a deviation is either predicted to be measured very rarely (e.g. the neutrino-less double β -decay, as predicted by models such as the seesaw mechanism where the neutrinos are Majorana particles) or if the scale of the new physics is taken to be much higher than experimentally accessible energies. In any case, extremely high precision both in measurements and predictions is of the uttermost importance to restrict the space of available BSM theories. Frequently, one employs so-called *effective field theories* (EFT) in the search for new physics: new particle fields at high energies lead to new or modified couplings that can be described by an operator in the EFT at low energies. Therefore, by specifying every possible EFT operator, one can quantify the deviations in experiments from the SM in a model-agnostic way. It is therefore quite obvious to intensify the effort in terms of precision calculations especially in those sectors of the SM where changes to the theory are proposed by particularly many BSM theories or where the physical mechanisms would be particularly sensitive to them. As I will explain in Sec. 2.3, this is the case for the electroweak production channels of the Higgs boson.

2.3 The Electroweak Sector and the Higgs Mechanism

In the following, I want to sketch the outlines of the electroweak sector of the SM and the symmetry breaking by the Higgs mechanism. Rather than giving a detailed description of the underlying physics, the purpose of this section is to motivate why the electroweak sector of the SM is of special interest to theorists. As laid out before, the SM is a gauge theory, and the $U(1)_Y \times SU(2)_L$ gauge symmetry corresponds to the EW sector. The choice of the symmetry groups for a QFT can usually be motivated by certain experimental findings, which indicate the presence of conserved charges. As these charges correspond to a symmetry according to Noether's theorem, one is able to deduce the group structure (e.g. of the SM) from the experimental results. From this point of view, the requirements for a theory of the EW sector can be summarised as follows: it must reproduce the multi-flavour structure of the fermionic sector, with different couplings for left- and right-handed fermion fields. The left-handed fermions must appear in doublets, i.e.

$$\begin{pmatrix} \nu_l \\ l^- \end{pmatrix} \text{ and } \begin{pmatrix} q_u \\ q_d \end{pmatrix} ,$$

whereas the right-handed fermions may only appear in singlets. The opposite holds for the anti-fermions. Since the simplest group with doublet representation is $SU(2)$, and the EW part of the SM is supposed to include the electro-magnetic interactions as described by QED, the naive idea could be to postulate a $SU(2) \times U(1)$ symmetry for this gauge theory. As mentioned before, it turns out that $SU(2)_L \times U(1)_Y$ is the actual symmetry of the EW sector, but that the $U(1)_Y$ symmetry cannot be identified with the $U(1)_{em}$ symmetry known from QED. In fact, a theory with this gauge symmetry could

not be realised with massive gauge bosons. However, experimental evidence suggests that the gauge bosons of the weak interactions must be massive. The mechanism that helps overcoming this problem and is responsible for generating mass terms for the gauge bosons is the Higgs mechanism, which I will come back to again in this section.

In order to construct a Lagrangian which does not only fulfil *global*, but also *local* $SU(2)_L \times U(1)_Y$ symmetry, one needs to introduce covariant derivatives. For the EW sector, these are given as:

$$D_\mu = \partial_\mu + i \frac{g}{2} \tau^i W_\mu^i + i \frac{g'}{2} Y B_\mu \quad .$$

Here, τ^i are the Pauli matrices, g and g' are the couplings of the $SU(2)_L$ and the $U(1)_Y$ interactions, respectively, W_μ^i with $i = 1, 2, 3$ and B_μ are the corresponding gauge fields, and finally Y denotes the weak hypercharge. With this definition, the $SU(2)_L \times U(1)_Y$ invariant Lagrangian with fermion fields ψ can be written as:

$$\mathcal{L} = -\frac{1}{4} \left(W_{\mu\nu}^i W^{\mu\nu i} + B_{\mu\nu} B^{\mu\nu} \right) + \bar{\psi}_L i \gamma^\mu D_\mu \psi_L + \bar{\psi}_R i \gamma^\mu D_\mu \psi_R \quad , \quad (2.1)$$

with the *field strength tensors* $W_{\mu\nu}^i = \partial_\nu W_\mu^i - \partial_\mu W_\nu^i + g \epsilon^{ijk} W_\mu^j W_\nu^k$ and $B_{\mu\nu} = \partial_\nu B_\mu - \partial_\mu B_\nu$. The fermion fields have been written by projection on their left- and right-handed parts $\psi_{L,R} = \frac{1}{2}(1 \mp \gamma_5)\psi$, where $\gamma_5 = i \gamma_0 \gamma_1 \gamma_2 \gamma_3$ is the product of the Dirac gamma matrices.

As can be seen easily, no mass terms have been introduced in this Lagrangian. As mentioned before, their naive introduction would not be possible without spoiling the gauge invariance. I will now turn to a brief explanation of the Higgs mechanism which provides a very elegant way to still introduce massive gauge bosons by symmetry breaking. For pedagogical reasons, I will follow a popular argument (see for example [60]) where the general principles of the Higgs mechanism are introduced for a kind of simplified toy model, the Abelian Higgs Model, before applying the mechanism to the actual electroweak SM. For a more detailed description, the interested reader is referred to [60] and to the original contributions where the mechanism was first proposed [12, 13, 14, 15].

For our toy model, we consider a Lagrangian with one single vector field A_μ :

$$\mathcal{L} = -\frac{1}{4} F_{\mu\nu} F^{\mu\nu} \quad (2.2)$$

This is the Lagrangian of the photon field in the case of no external fermion current, with $F^{\mu\nu} = \partial^\mu A^\nu - \partial^\nu A^\mu$ being the *field strength tensor*. Applying the Euler-Lagrange equations to it yields Maxwell's equations in vacuo. It is easy to see that this Lagrangian is invariant under a local gauge transformation as defined by

$$A_\mu(x) \rightarrow A'_\mu(x) = A_\mu(x) + \partial_\mu \eta(x) \quad . \quad (2.3)$$

With this transformation, the Lagrangian becomes

$$\begin{aligned} \mathcal{L}' &= -\frac{1}{4} [\partial_\mu (A_\nu + \partial_\nu \eta) - \partial_\nu (A_\mu + \partial_\mu \eta)] \cdot [\partial^\mu (A^\nu + \partial^\nu \eta) - \partial^\nu (A^\mu + \partial^\mu \eta)] \quad (2.4) \\ &= -\frac{1}{4} [F_{\mu\nu} + \partial_\mu \partial_\nu \eta - \partial_\nu \partial_\mu \eta] [F^{\mu\nu} + \partial^\mu \partial^\nu \eta - \partial^\nu \partial^\mu \eta] = -\frac{1}{4} F_{\mu\nu} F^{\mu\nu} = \mathcal{L} . \end{aligned}$$

In the previous section, I explained that three of the four gauge bosons of the electroweak interaction in the SM are massive particles. Indeed, their masses have been measured to be 80.379 GeV for the W^\pm bosons and 91.1876 GeV for the Z boson, respectively [61]. Naively, one would therefore add a mass term $\propto A_\mu A^\mu$ for a gauge boson field to the Lagrangian to give it a non-zero mass. But we can show with the help of our toy model that such a term violates gauge invariance. After adding such a mass term, the Lagrangian reads

$$\mathcal{L} = -\frac{1}{4}F_{\mu\nu}F^{\mu\nu} + \frac{1}{2}m^2 A_\mu A^\mu \quad , \quad (2.5)$$

which is clearly not invariant under the transformation given in Eq. (2.3). Indeed, this symmetry requires the gauge boson to be massless!

We will now extend our toy model by adding another, complex scalar field ϕ that couples to the photon field, and a potential $V(\phi)$:

$$\mathcal{L} = -\frac{1}{4}F_{\mu\nu}F^{\mu\nu} + |D_\mu\phi|^2 - V(\phi) \quad . \quad (2.6)$$

Here, $D_\mu = \partial_\mu - ieA_\mu$ is the *covariant derivative*, with e being the (electric) elementary charge. Comparing Eq. (2.6) to the Lagrangian of quantum electrodynamics, we see that ϕ corresponds to a ‘scalar electron’ with charge $-e$ (*scalar electrodynamics*). The potential $V(\phi)$ should take the form $V(\phi) = \mu^2 |\phi|^2 + \lambda(|\phi|^2)^2$, which is the most general potential allowed by the conditions of renormalisability and gauge invariance. We can see that the Lagrangian is still invariant under the transformation of Eq. (2.6) if at the same time the field ϕ undergoes a $U(1)$ phase transformation:

$$\begin{aligned} A_\mu(x) &\rightarrow A'_\mu(x) = A_\mu(x) + \partial_\mu\eta(x) \quad \text{and} \\ \phi(x) &\rightarrow \phi'(x) = e^{ie\eta(x)}\phi(x) \quad . \end{aligned} \quad (2.7)$$

Assuming that $\lambda > 0$, we have two possibilities for the state of minimum energy in our theory: if $\mu^2 > 0$, the only minimum is the trivial one at $\phi = 0$; but if $\mu^2 < 0$, we will find a local maximum at $\phi = 0$, while we have a continuum of minima at $\langle\phi\rangle = \sqrt{-\frac{\mu^2}{2\lambda}}$. Here, $\langle\phi\rangle$ is the vacuum expectation value (VEV) of ϕ , and it has a degeneracy in the angle of ϕ in the complex plane. We can choose the direction of the vacuum arbitrarily (conventionally, it is chosen to lie along the real axis), but as soon as we decide for a particular direction, e.g. to perform a perturbative calculation around the vacuum state, the original $U(1)$ symmetry of the Lagrangian is *spontaneously broken*.

In order to show the consequences of this symmetry breaking, we expand the Lagrangian around the VEV. Therefore, we rewrite the field as

$$\phi \equiv \frac{1}{\sqrt{2}}e^{i\frac{\chi}{v}}(v+h) \quad , \quad (2.8)$$

where $v := \sqrt{-\frac{\mu^2}{\lambda}}$. Here, h and χ are real, scalar fields, and $\phi(h=\chi=0) = \frac{v}{\sqrt{2}} = \langle\phi\rangle$ corresponds to the VEV of ϕ . The expansion of the Lagrangian up to terms of the second

order now reads:

$$\begin{aligned} \mathcal{L} = & -\frac{1}{4}F_{\mu\nu}F^{\mu\nu} - evA_\mu\partial^\mu\chi + \frac{e^2v^2}{2}A_\mu A^\mu \\ & + \frac{1}{2}\left(\partial_\mu h\partial^\mu h + 2\mu^2 h^2\right) \\ & + \frac{1}{2}\partial_\mu\chi\partial^\mu\chi + \dots \end{aligned} \quad (2.9)$$

The dots (...) indicate terms corresponding to higher order terms, i.e. $\chi - h$ interactions. Apart from one term, corresponding to a mixed $\chi - A$ propagator, Eq. (2.9) resembles the Lagrangian of three fields: a massive vector field A_μ with mass $m := ev$, a massive scalar field h with mass $m_h := \sqrt{-2\mu^2}$, and a massless scalar field χ , which we call the *Goldstone boson*. If we make use of the gauge invariance, we can perform the following transformation on A :

$$A \rightarrow A' = A - \frac{1}{ev}\partial_\mu\chi \quad , \quad (2.10)$$

which is equivalent to saying that the angular degree of freedom (DOF) of ϕ should vanish. As a consequence of this choice (the *unitary gauge*²), the field χ disappears from the Lagrangian and also the mixed $\chi - A$ term drops out. At the cost of introducing another particle, we have found a mechanism to give the gauge boson a mass term in a gauge-invariant way. This is the Higgs mechanism.

We can now apply the Higgs mechanism in the same way to the EW part of the SM, the Weinberg-Salam model. We can write the kinetic terms of the familiar Lagrangian of Eq. 2.1 as

$$\mathcal{L}_{WS,kin.} = -\frac{1}{4}\left(W_{\mu\nu}^i W^{\mu\nu i} + B_{\mu\nu}B^{\mu\nu}\right) \quad . \quad (2.11)$$

We now also add a complex, scalar $SU(2)$ doublet field $\Phi = \begin{pmatrix} \phi^+ \\ \phi^0 \end{pmatrix}$ with a scalar potential V . Its contribution to the Lagrangian is thus given as

$$\mathcal{L}_S = (D^\mu\Phi)^\dagger(D_\mu\Phi) - V(\Phi) \quad , \quad (2.12)$$

with $D_\mu = \partial_\mu + i\frac{g}{2}\tau W_\mu + i\frac{g'}{B_\mu}Y$. Again, the potential V is chosen to be the most general allowed by the constraints of renormalisability and invariance under $SU(2)_L$ transformations, which reads

$$V(\Phi) = \mu^2|\Phi^\dagger\Phi| + \lambda\left(|\Phi^\dagger\Phi|\right)^2 \quad . \quad (2.13)$$

²This gauge is very convenient to illustrate the particle content of the theory. However, in the unitary gauge, scattering cross sections include contributions $\propto (k^2)^n$. Gauge invariance requires these contributions to cancel in the final result of a calculation, but not necessarily at intermediate steps, which can lead to numerical instability. Therefore, calculations are often performed in a different gauge, the Landau gauge.

Like before, we assume $\lambda > 0$ and look at the case of $\mu^2 < 0$, when the state of minimal energy is not at $\Phi = 0$. Just as in the example of the Abelian toy model in the previous paragraphs, the field Φ develops a non-vanishing VEV, which can be chosen to lie in an arbitrary direction in the $SU(2)_L$ space. With the choice

$$\langle \Phi \rangle \equiv \frac{1}{\sqrt{2}} \begin{pmatrix} 0 \\ v \end{pmatrix} , \quad (2.14)$$

the electromagnetic charge $Q = \frac{(\tau_3 + Y)}{2}$ of the VEV becomes $Q \langle \phi \rangle = 0$, with Φ having the hypercharge $Y = 1$. With this VEV from Eq. (2.14), the original $SU(2)_L \times U(1)_Y$ symmetry is broken to a $U(1)_{EM}$ symmetry.

Again, we go to the unitary gauge,

$$\Phi = \frac{1}{\sqrt{2}} \begin{pmatrix} 0 \\ v + h \end{pmatrix} , \quad (2.15)$$

and get, by insertion into Eq. 2.12, a contribution from the kinetic energy term that is equivalent to gauge boson mass terms:

$$M^2 \propto \frac{1}{2}(0, v) \left(\frac{g}{2} \tau W_\mu + \frac{g'}{2} B_\mu \right)^2 \begin{pmatrix} 0 \\ v \end{pmatrix} \quad (2.16)$$

We find linear combinations of the original fields which now obtain mass terms and therefore correspond to the physical gauge Boson fields. These are

$$\begin{aligned} W_\mu^\pm &= \frac{1}{\sqrt{2}} (W_\mu \mp i W_\mu^2) , \\ Z^\mu &= \frac{-g' B_\mu + g W_\mu^3}{\sqrt{g^2 + g'^2}} , \\ A^\mu &= \frac{g B_\mu + g' W_\mu^3}{\sqrt{g^2 + g'^2}} . \end{aligned} \quad (2.17)$$

Commonly, they are written in terms of a mixing angle θ_W , the Weinberg angle or weak mixing angle, with

$$\sin \theta_W \equiv \frac{g'}{\sqrt{g^2 + g'^2}} ,$$

which is fixed by the fact that the photon field A^μ must couple to fermions with the well-known electromagnetic coupling e : $e = g \sin \theta_W = g' \cos \theta_W$. From Eq. (2.16), we get the following values for the Boson masses:

$$M_W^2 = \frac{1}{4} g^2 v^2, \quad M_Z^2 = \frac{1}{4} (g^2 + g'^2) v^2, \quad M_A = 0 .$$

It should be noted that, if we had chosen a different gauge, additional Goldstone bosons would appear in the spectrum. In the SM, there are three Goldstone bosons, which in *Feynman gauge* have masses M_W and M_Z .

The Higgs field does not only give the gauge W^\pm and Z bosons their masses, but is also ‘used’ to generate the fermion masses by coupling it to the fermion fields with so-called *Yukawa couplings*. Although it plays only a minor role in the process considered in this thesis, I want to take the opportunity to briefly introduce how the Higgs field enters the generation of the fermion masses.

Naively adding masses to a fermion field ψ would imply to add a mass term of the form

$$\mathcal{L}_m = -m\bar{\psi}\psi = -m(\bar{\psi}_L\psi_R + \bar{\psi}_R\psi_L) \quad , \quad (2.18)$$

which is again forbidden by gauge invariance since the left- and right-handed parts of ψ transform differently under $SU(2)_L$ and $U(1)_Y$. But we can instead add a term by introducing a Yukawa coupling of the Higgs fields to the fermions, which for the down-type quarks would have the form

$$\begin{aligned} \mathcal{L}_{\text{Yukawa}, d} &= -\lambda_d \bar{Q}_L \Phi d_R + \text{h.c.} \\ &= -\lambda_d \frac{1}{\sqrt{2}} (\bar{u}_L, \bar{d}_L) \begin{pmatrix} 0 \\ v + h \end{pmatrix} d_R + \text{h.c.} \quad . \end{aligned} \quad (2.19)$$

This can be regarded as a mass term, which becomes obvious when we substitute $\lambda_d = \frac{m_d \sqrt{2}}{v}$. In the same manner, with the help of the $SU(2)_L$ doublet $\Phi^c := -i\tau_2 \Phi^*$, we can formulate a Yukawa coupling term for the up-type quarks:

$$\mathcal{L}_{\text{Yukawa}, u} = -\lambda_u \bar{Q}_L \Phi^c u_R + \text{h.c.} \quad . \quad (2.20)$$

The mechanism can be applied straightforward on the charged leptons as well. Only the neutrinos, lacking a right handed partner, remain massless. However, extensions of the SM with neutrinos masses via Yukawa couplings exist (*seesaw mechanism*).

If we express the kinetic energy terms of the fermions in terms of the mass eigenstates of the gauge bosons (see Eq. (2.17)), we can determine the charged and neutral weak current interactions. This also allows us to determine the parameter v of the Higgs field’s VEV as $v^2 = (\sqrt{2}G_F)^{-1} \approx (246 \text{ GeV})^2$ from the μ decay $\mu \rightarrow e\bar{\nu}_e\nu\mu$. It is worth noticing that we can express the Higgs’ potential from Eq. (2.13) only in terms of v and of the mass of the Higgs boson, $m_H^2 = 2v^2\lambda$.

Although the properties of the particle discovered in 2012 by the experiments of ATLAS and CMS are so far consistent with the properties of the Higgs boson of the SM, it remains an open question whether the mechanism of EW symmetry breaking is realised exactly in this simplest version in nature. One difficulty that many theorists see with this particular realisation of the EW symmetry breaking is that it leads to quadratically divergent virtual Higgs loop corrections, which have to be accounted for by counterterms for every order of perturbation theory. This so-called *fine tuning* is considered unnatural by many researchers. Moreover, most or nearly all models for BSM physics propose a modification to the Higgs sector in some way. In SUSY for example, the divergences can be canceled automatically and are thus accounted for in a natural way. Usually, extensions to the SM suggest a more complicated version of the EW symmetry breaking with additional Higgs bosons, e.g. with different electric charge,

mass or coupling strengths. Of course, one can hope for their direct detection, i.e. by producing them in collider experiments, but so far, there exists no experimental evidence for their existence. As with any other BSM particle, the reason for this could either be that the particle is too heavy to be produced at a collider, or that its production rates are so low that its production cannot be distinguished from background processes. Thus, one has to resort to indirect detection of the new physics. Therefore, it is necessary to have high precision measurements of the processes where one expects the new physics effects to manifest. From this perspective, the Higgs sector also seems very promising: adding one or more Higgs bosons in a BSM theory would lead to a modification of the Higgs coupling and thus to a derivation of their SM value [62]. Put differently, if the measured couplings deviate from the predictions of the SM, this would lead to a violation of unitarity at some energy scale and therefore indicate the presence of new physics at some higher scale [63]. For example, BSM physics could lead to a correction of the VVH vertex and introduce a momentum dependent term [38]. This particular vertex can be probed in both the VBF and the HV processes.

To summarise, one can say that the mechanism of EW symmetry breaking is very sensitive to any deviation from the SM. It is therefore crucial to probe the EW and Higgs sector with the highest precision possible in order to find out more about possible BSM physics. For this reason, one sometimes speaks of *the Higgs window to new physics*.

Chapter 3

From QFT to Precision Calculations

In Chap. 2, I explained how the Lagrangian of a QFT contains all the information about the dynamics of the fields and their symmetries. However, neither the Lagrangian itself, nor the couplings or fields inside it can be measured directly. Finding correspondences between the parameters of a theory and physical observables is a subtle procedure. Generally, we will in most experiments observe interactions between particles, for example the Coulomb force between two electrons or the scattering of two protons off each other at a hadron collider facility. When translated into the picture of QFT, this is equivalent to starting with an initial state with a defined ensemble of n particles, which then interact and yield a final state with m particles. As explained in Sec. 2.1, QFT offers the possibility to describe the creation and annihilation of particles, which is why the number of particles does not have to be constant after the process. A very common¹ tool set to describe the transition from the initial to the final state, i.e. the interactions of the particles, is perturbation theory. The central concept behind perturbation theory is the so called \hat{S} -matrix, which is defined as giving the *amplitude* for the transition from the initial state $|i\rangle$ to the final state $\langle f|$ while considering all possible interactions:

$$S_{fi} := \langle f | \hat{S} | i \rangle \quad . \quad (3.1)$$

The square of this amplitude then yields the probability of ending up with $\langle f|$ after any interaction between the particles in $|i\rangle$ took place. The operator \hat{S} in Eq. (3.1) can often be related to the Lagrangian of the theory. If the interaction terms $\mathcal{L}_{\mathcal{I}}$ only contain the field operators themselves and not their derivatives, \hat{S} takes the form:

$$\hat{S} = \hat{T} \exp \left\{ i \int d^4x \mathcal{L}_{\mathcal{I}} \right\} \quad . \quad (3.2)$$

Here, \hat{T} is the quantum mechanical *time ordering operator*, which has to be understood as acting on the fields after expansion of the exponential function.

¹Other methods, such as lattice calculations, exist, but are beyond the scope of this work.

The idea of perturbation theory is to treat the interactions between the fields as small perturbations to the free, non-interacting theory, and to expand the expression in Eq. (3.2) in a power series with the coupling constants as expansion parameters. Obviously, if and only if the dimensionless couplings in $\mathcal{L}_{\mathcal{I}}$ are small compared to one, higher orders of the theory become more and more suppressed and we can hope for the series to converge. For calculations in QCD, this is guaranteed at sufficiently high energies (more on the energy-dependant behaviour of the strong coupling constant α_s will be discussed in 3.1.1), and it is generally the case for EW calculations, where the relevant *fine structure constant* α is of the order $\sim 10^{-2}$. To be able to perform comparisons between experimental data and theoretical predictions, the perturbative calculations should – at least – match the precision that is reached by contemporary experiments such as the LHC detectors. Since the accuracy of a perturbative calculation is mostly governed by the order at which the perturbative series is truncated, it is not enough to consider only the first, leading order (LO) for most processes, but at least the next-to-leading order (NLO) in QCD has to be taken into account. For some processes, even higher orders (NNLO, N3LO) in the strong coupling or NLO-EW corrections need to be considered to reach meaningful precision (the importance of the different higher order corrections for the VBF process considered here is discussed in Chap. 4).

In Sec 3.1, I will explain how exactly experimentally measured cross sections can be calculated with the help of the perturbatively approximated \hat{S} -matrix and will also mention how non-perturbative effects in QCD have to enter these calculations. As most of the difficulties appearing through a higher order calculation already manifest at NLO, I will explain the procedure of such a calculation in Sec. 3.2 with a special focus on the treatment of divergences that appear during this process.

Fixed-order calculations can be brought even closer to experimental observables by parton showers. I will briefly discuss their principles in the last section 3.3 of this chapter, focussing on their matching to a hard process calculated at NLO.

3.1 Cross Sections

In the last paragraphs, I sketched how the transition probability from a defined initial state to a (different) final state by interaction between the particles can be linked to the Lagrangian of the theory. However, what is typically measured in most experiments in particles physics is a cross section. This term comes from scattering experiments in classical mechanics, where a target with a finite cross section is shot at with projectiles (assumed to be infinitely small), and the probability of a projectile hitting the target is proportional to its surface area. However, elementary particles cannot be considered as classical rigid bodies and it can be more illustrative to define a hadronic cross section starting from the rate at which a given event occurs in a collider experiment. For our purposes, it is useful to rewrite this quantity in such a way that the part depending on the experimental setup, i.e. on the collider's properties, and the part corresponding to the physics of the scattering itself factorise. The collider-dependent part is summarised in the *luminosity* L and can be interpreted as the density of particles per unit area and unit

time passing the experiment. From the dimensions of the luminosity, $[L] = t^{-1}s^{-2}$, and the event rate, $\left[\frac{dN}{dt}\right] = t^{-1}$, we can derive that the remaining part has the dimensions of an area. In analogy to classical scattering, we call this the cross section σ . We can relate this directly to the \hat{S} -matrix of Eq. (3.1): when we integrate the transition probability over all initial and final states under consideration, we will get a measure of how likely a scattering event is bound to happen. However, since we are not interested in the trivial case without any scattering, we will subtract it from the \hat{S} -matrix, ending up with the invariant matrix element \mathcal{M}_{fi} , which we can define via

$$\begin{aligned} S_{fi} - \delta_{fi} &= \langle f | \hat{S} - \mathbb{1} | i \rangle \\ &= i(2\pi)^4 \mathcal{M}_{fi} \delta^{(4)} \left(\sum_i p_i - \sum_f p_f \right) \end{aligned} \quad (3.3)$$

$$\times \prod_i (2E_i V)^{-1/2} \times \prod_f (2E_f V)^{-1/2} \quad , \quad (3.4)$$

where V is the volume in which the scattering is happening, p_i and p_f are the momenta of the initial and the final state particles, and E_i and E_f their energies. The delta function simply ensures four-momentum conservation in the scattering process. As stated before, we will have to consider the square of this expression to obtain a transition probability. The integration over the phase space of possible states then leaves us with a quantity that has indeed the dimension of an area and can be identified with the partonic cross section:

$$\sigma_{fi} \equiv \frac{\int d\text{PS}_{n_f} |\mathcal{M}_{fi}|^2}{4\sqrt{(p_1 \cdot p_2)^2}} \quad . \quad (3.5)$$

Here, we already assumed a scattering process with two massless² particles with four-momenta p_1, p_2 in the initial state, as it is usually the case for partonic collisions. The factor $4\sqrt{(p_1 \cdot p_2)^2} \equiv F$ in the denominator is the flux of incoming particles, which we want to normalise to. For brevity, we will absorb the factor of $1/F$ in the definition of the matrix element from now on. Finally, the Lorentz-invariant n_f -particle phase space, abbreviated $d\text{PS}_{n_f}$ in Eq. (3.5), is defined as

$$d\text{PS}_{n_f} \equiv \left(\prod_f \frac{d^3 p_f}{(2\pi)^3 2E_f} \right) (2\pi)^4 \delta^{(4)} \left(\sum_i p_i - \sum_f p_f \right) \quad . \quad (3.6)$$

3.1.1 A Few Words about Non-Perturbative QCD

While our calculation is largely based on perturbation theory, calculating a full cross section for a hadronic collision requires the inclusion of some non-perturbative effects as

²While assuming that $m_i \approx 0$ for the incoming partons is a good approximation for collider experiments anyway, where the kinetic energy of the particles is by several orders of magnitude higher than their rest mass, it is even a necessary assumption for the factorisation theorem that is dealt with at the end of Sec. 3.1.1.

well. In this subsection, I will follow some arguments from [64] to explain why and how these come into play.

In the last paragraphs, we have obtained an expression for the partonic cross section of a $2 \rightarrow n$ scattering process. Yet we have set aside the fact that in a collider like the LHC, we are actually probing hadrons, i.e. composite particles, and not isolated partons. The reason why we cannot directly collide colour-charged particles – and at the same time the reason why we can factorise out the partonic part of the cross section – lies within the nature of the strong interaction and the *running* of the coupling constant α_s [64]: if we want to calculate perturbatively some observable \mathcal{O} related to a process with an energy scale Q^2 in QCD, QFT requires renormalisation to remove divergences occurring during the calculation. As will become clear in the next section 3.2, this procedure involves the introduction of another energy scale μ_R^2 . Although this parameter is introduced rather arbitrarily and never appears in the Lagrangian of the theory, the result of the calculation would artificially depend on the ratio Q^2/μ_R^2 . Since this would be clearly unphysical, we require independence of \mathcal{O} from μ_R^2 , which translates to $\frac{d\mathcal{O}}{d\mu_R^2} = 0$. As our considerations should be valid for any (dimensionless) QCD observable, the only other dependence apart from the one on Q^2/μ_R^2 that \mathcal{O} might have is on the coupling constant α_s . Our requirement can therefore only be met if we have an implicit dependence on μ_R^2 hidden inside the dependence on α_s that cancels the explicit dependence. In conclusion, this implies that α_s depends on the scale at which we measure it. We call this behaviour the *running* of the strong coupling.

In a more illustrative way, one can also explain this effect by vacuum fluctuations. In a QFT, virtual particles and anti-particles can exist for very short times in the vacuum state. As a consequence, a charged particle is always surrounded by a cloud of virtual particles and anti-particles. If we compare this situation to the presence of an electrically charged particle, e.g. an electron, in a medium with real charge carriers, then we would expect the charge carriers with positive charge (or virtual positrons in the vacuum) to be closer to the electron than negative charge carriers, corresponding to virtual electrons in our original situation. In the case of a charge inside a dielectric, this effect leads to a screening of the charge, which effectively gets smaller with increasing distance. The same is indeed observed in QED, where the coupling α decreases with increasing distance, which is equivalent to a smaller momentum transfer. However, the non-Abelian structure of QCD leads to an inverse effect for colour-charged particles. As a result, the coupling α_s increases with increasing distancing or decreasing momentum transfer, respectively. We describe the running of a coupling α_x by the so called *renormalisation group equation* (RGE), which describes how α_x , given at one scale μ_0 , evolves to another scale μ_R :

$$\mu_R^2 \frac{d\alpha_x(\mu_R^2)}{d\mu_R^2} = \beta(\alpha_x) \quad .$$

In QED, the function $\beta(\alpha)$ is positive, while $\beta(\alpha_s)$ in QCD is negative. We can expand it in a power series in α_s as

$$\beta(\alpha_s) = -\alpha_s^2 \sum_{n=0}^{\infty} \beta_n \alpha_s^n \quad .$$

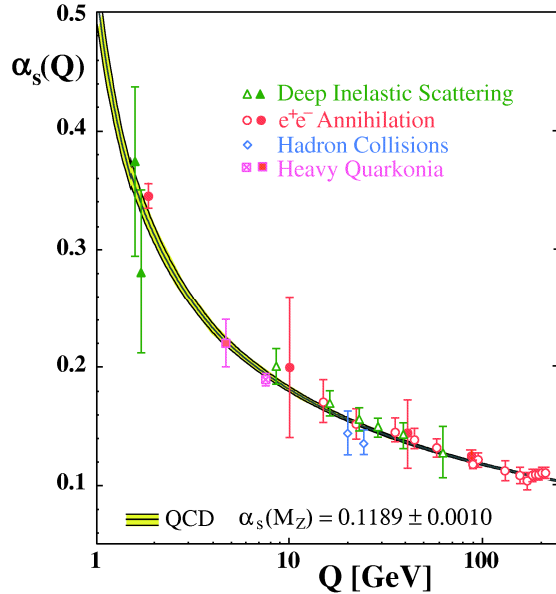


Figure 3.1: The value of α_s at different energy scales as measured by experiments (status of 2006). The curves are theoretical QCD predictions. Figure taken from [65].

Taking into account only the first order³ ($n = 0$), the β -function of QCD takes the approximate form

$$\beta \approx -\alpha_s^2 \cdot \beta_0 = -\frac{(11C_A - 2N_f)}{12\pi} \alpha_s^2 = -\frac{(33 - 2N_f)}{12\pi} \alpha_s^2 \quad , \quad (3.7)$$

where $C_A = 3$ is a *Casimir colour factor* and N_f is the number of active quark flavours. As we can see, as long as $N_f \leq 16$, the QCD β -function in one-loop approximation is always negative. For comparison, the equivalent approximation to the β -function of QED yields

$$\beta_{QED}(\alpha) = \frac{2}{3\pi} \alpha^2 + \mathcal{O}(\alpha^3) > 0 \quad .$$

There are two important effects connected to the running of α_s as described above: confinement and asymptotic freedom. From what we know about how α_s evolves, we expect that in the $q \rightarrow \infty$ limit, $\alpha_s(q^2)$ will approach 0. Indeed, at high momentum transfer, colour-charged particles behave *asymptotically free*. On the other hand, we expect the coupling to increase with lower momentum transfer. Even though the expansion of Eq. (3.7) of the β -function will break down at some point with α_s becoming larger and thus make the calculation of the behaviour of α_s in this regime perturbatively impossible, this effect manifests in nature: we can only observe colour-neutral objects, the colour-charged particles are *confined* in bound states. If we tried to isolate e.g. a quark from a hadron, the energy necessary to do this would increase with distance, until

³While the first and the second order coefficients, β_0 and β_1 , are independent of the renormalisation scheme that is used, this is not true any more for higher order terms $n \geq 2$.

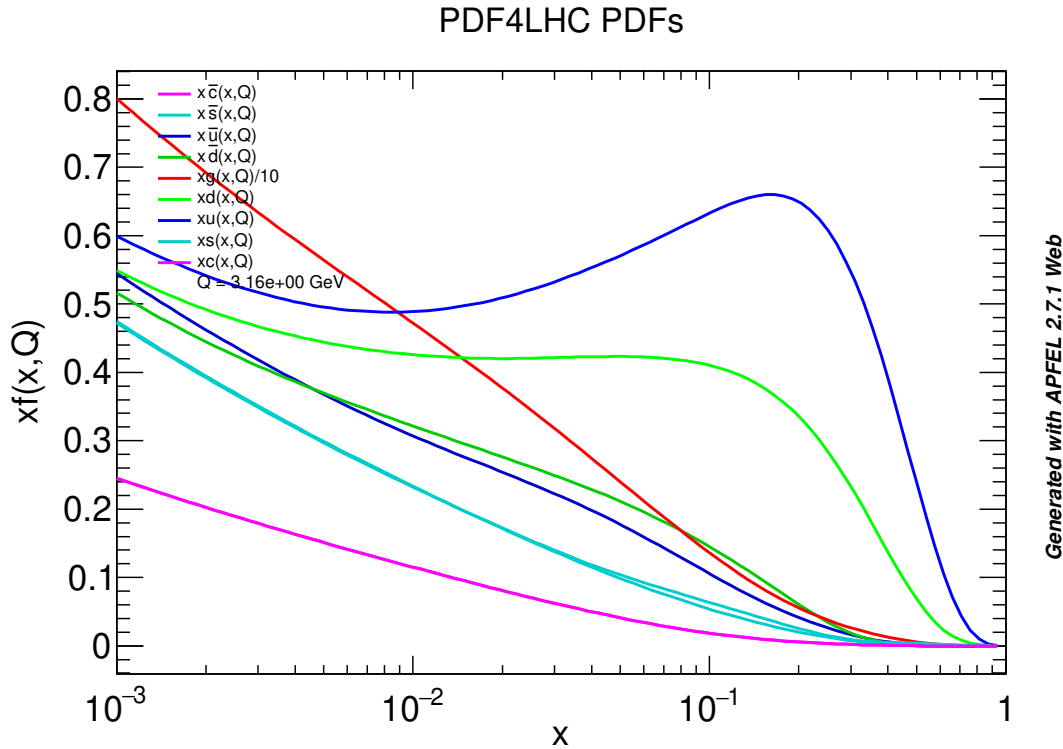


Figure 3.2: Different PDFs for the proton at a scale of $Q = 3.16$ GeV. Plotted with the web interface of the APFEL library [66].

it would rise high enough to create new quark-antiquark pairs, leading to new confined states.

As we can see, we cannot work with (anti-)quarks and gluons at a collider facility the same way we can use electrically charged leptons. Instead, we can only use hadrons, for instance protons or antiprotons, where the colour-charged particles exist in bound states. However, as we learned above, α_s becomes very small at the typical energy regime in these bound states and perturbative methods break down. Therefore, we resort to heuristic *parton distribution functions* (PDF) to parametrise the inner structure of hadrons. The idea behind PDFs is that in hadronic collider experiments, we deal with energy scales Q high enough for the partons inside a hadron to be considered free. Simply speaking, these functions $f_i(x, Q)$ then give us the probability density for finding a parton i carrying the momentum fraction x of the hadron momentum when probing it at the energy scale Q . They are process-independent, so a PDF fit to the results of one experiment could be used to describe the partonic content of the hadron for any other experiment as well. Although we cannot perturbatively calculate the PDFs and have to rely on fits, we can still say quite a few things about their behaviour. For one, some statements about the PDFs can be made based on arguments of unitarity alone. Summing over all partons i and integrating over the momentum fraction x weighted by the respective PDF should

yield one, since the total hadron momentum is distributed amongst its partons:

$$\sum_i \int_0^1 dx x f_i(x, Q) = 1 \quad .$$

Similar statements can be made about the PDFs of the *valence* and the *sea* quarks of a hadron, i.e. the real and the virtual quarks it consists of: when integrating the difference $f_q(x, \mu) - f_{\bar{q}}(x, \mu)$ of the PDFs of a quark q and the corresponding antiquark \bar{q} over the whole x -range, the result must be equal to the number of valence quarks of flavour q in the hadron minus the number of valence quarks of flavour \bar{q} . In the case of quark flavours which only exist as sea quarks in a hadron, the results must be zero.

A second important feature of PDFs is that we can evolve them from one energy scale Q_0 to another scale Q_1 analytically in a similar manner to the evolution of α_s from one scale to another. The equations to describe this evolution were independently discovered by three research teams: By Vladimir Gribov and Lev Lipatov in 1972 [67], by Yuri Dokshitzer in 1977 [68] and by Guido Altarelli and Giorgi Parisi in 1977 [69]. While they are sometimes still called Altarelli-Parisi equations after the two latter ones, they are most commonly referred to as DGLAP equations after the initials of all authors today. These differential equations are based on the so-called *splitting kernels* P_{ij} , which describe the probability for a parton of type j radiating a parton of type i (see also Sec. 3.3). Simply put, the general idea behind the DGLAP evolution is that the variation of the i -th PDF with respect to the energy scale Q can be derived by convoluting the PDFs for all partons j at higher energies with the probability that the j -th parton radiates parton i with the right energy fraction. For example, the scale dependence of the probability $f_{q_i}(x, Q)$ to find a quark i with momentum fraction x at some energy scale Q is given by:

$$Q^2 \frac{df_{q_i}(x, Q^2)}{dQ^2} = \frac{\alpha_s(Q^2)}{2\pi} \int_x^1 \frac{dy}{y} \left(P_{q_i g}(x/y) f_g(y, Q^2) + \sum_j P_{q_i q_j}(x/y) f_{q_j}(y, Q^2) \right) \quad .$$

The illustrative explanation would be that the variation of the i -quark parton density comes from the density of finding some quark j with higher momentum fraction y times the probability that i comes from the splitting of j , plus the density of a gluon times the probability that i comes from a gluon splitting. However, this simplified explanation is only valid for the leading order approximation of the splitting kernels and neglects higher order effects [64, 70]. On a side note, the splitting kernels are also important for the theory of parton showers that will be dealt with in Sec. 3.3.

Going back to the description of a scattering process at a hadron collider, we consider the partons a, b inside the hadrons A, B to be massless and to carry only momentum in the beam direction. Any internal degrees of freedom of the hadron are neglected, and we can parametrise the partonic momenta $p_{a,b}$ as fractions $x_{a,b}$ of the hadron momenta $P_{A,B}$:

$$\begin{aligned} p_a &= x_a P_A \quad , \\ p_b &= x_b P_B \quad . \end{aligned}$$

The factorisation theorem now states that we can separate the hadronic cross section for our scattering into a perturbative, partonic part for the so-called *hard process* and a process-independent part described by the PDFs that covers the partonic structure of the hadrons. This factorisation introduces a scale μ_F at which the PDFs are evaluated and which separates the perturbative regime of the hard process from the domain of the PDFs. Usually, the scale is taken to be of the order of kinematic invariants characteristic to the hard process. Since the scale is more or less arbitrary and does not correspond to a physical quantity, the result of an ideal calculation should be independent of the particular choice. For this reason, it is very common to vary the scale (e.g. by factors of 0.5 to 2) and to take the variation in the result as an estimator of the uncertainty related to the factorisation and to higher order corrections which were not taken into account.

We can now finally obtain the total cross section for a scattering process $AB \rightarrow f$ with a final state f at a hadron collider by convoluting the partonic cross section $\sigma_{ab \rightarrow f}$ and the PDFs for the partons a, b :

$$\sigma_{AB \rightarrow f} = \sum_{a,b} \int_0^1 dx_a \int_0^1 dx_b f_a^A(x_a, \mu_F) f_b^B(x_b, \mu_F) \sigma_{ab \rightarrow f}(p_a, p_b, \mu_F) \quad (3.8)$$

Sometimes, a θ -function of the form $\theta\left((p_a + p_b)^2 - M^2\right)$ is included in the prescription to indicate that the partonic center of mass energy $s = (p_a + p_b)^2$ must be large enough to produce the final state particles with total invariant mass M . Otherwise, this restriction must be taken into account in the calculation of the partonic cross section.

Using this formula, we can calculate the cross section for a hadronic scattering process if we can calculate the partonic cross section from Eq. (3.5). Since in practice, an analytic evaluation of the integrals over the phase space and over $x_{1,2}$ is almost always impossible, we resort to numerical methods like Monte Carlo integration.⁴ For their purposes, it is often more convenient to perform a change of variables for the integration. A very common choice is to use the ratio of the partonic and the hadronic centre-of-mass energy, $\tau = s/S$ and the rapidity of the two-parton system $y = \frac{1}{2} \ln\left(\frac{x_1}{x_2}\right)$. Using this prescription, we can calculate the cross section for a hadronic scattering process if we are able to calculate the partonic cross section from Eq. (3.5). A more detailed prescription on exactly how to calculate the matrix element in higher orders of perturbation theory is still missing and will be discussed in the next section.

3.2 NLO Corrections

In the previous section, we have seen how a partonic scattering cross section is related to the Lagrangian of a field theory via the matrix element \mathcal{M}_{fi} or \hat{S} . From Eq. (3.2),

⁴The term *Monte Carlo methods* generally refers to numerical methods where observables are obtained by using (pseudo-)random numbers. For calculations in particle physics, two applications are important, and the use of the term is therefore ambiguous: for one, the numerical integration of complicated functions, e.g. phase space integrals, is usually performed by Monte Carlo methods. On the other hand, *Monte Carlo event generators* often refers to shower Monte Carlos (SMC), i.e. programs where pseudo-random numbers are used for the probabilistic generation of radiation in a parton shower (see Sec. 3.3).

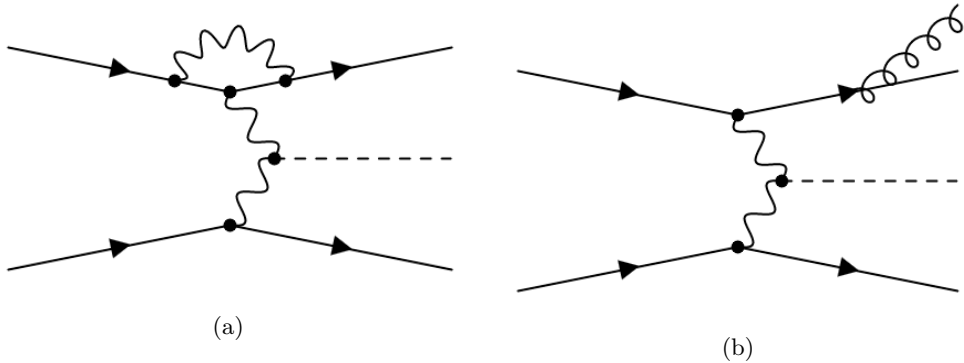


Figure 3.3: Examples for a one-loop virtual EW correction (a) and a real emission QCD correction to a generic VBF process.

we know that, after expanding the exponential function, we will end up with an a priori infinite sum of terms of the following form:

$$\int dx_1 \cdots \int dx_n \hat{T} \left[\prod_{i=1}^n \mathcal{L}_{\mathcal{I}}(x_i) \right]$$

In the interaction Lagrangian $\mathcal{L}_{\mathcal{I}}$, the terms are generally products of field operators at some power (or their derivatives) with coupling constants. As we recall, a necessary condition for perturbation theory to be feasible is that the couplings are small compared to one. Then, higher order terms in the sum – corresponding to higher orders of the coupling constants – are suppressed and we can cut off the sum at some finite order. We then end up with a finite sum where each summand contains a time-ordered product of field operators. To evaluate them, we can make use of *Wick's theorem* [71], which helps to translate them into simpler expressions. These expressions can be represented graphically by *Feynman diagrams*, where each component corresponds to a mathematical expression by a set of *Feynman rules*.

For example, taking into account only the first summand $\mathcal{M}^{(0)}$ (which is sometimes also called the *Born approximation*) for the scattering amplitude of the electroweak process $us \rightarrow Hdc$ leaves us with only one contribution in the end, which can be translated into the Feynman diagram depicted in Fig. 4.3. The corresponding Born cross section would then be

$$\sigma^{LO} = \frac{1}{4\sqrt{(p_1 \cdot p_2)^2}} \int d\text{PS}_3 |\mathcal{M}^{(0)}|^2 \equiv \frac{1}{F} \int d\text{PS}_3 \mathcal{B}_3 \quad ,$$

where the index 3 on the phase-space measure and the Born matrix element \mathcal{B} indicates the three-particles final state.

Let us stay with our example of $us \rightarrow Hdc$ scattering and assume that we want to include one more order of the electroweak coupling α in the perturbative series, i.e. $\mathcal{M}^{(1)}$. This NLO correction already yields more than only one term. Here, the contributions

can be translated into Feynman diagrams with closed particle loops, such as the example diagram depicted in Fig. 3.3a. However, to be consistent in our calculation, we need to take into account also other diagrams without loops (which we also call tree-level diagrams), which contribute at the same order of the coupling α as the loop diagrams in the squared matrix element, but describe a process with an additional final state particle, e.g. an additional photon emission (see Fig. 3.3b), a so-called real emission. As we will see in the next subsection 3.2.1, this is not only necessary to stay consistent with the orders of the perturbative expansion, but also to cancel divergences associated with the loop diagrams. Apparently, since the 3- and the 4-particle final states ‘live’ in different phase spaces, our NLO cross section has to be split into two contributions which have to be integrated separately:

$$\sigma^{NLO} = \sigma_3^{NLO} + \sigma_4^{NLO} \quad (3.9)$$

The latter term now corresponds to the tree-level diagrams for the final state with one additional real emission and is calculated by integrating the real squared matrix element \mathcal{R}_4 over the 4-particle phase space. The former term includes both the Born amplitude squared \mathcal{B}_3 and the interference of the Born and the virtual amplitude \mathcal{V}_3 :

$$\begin{aligned} & \frac{1}{F} \int d\text{PS}_3 \left| \mathcal{M}^{(0)} + \mathcal{M}^{(1)} \right|^2 \\ &= \frac{1}{F} \int d\text{PS}_3 \left(\left| \mathcal{M}^{(0)} \right|^2 + \left| \mathcal{M}^{(0)} \mathcal{M}^{(1)*} \right| + \left| \mathcal{M}^{(1)} \right|^2 \right) \\ &\approx \frac{1}{F} \int d\text{PS}_3 \left(\left| \mathcal{M}^{(0)} \right|^2 + \left| \mathcal{M}^{(0)} \mathcal{M}^{(1)*} \right| \right) \equiv \frac{1}{F} \int d\text{PS}_3 (\mathcal{B}_3 + \mathcal{V}_3) = \sigma_3^{NLO} \quad . \end{aligned} \quad (3.10)$$

It is worth noticing that we only include the interference with the tree-level diagrams and the loop-diagrams in the virtual contribution \mathcal{V}_3 , as the loop diagrams squared are formally of higher order in perturbation theory.

3.2.1 Ultraviolet Divergences And Renormalisation

When calculating observables with perturbative methods, we often come across divergent expressions in integrals. In this and the following section, I will explain how they are dealt with to obtain finite predictions in the end by using one example that is very popular in literature and can be found e.g. in [72]. These divergences can occur in the integrands of phase space integrals and in connection with loop diagrams. The Feynman rules tell us to integrate over the whole range of the loop momentum in these cases, and very often, these integrals then diverge. An example is depicted in Fig. 3.4, which corresponds to a correction of the photon propagator in QED. The corresponding matrix element is proportional to

$$\begin{aligned} i\Pi_2^{\mu\nu} &= -(-ie)^2 \int \frac{d^4k}{(2\pi)^4} \frac{i}{(p-k)^2 - m^2} \frac{i}{k^2 - m^2} \\ &\quad \times \text{Tr} \left[\gamma^\mu (\not{k} - \not{p} + m) \gamma^\nu (\not{k} + m) \right] \quad . \end{aligned} \quad (3.11)$$

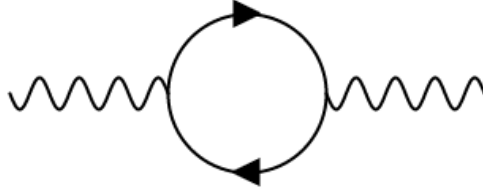


Figure 3.4: The Feynman diagram corresponding to *vacuum polarisation*, a one-loop correction to the photon propagator.

Here, p is the photon momentum, k and m are the momentum and the mass of the loop particle, γ^μ are the Dirac gamma matrices, and \not{a} is a shorthand notation of $\gamma^\mu a_\mu$ for any four vector a . When we integrate over the loop momentum k in this or a similar case, we can observe two different types of divergences. The integral can diverge in the infrared (IR) limit, i.e. for small values of $k \ll p$, but also for large values of $k \gg p$. We call this latter kind of divergences ultraviolet (UV) divergences.

At first glance, it might not look very physical that we come across divergent integrals when we calculate cross sections. To correspond to something that can be measured in experiments, an observable clearly needs to be finite. We will see in Sec. 3.2.2, when we take a closer look at IR divergences, that one possible solution to this dilemma is that some divergent contributions only appear in intermediate steps of the calculation, but not in the final result. However, this is generally not the case for UV divergences. For this reason, perturbative QFT had to face serious doubts in its early days. Only later it was discovered that the divergences can be dealt with by the procedures of *regularisation* and *renormalisation*. The concept behind these procedures is that a diagram like the one in Eq. (3.11) does not actually correspond to an observable quantity: from tree level diagrams, we are used to a direct correspondence between physical observables and the parameters of our theory, e.g. coupling constants. This does not hold when we include higher order corrections into our theory. Only if we were able to include all higher order corrections into our calculation, we would be able to relate the physical quantities to the original parameters, which we call *bare* parameters. From this point of view, UV divergences reflect our ignorance of higher order corrections. However, in the end, when we compute measurable quantities, the result must and will always be finite, and therefore is only dependent on finite parameters. The idea of regularisation is to deform the theory in the high-energy limit by introducing a *regulator* in such a way that the integrals of the form of Eq. (3.11) turn out finite and the infinite terms are absorbed by the regulator. Of course, physical predictions may not depend on the choice of our more or less arbitrarily introduced regulator. Finally, when performing renormalisation, we redefine physical observables in such a way that they only depend on finite quantities, and infinite parameters such as the bare coupling constants drop out. If all observables of a theory can be redefined in such a way, we call this theory renormalisable.

To show in some more detail how a regularisation and renormalisation procedure

works, we go back to the loop diagram of Fig. (3.4). On a side note, we now might realise that it actually corresponds to an effect called *vacuum polarisation* that was shortly mentioned in Sec. 3.1.1. It shows the creation of virtual e^+e^- pairs and how the vacuum is polarised similar to a dielectric in the presence of an electric charge. In the aforementioned section, we concluded that such an effect is responsible for a screening of the charge, leading to a decrease of the effective charge with higher distance. We are now able to relate this to our concept of physical and bare parameters.

In order to get rid of the UV divergence in Eq. (3.11), a very simple approach would be to just introduce a hard scale Λ as regulator at which we cut off the integral. The result would then depend on Λ and the original divergence would manifest when taking the limit $\Lambda \rightarrow \infty$. This regularisation scheme can actually be performed, but has some drawbacks in comparison to other methods, the most obvious probably being that it breaks the translational invariance of the integral. In this example, I want to introduce a different ansatz that turns out to be more useful for most realistic problems. It is based on the observation that many integrals in QFT would not be divergent if carried out in less than four dimensions. Actually, we can predict by simply counting the powers of the loop momentum k in an integrand whether the integral will diverge for $k \rightarrow \infty$ or not. In the regularisation scheme of *dimensional regularisation* (DREG) [73], the integration is therefore performed in $d = 4 - 2\epsilon$ dimensions.⁵ This reduces the power of k in the numerator, leading to a finite result for the integral. This result will depend on the regulator ϵ , and the original divergences will manifest in $1/\epsilon^n$ poles ($n \geq 1$). A very important feature of DREG is that it not only keeps the translational invariance of the integrals, but also respects Lorentz invariance and preserves the gauge symmetries of the theory. Moreover, it can also be used to regularise IR divergences as well (with $\epsilon < 0$).

If we use DREG for the integral in our example, we find after some steps that the result is

$$i\Pi_2^{\mu\nu} = \frac{-8e^2}{(4\pi)^{d/2}} (p^2 g^{\mu\nu} - p^\mu p^\nu) \Gamma\left(2 - \frac{d}{2}\right) \mu^{4-d} \times \int_0^1 dx x(1-x) \left(\frac{1}{m^2 - p^2 x(1-x)}\right)^{2-d/2}. \quad (3.12)$$

Here, we introduced a so-called *Feynman parameter* x , and $\Gamma(z)$ is the Euler gamma function, which has single poles at $z = -n \forall n \in \mathbb{N}_0$. The factor μ is a mass scale and must be introduced to compensate for the change in the mass dimension of the integral if integrating in $d \neq 4$. It has to be pointed out that μ is not to be interpreted as an upper bound like a cutoff would be, but should rather be of the order of typical invariants of the process. We can see that due to the pole structure of the Γ -function, we cannot just send $\epsilon \rightarrow 0$ and thereby go back to $d = 4$ dimensions. This is generally the case that we end up with after performing any form of regularisation. If for example, we had used a high-energy cutoff Λ to deal with a divergent integral of this kind, we would have obtained a result which would be proportional to Λ^n or $\log(\Lambda^n)$ and we could not go

⁵To avoid confusion, it should be noted that sometimes d is instead chosen to be $d = 4 - \epsilon$.

back to the limit $\Lambda \rightarrow \infty$. Nevertheless, we still want to be able to obtain results where the regulator drops out. This is where the next step of our procedure, renormalisation, takes place.

As pointed out before, including higher order corrections has made it more complicated or even impossible to relate physical observables to the bare parameters of the theory. When we were only working with tree-level diagrams, we could for example directly relate the photon propagator with the Fourier transformed Coulomb potential of an electron as $V(k^2) = e^2 k^{-2}$. This was a direct relation between e as a parameter of the theory and some measurable quantity. If we included the loop correction from Eq. (3.12), the expression for V would become infinite and our relation would be spoiled. Although we see that we cannot directly relate the (bare) parameters of the theory to our observables once we include loop corrections, we can simply define a *renormalised* charge, e_R , at a renormalisation scale μ_R by stating that $V(\mu_R^2) \equiv e_R^2 \mu_R^{-2}$. Since this is just a definition, it holds up to all orders. Such a *renormalisation condition* generally defines the renormalised quantity, e.g. e_R , by an observable that can be expressed in terms of the bare parameter, e.g. $e_R \equiv \mu_R^2 V(k^2 = \mu_R^2)$, and consequently expresses the renormalised parameter in terms of the bare one. Here, the bare parameter e clearly cannot have a finite value, since it has to compensate for the infinities coming from the loop integrals that enter the calculation of V . Nevertheless, our definition of e_R could be solved for e , and we could use the resulting expression to eliminate the bare charge e and the regulator ϵ in other observables that we want to calculate. Then, we have reached our goal of expressing measurable quantities only in terms of other measurable quantities. This is the core idea of renormalisation. We remember that we already briefly sketched this procedure when developing the renormalisation group equation to evolve the coupling constant of QCD, α_s , from one scale μ_0 to another scale μ_1 in sec. 3.1.1.

To make any calculation in a renormalisable QFT finite, we have to renormalise not only the coupling constants, but also any other parameter of the theory like masses and even the fields themselves. What we have sketched so far is known as *bare perturbation theory*, and can be summarised as follows:

1. To calculate any observable beyond LO in perturbation theory, we evaluate the corresponding diagrams using a regularisation scheme such as DREG.
2. Use the results to formulate renormalisation conditions at some scale μ_R that fix the relation between renormalised and bare parameters. In multiplicative renormalisation, which is explained here, we define the renormalised parameters by a product of (infinite) prefactors Z_i called the *renormalisation constants*, times the bare parameters.
3. Solve the relations from step 2 for the bare parameters and use the resulting expressions to eliminate them in the calculations from step 1.

While this recipe will work for any renormalisable QFT, it is relatively cumbersome for many higher order calculations. In practice, we rather use *renormalised perturbation theory*, which follows a slightly different recipe, but is based on the same grounds:

1. Take the Lagrangian \mathcal{L} of the theory with the bare parameters.
2. Use the same renormalisation conditions as in bare perturbation theory where we expressed the renormalised parameters using the renormalisation constants Z_i to rewrite the Lagrangian with the renormalised parameters.
3. By re-writing the renormalisation constants as $Z_i = 1 + \delta_i$, we can split the bare Lagrangian into two parts: $\mathcal{L} = \mathcal{L}_R + \delta\mathcal{L}$, where \mathcal{L}_R has the same form as \mathcal{L} . Here, we call the terms δ_i *counterterms* and $\delta\mathcal{L}$ the *counterterm Lagrangian*.
4. If we now compute observables, we have to perform our calculations based on the full Lagrangian \mathcal{L} , which will yield additional Feynman rules from $\delta\mathcal{L}$. The results will always be finite.

The same scheme can be used iteratively for higher order corrections with two or more loops. However, this is beyond the scope of this thesis.

Just as there are different regularisation schemes, there also exist several renormalisation schemes. While the counterterms in renormalised perturbation theory have to be chosen in such a way that they cancel the divergences from the loop integrals, we have a certain freedom left of how much of the finite part of the integrals we also include in the counterterms. I want to briefly review two of the most important schemes here. The first is known as *on-shell subtraction*, and while it offers a very intuitive interpretation of the Lagrangian, it is not always appropriate for practical calculations, especially in QCD. Basically, one can summarise the idea of the on-shell scheme by identifying the renormalised mass parameters m_R in the Lagrangian with the physically observed masses of the particles. For this purpose, the physical masses are defined as the location of the poles of the respective propagators. Using this scheme, we can link observables very easily to the input parameters of the theory – much like we have done with the electron charge in the example above. For the EW part of the SM, a complete set of the resulting renormalisation conditions for the physical sector can be found in a compact form for example in [74]. However, if we perform calculations in QCD, we have to deal with colour-charged particles. As we saw in section 3.1.1, a consequence of confinement is that these particles called partons will always appear in colour-neutral states, and consequently, we cannot measure the masses of isolated partons. Moreover, in the renormalisation of QED or the EW sector, the electric charge is usually defined in the *Thomson limit* of e^-e^- -scattering, that is at zero momentum transfer. For the renormalisation of the strong coupling constant on the other hand, we cannot properly define the Thomson limit. For these reasons, it is more suitable to use a different renormalisation scheme when the calculations include NLO-QCD corrections. A very common choice, probably the most common one, is the *minimal subtraction* (MS) or the *modified minimal subtraction* ($\overline{\text{MS}}$) scheme. These schemes, especially the $\overline{\text{MS}}$ scheme, fit the DREG scheme for regularisation perfectly. The idea behind MS is that the counterterms are chosen in such a way that they do not include any finite part. Instead, they take the minimal form possible, that is they only include the part proportional to $1/\epsilon$, with ϵ being the regulator from the DREG scheme. When regulating the one-loop contribution to the

QED photon propagator in that scheme, we came across the $\Gamma(\epsilon)$ function and had to take the limit of $\epsilon \rightarrow 0$. Expressions of this form occur very frequently in DREG, and in this limit we can expand the Γ function as

$$\lim_{\epsilon \rightarrow 0} \Gamma(\epsilon) = \frac{1}{\epsilon} - \gamma_E + \mathcal{O}(\epsilon) \quad ,$$

where $\gamma_E \approx 0.577$ is the *Euler-Mascheroni constant*. This is the origin of terms proportional to $1/\epsilon$. In the MS scheme, we define the counterterms δZ_i to include only these, whereas in the $\overline{\text{MS}}$ scheme, we also include terms proportional to $-\gamma_E$ and to $\ln(4\pi)$ which frequently occur together with the $1/\epsilon$ poles.

The choice of a renormalisation and a regularisation scheme for a calculation is often determined by several factors. As explained before, a very convenient scheme for QCD calculations is the $\overline{\text{MS}}$ scheme alongside with DREG to regularise UV and IR divergences (see next subsection for details on IR divergences). This choice is also very convenient since PDFs (see Sec. 3.1.1) are usually defined in the $\overline{\text{MS}}$ scheme. In EW calculations, however, another common choice is to use DREG and the $\overline{\text{MS}}$ scheme for regularisation and renormalisation of UV divergences, but to regularise IR divergences with small mass parameters (*mass regularisation*). In our implementation of the VBF process, we use the default setting of the program `RECOLA`, which is to choose DREG and the $\overline{\text{MS}}$ scheme for all parts of the calculations (see also sec. 5.2).

Before concluding this subsection on the renormalisation of UV divergences, I want to add a few remarks on the choice of the renormalisation scale μ_R . In the end, our NLO calculations will always depend on the choice of this scale. Unlike the cutoff scale we encountered when discussing regularisation, it is not to be understood as the limit up to which we expect our theory to work and which we want to be able to take to infinity in the end. Instead, it should be interpreted as a scale at which we define the renormalisation conditions. In DREG, when μ_R^2 is of the order of some scale Q^2 of the process, logarithms of the form $\ln(\mu_R^2/Q^2)$ in the results will drop out. It is thus typically chosen to be equal to kinematic invariants characteristic to the process at hand. Since this is very similar to the reasoning behind the choice of the factorisation scale μ_F , the (central values) of the two scales are often chosen to have the same value. Just like μ_F , the renormalisation scale μ_R is usually changed, e.g. by factors of (0.5 to 2), to obtain an estimate of the uncertainty related to the process of renormalisation. It seems natural to interpret this uncertainty as an effect of truncating the perturbative series at some fixed order, e.g. at NLO. However, for many processes, it turns out that including one additional order of some coupling leads to corrections that significantly exceed the scale uncertainty at the original perturbative order. These estimates therefore should be taken with a pinch of salt, but they can still be a good first indication whether including an additional order in perturbation theory actually reduces the theoretical uncertainty.

3.2.2 Infrared Divergences

At the beginning of this section, when we took a closer look at the behaviour of loop integrals, we recognised that they can not only diverge for large loop momenta $k_0 \rightarrow \infty$,

but also in the low energy regime, a behaviour which we called IR divergence. More precisely, we will call the low-energy divergences for $k_0 \rightarrow 0$ *soft* divergences. They are not unique to virtual corrections: we remember that when we calculate the full NLO cross section for a process, we also have to include real emission corrections, i.e. the radiation of one additional (massless) particle. These corrections also lead to IR divergences: If the emitted particle j becomes soft, $p_j^2 \rightarrow 0$, or approaches the limit where it moves collinear to its emitter particle i , $p_i \cdot p_j \rightarrow 0$ (*collinear* divergence), this cross section diverges as well. We will encounter this divergent behaviour in any QFT with massless gauge bosons, i.e. especially in QCD and in QED. The general treatment of these IR divergences will be explained briefly in this subsection, following arguments from [72, 75].

The effect of IR divergences even has a physical interpretation: experimentally, we will never be able to distinguish one massless particle in the final state, e.g. a quark, from the same final state particle accompanied by another massless particle, e.g. a photon or gluon, with very small momentum or moving collinear to the original particle. The original particle cannot be distinguished from the cloud of low-energy particles surrounding it.

However, as with UV divergences, we expect physical observables to only take finite values, and therefore also expect to obtain finite results when calculating them. Indeed, it turns out that we will obtain IR finite results for so-called IR safe observables if we include both the virtual and the real emission corrections at a given order in perturbation theory. In QED, this is the statement of the *Bloch-Nordsieck* theorem [76]: by summing all photon loop corrections and the corrections corresponding to photon bremsstrahlung in the final state, the resulting calculation will be IR finite at all orders. More generally, the *Kinoshita-Lee-Nauenberg theorem* (KLN) [77, 78] states that in any unitary QFT, IR singularities between the virtual and real emission corrections cancel for suitable quantities if we include all possible initial *and* final states that yield soft or collinear singularities to a given observable. In this context, a suitable observable is one that meets the requirements of *infrared safety*, which means that it must not depend on the IR limit of the theory. In practice, an observable \mathcal{O} which depends on any momentum p is called infrared safe if in the collinear or soft limit of the splitting $p \rightarrow p' + k$, that is for $p'_0 \rightarrow 0$, $k_0 \rightarrow 0$ or for $p' \cdot k \rightarrow 0$, \mathcal{O} approaches the value it takes if no splitting takes place. I will give a more formal definition of IR safety at the end of this section.

In NLO-QCD calculations, the concept of IR safety is closely entangled with the idea of *jets*. As explained above, we cannot expect every observable sensitive to final state radiation to always take on finite values. Let us take for example the VBF scattering process $us \rightarrow Hdc$. Here, we have to include the real emission contributions in NLO, corresponding for example to $us \rightarrow Hdc + g$. If we wanted for example to measure the differential cross section $d\sigma/dp_{T,c}$ of the transverse momentum of the c quark, we could not expect the cross section to remain finite, since the value of this observable does not agree between the case of no splitting $c \rightarrow cg$ and the soft/collinear limit of this splitting. On the other hand, a detector in a collider experiment will only have a finite spatial resolution, so a very soft or collinear splitting will look as if no splitting at all has taken place.

All these considerations do not even take into account the fact yet that any parton

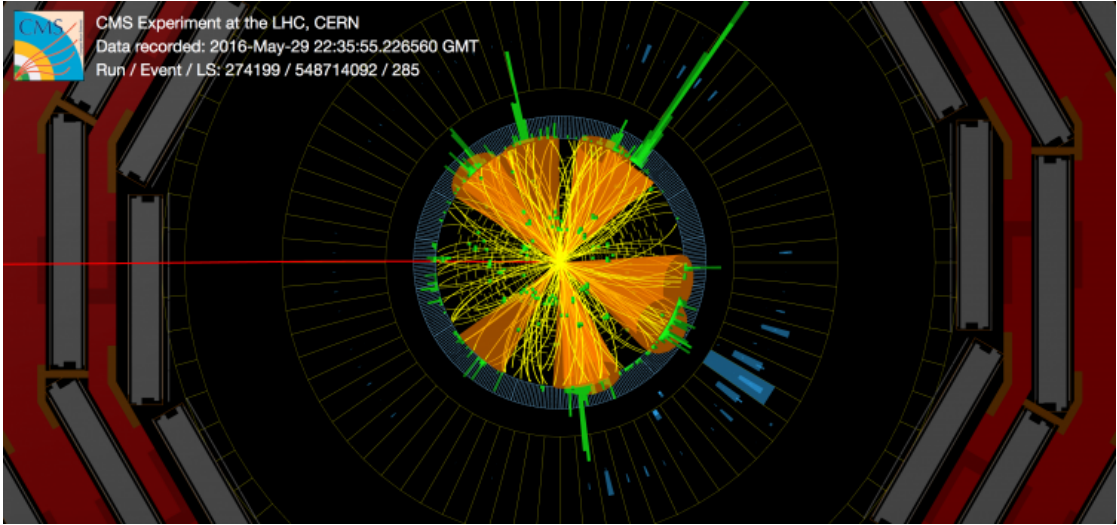


Figure 3.5: Visualisation of a candidate event for $t\bar{t}t\bar{t}$ production at the CMS experiment at the LHC, CERN. Image taken from [79].

will never be detected as an isolated particle in a detector due to confinement. Instead, our discussion of QCD in the low-energy regime in Sec. 3.1.1 revealed that strongly charged particles may excite new particles from the vacuum when being separated to long distances. These bunches of particles (jets) will then form bound states, i.e. hadrons, and will hit the detector in roughly the same direction (we will discuss the possibilities for the numerical simulations of this part of collision event in Sec. 3.3). A visualisation of how such an event ‘looks’ like at the CMS detector of LHC at CERN is depicted in Fig. 3.5. Summarising these considerations, we see that it would be favourable to define a prescription for how to consistently group together particles hitting the detector in the same area and thereby find an IR safe definition for a jet. For these purposes, a large variety of jet algorithms exists. For our analysis (see chapter 6.1), we use the so-called anti- k_T algorithm [80]. This algorithm works as follows:

1. For every particle i in the final state, calculate the distance d_{ij} to every other particle j , and to the beam axis B , which is usually taken to be the \hat{e}_z axis. This distance is defined by

$$d_{ij} = \min\left(p_{T,i}^{2k}, p_{T,j}^{2k}\right) \cdot \frac{\Delta R_{ij}^2}{R^2} \quad , \quad (3.13)$$

with $k = -1$ and

$$\Delta R_{ij}^2 = (y_i - y_j)^2 + (\phi_i - \phi_j)^2 \quad . \quad (3.14)$$

Here, $y_i = \ln \frac{E+p_z}{E-p_z}$ is the rapidity of particle i , ϕ_i is its azimuthal angle and R is a radius parameter. R can be interpreted as the minimal distance between two distinct jets and is typically set to values around $R = 0.5$.

2. If for some particle j the distance d_{ij} is lower than d_{iB} , combine i and j and replace them by the resulting entity $i + j$ in the list of particles.
3. If d_{iB} is minimal, i is removed from the list of particles and called a jet.
4. Repeat until no particles are left.

This jet algorithm is IR-safe and comparably fast, which is why it is probably the most commonly used algorithm nowadays. Moreover, the jets built with the anti- k_T algorithm can be easily interpreted geometrically. It can be applied on simulated and on real detector events, and both the CMS and the ATLAS experiment use it for jet reconstruction [81]. The anti- k_T algorithm belongs to a broader class of jet algorithms, the sequential recombination algorithms. Other representatives of this class are the k_T algorithm, which uses the same scheme, but with $k = +1$ in the definition of d_{ij} in Eq. (3.13), and the Cambridge-Aachen algorithm, corresponding to $k = 0$.

By employing a jet algorithm, we make use of the fact that our detectors have a finite spatial and energy resolution, and effectively use this finiteness as an IR regulator for the real emission cross section in the final state. In practice, regulating the soft and collinear divergences in calculations is better done by other methods, for example by giving the particles a very small but finite mass (mass regularisation) or by employing the DREG scheme. As mentioned before, IR divergent integrals can be regularised in $d = 4 - 2\epsilon$ dimensions with $\epsilon < 0$, which is the method used for example by the amplitude generator RECOLA in our calculation.

Finally, we figured out how to define infrared-safe observables. For QED corrections, as stated by the Bloch-Nordsieck theorem mentioned above, including final state real emission corrections is enough for cancelling IR divergences to all orders. But we also learned that the KLN theorem states that for a cancellation at least for IR safe observables in any unitary theory, we should also sum over initial state radiation. In practice, we already achieved this by a re-definition of our initial state using PDFs in Sec. 3.1.1. We effectively absorb the divergent part of the initial state into the definition of the PDFs, which cannot be calculated. The remaining part of the cross section, happening at a different momentum scale $Q^2 > \mu_F$, remains finite. From this point of view, the (unphysical) factorisation scale μ_F serves as a regulator for the initial state radiation.

Now, we should be able to calculate finite cross sections for appropriate observables and the IR divergences should cancel between virtual and real contributions. However, a problem arises in nearly every calculation in practice: we generally cannot evaluate the phase space integrals analytically, but have to employ numerical integration methods. With these methods, the exact cancellation between the virtual and the real divergences becomes cumbersome, because the respective contributions are evaluated separately in different phase spaces, namely in the n -particle phase space for the virtual and in the $n + 1$ -particle phase space for the real emission corrections (in our case of the VBF process, $n = 3$). At the same time, numerical integration requires finite quantities, so we cannot simply evaluate the two integrals one by one and then hope for their sum to be finite. Instead, we have to get rid of the divergences before integrating. One possible method is called subtraction method and is based on the idea that we can make these

contributions finite by adding and subtracting a counterterm in a suitable way. Each of these counterterms \mathcal{C}_{n+1} acts on the one particle radiation phase space $d\text{PS}_{rad}$ and must fulfil two important properties: it must have the same singular behaviour as the real amplitude squared \mathcal{R}_{n+1} , and it must be (analytically) integrable over $d\text{PS}_{rad}$. Then it can be subtracted from \mathcal{R}_{n+1} , and its integral $\mathcal{I}_n = \int d\text{PS}_{rad} \mathcal{C}_{n+1}$ can be added to \mathcal{V}_n , to cancel the soft and collinear singularities properly:

$$\sigma_{NLO} = \int d\text{PS}_n (\mathcal{B}_n + \mathcal{V}_n + \mathcal{I}_n) + \int d\text{PS}_{n+1} (\mathcal{R}_{n+1} - \mathcal{C}_{n+1}) \quad (3.15)$$

Since we demand \mathcal{C}_{n+1} to be analytically integrable over the one-particle phase space, the singular behaviour will not spoil the calculation any more and both integrals become finite before numerical integration. To determine appropriate counterterms is a cumbersome task, and several ansatzes are available. One of them, the *Frixione-Kunszt-Signer* (FKS) subtraction method [75, 82], is also employed in the POWHEG BOX program which is used for our calculations (see Sec. 3.3.1), and thus will be explained here very briefly.

The FKS method introduces a measurement function \mathcal{S} , which relates the momenta of observable jets to the partonic momenta. More explicitly, in a process with n partons in the Born final state, \mathcal{S}_n is used to define the jet momenta in terms of the n (leading order) parton momenta and \mathcal{S}_{n+1} to define them in terms of the $n+1$ -body partonic kinematics [82]. The condition that the total cross section must be finite for IR safe observables can be now expressed more formally using the measurement functions:

$$\begin{aligned} \lim_{p_i^0 \rightarrow 0} \mathcal{S}_{n+1} &= \mathcal{S}_n, \\ \lim_{p_i \parallel p_j} \mathcal{S}_{n+1} &= \mathcal{S}_n, \\ \lim_{p_i \parallel p_{a/b}} \mathcal{S}_{n+1} &= \mathcal{S}_n, \\ \forall 1 \leq i, j \leq n+1, \quad i \neq j \quad . \end{aligned}$$

Here, p_a, p_b are the incoming parton momenta. We then decompose the phase space in *single-singular* regions, that is regions which by definition have one soft or collinear singularity at most. This is done by the following definition of $\mathcal{S}_n + 1$:

$$\mathcal{S}_{n+1} = \sum_i = 1^{n+1} \left(\mathcal{S}_i^{(0)} + \sum_{j=1, j \neq i}^{n+1} \mathcal{S}_{ij} \theta(p_{T,j}^2 - p_{T,i}^2) \right) ,$$

where we define

$$\begin{aligned} \mathcal{S}_i^{(0)} \neq 0 &\Leftrightarrow p_i^0 \rightarrow 0, \vec{p}_i \parallel \vec{p}_a, \vec{p}_i \parallel \vec{p}_b \\ \mathcal{S}_{ij}^{(0)} \neq 0 &\Leftrightarrow p_i^0 \rightarrow 0, p_j^0 \rightarrow 0, \vec{p}_i \parallel \vec{p}_j \quad . \end{aligned}$$

This definition also gives us the freedom of redefining \mathcal{S}_i and \mathcal{S}_{ij} by any terms which vanish in the IR limits. We finally redefine our definition of the n and the $n+1$ cross

sections by inserting the definitions of the measurement \mathcal{S} and obtain

$$\sigma_{NLO} = \sigma_{NLO}^{(n)} + \sigma_{NLO}^{(n+1)} \quad (3.16)$$

$$= \int d\text{PS}_n (\mathcal{B}_n + \mathcal{V}_n) \mathcal{S}_n + \int d\text{PS}_{n+1} (\mathcal{R}_{n+1}) \mathcal{S}_{n+1} \quad . \quad (3.17)$$

In this expression, both integrands are now finite and can be integrated numerically.

At this point, since our process includes calculations of matrix elements at NLO-EW, a final remark on EW radiative corrections is in order. Unlike QCD and QED, the full EW sector of the SM contains massive vector bosons $V = W^\pm, Z$. This is important for the calculation of virtual one-loop corrections. In the discussion of IR singularities in theories with massless bosons in the previous section, I mentioned that these singularities can be regularised for example by the introduction of a small mass for the loop particle, i.e. the photon or gluon. The singularities then manifest themselves as logarithms of the ratio of the momentum transfer over the regulator mass. For EW loop corrections, the boson masses play the role of a ‘natural’ regulator for the loop integrals, and the would-be singular regions manifest themselves as $\log(Q^2/M_{W,Z}^2)$. In the limit of a large momentum transfer, the squared gauge boson masses can be neglected against Q^2 and these terms behave like the IR limit $M_{W,Z} \rightarrow 0$ of the loops. As I will discuss in Sec. 4, these Sudakov logarithms are responsible for sizeable effects of EW corrections in some kinematic regions of scattering events, namely at high transverse momenta.

3.3 Parton Showers

In the previous sections, we have seen how to perform a cross section calculation of a hard process at fixed order with perturbative methods. This lets us compute results for inclusive cross sections, but no matter how many orders of the perturbative expansion we include, we will never be able to get predictions for arbitrary exclusive cross sections. The reason is that we will always have to sum over different final states to cancel IR divergences according to the KLN theorem.

At the same time, the final state as modelled by the hard process is not a realistic experimental final state. The highly energetic partons will radiate photons (bremsstrahlung) and gluons. Formally, these additional radiations are of higher order in perturbation theory and thus suppressed by powers of α or α_s . Nevertheless, in the collinear and/or the soft region, the radiation is kinematically enhanced by logarithmic factors and cannot be neglected when an accurate description of the final state is desired. In QCD, another important aspect that has to be considered is the increase of α_s with the energy of the final state particles decreasing. Thus, while a particle loses energy through radiation, subsequent radiation is actually less suppressed, until we eventually even leave the perturbative regime at some point. At this scale, which is usually taken to be at around 1 GeV, the process of hadronisation sets in, which will be very briefly discussed at the end of this section.

To calculate exclusive quantities and to obtain a more realistic final state, the resummation of the leading logarithms (LL) of infinitely many Feynman diagrams would

be necessary. This happens in a parton shower (PS) generator, which uses probabilistic methods and is based on the concept of unitarity, as I will discuss below. While both QED and QCD showers exist and are actually used in our calculations (see Sec. 6.1), QCD showers have played a more important role for most calculations so far. Therefore, I will use the QCD case to describe how a PS works in general. Most of the underlying principles can easily be generalised and extended to the QED case as well. The arguments presented here follow explanations that are given e.g. in [83, 54].

We consider a final state parton i of the hard process, which, w.l.o.g., we assume to be a quark. The differential probability dP of this parton splitting into two partons j, k , e.g. for the splitting $q \rightarrow q + g$, is given by the Altarelli-Parisi splitting kernels $\hat{P}_{ji}(z)$ ⁶ in the almost-collinear regime of small emission angles:

$$dP = \frac{\alpha_s}{2\pi} \sum_j \hat{P}_{ji}(z) \frac{1}{t} dt dz \equiv F(z, t) dt dz \quad (3.18)$$

The splitting kernels, which we already encountered during the discussion of PDFs and the DGLAP equations for the evolution of α_s in Sec. 3.1.1, depend on the fraction z of the energy E_i of parton i that parton j takes away, i.e. $E_j = zE_i, E_k = (1-z)E_i$. The variable t is defined as $t := E_i^2 \theta^2$, with θ being the opening angle of the splitting. At every step in the evolution, the running of α_s is taken into account by evolving it to the scale $Q = \theta(1-z)zE$. The explicit form of the splitting kernels is as follows [64]:

$$\begin{aligned} \hat{P}_{qq}(z) &= \frac{4}{3} \frac{1+z^2}{1-z} \quad , \\ \hat{P}_{gg}(z) &= 3 \frac{(1-z(1-z))^2}{z(1-z)} \quad , \\ \hat{P}_{qg}(z) &= \frac{N_f}{2} (z^2 + (1-z)^2) \quad , \\ \hat{P}_{gq}(z) &= \frac{4}{3} \frac{1+(1-z)^2}{z} \quad . \end{aligned}$$

The notation $\hat{P}_{ji}(z)$ is to be understood as ‘a particle of type i is radiating a particle of type j , which carries the energy fraction z ’. N_f denotes the number of active flavours.

The PS algorithm can be understood as a repeated application of Eq. (3.18) where the splittings are ordered in some evolution variable. This could be the opening angle θ or some related variable such as t , or e.g. the virtuality q at which the splitting takes place. It is important that the evolution variable is chosen such that the dominant contribution will come from configurations where the splittings are indeed ordered in the variable. The algorithm now starts at an initial value in this variable, corresponding to the hard process, and evolves down to some variable which corresponds to the limit in which additional splittings cannot be resolved any more. The core idea behind the algorithm is based on the argument of unitarity: Without using any knowledge on the form of the

⁶Sometimes, the splitting kernels are given with their full dependence on the azimuthal angle ϕ of the splitting. Here, I consider them to be averaged over ϕ .

splitting probability, we can say that the sum of the probabilities for *no* splitting taking place between some values t_I and t_0 of the evolution variable and a splitting actually taking place at some $t \in [t_I, t_0]$ must be equal to 1. If we denote the probability for no splitting as $\Delta(t_I, t_0)$, we can express this argument more formally by stating that

$$1 = \Delta(t_I, t_0) + \int_{t_0}^{t_I} dt \int_0^1 dz \Delta(t_I, t) F(z, t) \quad .$$

Here, $\Delta(t_I, t) F(z, t)$ is to be interpreted as the probability that the *first* splitting takes place at t with momentum fraction z , i.e. that no other splitting has taken place at another $t' \in [t_I, t]$ before. This equation can be solved by making use of the fact that $\Delta(t_1, t_2) = \Delta(t_1, t_0) / \Delta(t_2, t_0)$ for any $t_1 > t_2$, and we obtain

$$\Delta(t, t_0) = \exp \left\{ - \int_{t_0}^t \frac{dt'}{t'} \int_0^1 dz \frac{\alpha_s}{2\pi} \hat{P}_{ji}(z) \right\} \quad . \quad (3.19)$$

This expression is called the *Sudakov form factor*. We can now implement the procedure for generating radiation ordered in the evolution value t as a probabilistic algorithm:

1. We take parton i and start with an initial value of the evolution variable t_I given by the hard process. We also define a lower cutoff t_0 , which is the minimum t for a resolvable branching. This implicitly also defines limits for the values z can take.
2. A random number $x \in [0, 1]$ is generated (uniformly) and the equation $\Delta(t_I, t) = x$ is solved for t .
3. If $t_1 < t_0$, we say that the splitting was not resolvable and the algorithm is terminated for parton i .
4. If $t_1 \geq t_0$, we perform the splitting $i \rightarrow j + k$. The value of z at which the splitting takes places is also chosen randomly, with a probability according to the distribution defined by $\hat{P}_{ji}(z)$.
5. Now, repeat the same algorithm, starting at step 2, for the partons j and k , but with $t_I \rightarrow t_1$.

This iterative algorithm is repeated until no more resolvable splitting can be found. The final state momenta can then be passed to the next step of the event generation process or to an analysis routine. Usually, also some reshuffling of the final state momenta takes place after the shower. The reason is that the final state particles of the hard process are usually assumed to be on their mass shell, while the parton shower starts with highly virtual, i.e. off-shell momenta. Through means of this reshuffling, a PS can also affect observables related to particles not actually participating in the shower process.

The choice of using the opening angle θ as evolution variable is not completely arbitrary. As outlined before, many choices of the evolution variable are possible, and they are equivalent w.r.t. their treatment of collinear emissions. However, also the soft emission of gluons is kinematically enhanced, and angular-ordered showers promise to

treat these radiations coherently (*coherent showering*). The argument is that after a splitting $i \rightarrow j + k$ at an angle θ_1 , the pair $j + k$ cannot be resolved at angles larger than θ_1 and radiation with $\theta > \theta_1$ should be generated as coming from the unresolved pair. This radiation would be equivalent to coming from the ‘mother particle’ i . With angular-ordered showers, these emissions must – per definition – have been generated before the splitting, i.e. they are in fact generated as radiation from i . A more detailed discussion of the effects of coherent showering is found e.g. in [64].

For some processes, for example for the EW production of Hjj within the VBF approximation, an alternative treatment of the shower can be useful, which is *dipole showering*. This concept is based on the fact that most Monte Carlo generators work in the so-called *large N_C limit*, where N_C is the number of colours: here, the event is treated as the sum of distinct colour flows. To ensure colour conservation, each incoming colour-charged particle must have a closed colour flow to a ‘colour partner’, which can either be another incoming particle carrying the respective anti-charge or an outgoing particle carrying away the same colour charge. Each pair of ‘colour partners’ can be treated as a dipole by the SMC, and the emission of a gluon would then be treated as the splitting into two dipoles. This has the advantage that the partons do not need to be off-shell to ensure momentum conservation during the PS since every emission is a $2 \rightarrow 3$ instead of a $1 \rightarrow 2$ process. Furthermore, it leads to a different distribution of the recoil of the emitted parton. For processes like deep inelastic scattering (DIS), this recoil distribution is actually closer to the physical reality than the global recoil distribution in a classical PS. From this point of view, the VBF process can be regarded as a ‘double Deep inelastic scattering (DIS)’ process, since no colour flow between the two final state partons exists. It turns out [84] and has been confirmed in one of our earlier studies [1] that the radiation pattern generated by a dipole shower is indeed closer to what is expected for additional radiation by higher-order calculations, especially in the central rapidity region. A more detailed discussion on how this statement holds with additional HV contributions is part of our phenomenological analysis that I present in chapter 6.

The procedure described above can be directly applied for a final state PS. For an initial state shower, the situation is slightly more complicated. Naively, we could simply start with initial state partons at some momenta, drawn randomly according to the PDFs at a shower starting scale, and feed them to a PS algorithm until they reach the scale of the hard process. In this case, we would have very little control over the distribution of the momenta at the beginning of the hard process, which would probably spoil the Monte Carlo efficiency. If, for example, we want to probe a HV production process like $q\bar{q} \rightarrow Z \rightarrow q'\bar{q}'H$, we would expect the cross section to peak where the invariant mass of the parton pair is close to the Z mass. Starting with momenta coming from a shower algorithm, we’d have very little chance to probe exactly this region. For this and other reasons, it is common to use a backward evolution for initial state showers. That means that the initial state momenta are drawn according to the probability distribution suitable for the hard process, with the PDFs being evaluated at the hard process scale, and the shower is evolved backwards, i.e. the partons gain energy in every emission until

they reach the low scale of the hadron. The only modification to the shower algorithm necessary is a modification to the Sudakov form factor: it is multiplied by the ratio of the PDFs at the shower starting scale over the PDFs at the hard scale to properly account for the probability of no splitting taking place.

The same programs which are used for generating the shower can usually be used to perform some other steps missing for a complete simulation of an event. This can best be explained using the sketch of Fig. 3.6. Here, a (fictitious) event from a hadron collider is depicted, with all the parts that should be covered by a complete simulation. So far, we have discussed the inner structure of the incoming hadrons, which is described by the PDFs, the initial state shower, the hard scattering process, and the final state PS. This description is missing two important parts before it can be fit to actual collider events: first, due to their composite nature, the hadrons will leave behind *beam remnants*. Even if those do not interact further, they have to be connected to the rest of the event to satisfy momentum, charge and colour conservation. Furthermore, other partons from the hadrons can interact as well, even though the majority of these interactions usually happens at lower energy scales than the hard process (soft or semi-soft collisions) since the probability of finding two partons per hadron with high momentum fraction x is strongly suppressed by the PDFs. The treatment of the remnants and this *underlying event* is usually also performed (phenomenologically) by the same programs that are used to simulate the PS. The second part we were missing in our description so far is what happens to the final state partons after the shower. As mentioned before, the shower stops when a scale or emission angle is reached at which either non-perturbative effects take over or where the detector resolution could not resolve further splittings. At this point, we still deal with colour-charged partons, whereas in the experiment we would detect hadrons or even their decay products with net-zero colour charge. The *hadronisation* process where the partons enter bound states can only be described phenomenologically and by employing very general features. The simulation is usually also based on the fact that particles have specific colour partners when working in the large N_C limit. Two main concepts for hadronisation, string and cluster models [85, 86], exist, which shall not be discussed further here. Our process can be interfaced with Monte Carlo programs which can also model hadronisation effects and particle decays, but their implementation is not process-specific and was thus not subject to our work. I refer the interested reader to the comprehensive overview in [87].

3.3.1 The POWHEG Method

In this chapter, I have shown two separate ideas to improve a LO calculation of a cross section for some scattering process: on the one hand, one can include higher order corrections (primarily NLO corrections), and on the other hand, one can use a SMC. While the former ansatz improves the precision for certain inclusive quantities, the latter promises to refine the description of exclusive quantities by resumming divergent logarithmic contributions in the LL approximation. This makes NLO calculations an ideal tool to test the predictions of the SM at very high precision, but calculations with a PS are more suited for experimental analyses, which often depend on exclusive quantities.

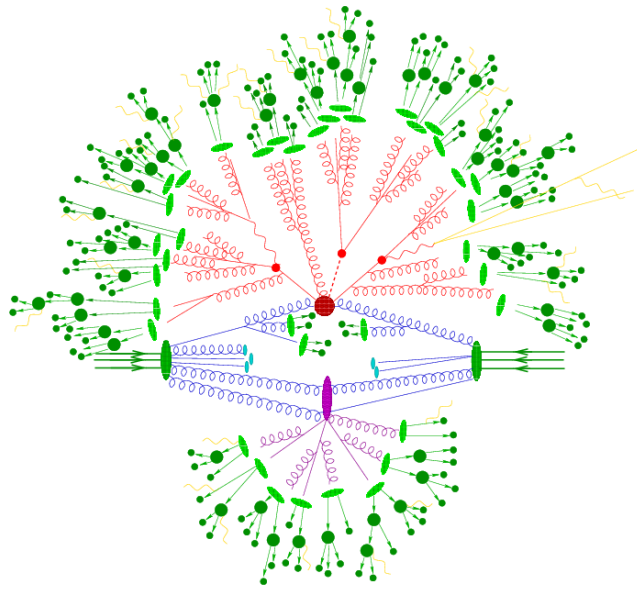


Figure 3.6: The different parts of a simulated hadronic event: the incoming hadrons are depicted as dark-green shaded blobs, dark blue lines correspond to the initial state parton shower, the light blue blobs are beam remnants, the dark red blob is the actual hard scattering process. The light red lines correspond to the final state shower, with light green blobs representing hadronisation and the dark green part depicting hadron decays. The purple part corresponds to the *underlying event* part. Figure taken from [88].

From this point of view, it seems appealing to combine the two concepts and perform calculations at NLO+PS precision. However, it turns out that this matching is actually not trivial at all. The reason is that just adding a PS to the result of an NLO calculation would lead to a double-counting of some contributions in the soft-collinear region, i.e. the shower would include some configurations that are already covered by the real emission contributions of the NLO calculation.

The first concept for the matching of NLO calculations to showers was the MC@NLO approach [89]. Its basic idea is to subtract the approximate NLO cross section that is given by the shower from the exact NLO calculation. These analytically computed *MC subtraction terms* are process-independent, but do depend on the implementation of the PS and thus have to be computed once for every SMC. Moreover, the result of the exact NLO calculation minus the MC subtraction terms is not guaranteed to be positive, leading to a significant share of the events being generated with (unphysical) negative weights [55]. In [54], a ‘new method for combining NLO-QCD with shower Monte Carlo algorithms’ was proposed. The strategy that this method, which later received the name POWHEG (**P**ositive **W**eight **H**ardest **E**mission **G**enerator) and is explained in more detail in [55], follows is to generate the hardest emission first at full NLO accuracy and let the shower only generate emissions of lower p_T than this. I want to briefly summarise the POWHEG formalism in the following, adapting the detailed explanations from [54, 55] to the notation used in this thesis. For the sake of simplicity, we assume that a p_T ordered shower is used. It is shown in [54] that the formulae shown in the following can be generalised to angular-ordered SMCs by using a so called *vetoed-truncated* PS.

In order to sketch the idea behind the POWHEG method, I start by expressing the differential cross section after matching a shower to a LO fixed-order calculation analogously to the NLO cross section of Eq. (3.15):

$$\begin{aligned} d\sigma_{LO,SMC} = & \sigma_{LO} (\Delta(t_I, t_0) + dt dz \Delta(t_I, t) F(z, t) \\ & \times (\Delta(t, t_0) + dt' dz' \Delta(t, t') F(z, t') \times (\dots))) \quad . \end{aligned} \quad (3.20)$$

At this point, I want to recall that the POWHEG method assumes a p_T ordered shower. As shown in the original publication [54], a p_T veto can simply be implemented by using the following modified Sudakov form factor:

$$\Delta_{p_T}(t, p_T) = \exp \left(- \int_{t_0}^t dt' \int_0^1 dz F(z, t') \theta(z(1-z)\sqrt{t'} - p_T) \right) \quad . \quad (3.21)$$

Using this Sudakov factor, we can write down an expression for the first shower emission:

$$d\sigma = d\sigma_{LO} (\Delta_{p_T}(t_I, p_T) + dt dz \Delta_{p_T}(t_I, p_T) F(z, t) \theta(t_I - t)) \quad . \quad (3.22)$$

which is equivalent to the following expression at $\mathcal{O}(\alpha_s)$:

$$\begin{aligned} d\sigma = & d\sigma_{LO} \left(1 - \int_{t_0}^{t_I} dt' \int_0^1 dz' F(z', t') + F(z, t) \theta(t_I - t) dt dz \right) + \mathcal{O}(\alpha_s^2) \\ = & d\sigma_{LO} (1 + F(z, t)_+ \theta(t_I - t) dz dt) + \mathcal{O}(\alpha_s^2) \quad . \end{aligned} \quad (3.23)$$

In the second line of Eq. (3.23), I have made use of the *+prescription* to regulate the singularities in t and z in the splitting kernel, which is defined as:

$$f(z)_+ := f(z) - \delta(1-z) \int_0^1 f(z') dz' \quad .$$

The expression of Eq. (3.23) can now be compared to the NLO cross section of Eq. (3.15), which can be rewritten as:

$$\begin{aligned} d\sigma_{NLO} &= d\text{PS}_n (\mathcal{B}_n + \mathcal{V}_n + \mathcal{I}_n) + d\text{PS}_{n+1} (\mathcal{R}_{n+1} - \mathcal{C}_{n+1} \mathbb{P}) \\ &= d\text{PS}_n (\mathcal{V}_n^* + (\mathcal{R}_{n+1} - \mathcal{C}_{n+1}) d\text{PS}_{rad}) \\ &\quad + \mathcal{B}_n \left(1 + \frac{\mathcal{R}_{n+1}}{\mathcal{B}_n} (1 - \mathbb{P} d\text{PS}_{rad}) \right) \text{PS}_n \quad . \end{aligned} \quad (3.24)$$

Here, \mathbb{P} is simply a projection of the $n+1$ particle phase space on the n particle phase space in the singular region, and \mathcal{V}_n^* is a shorthand notation for $\mathcal{V}_n + \mathcal{I}_n$. On comparing the last line of this expression to Eq. (3.23), the reader may notice that if we adapt Eq. (3.20) in a clever way, we obtain the exact expression at NLO. This is achieved by replacing the splitting kernel for the hardest splitting by the ratio between the real and the born matrix elements, $F(t) \rightarrow \frac{\mathcal{R}_{n+1}}{\mathcal{B}_n}$ and by replacing the Sudakov form factor through the p_T -ordered *POWHEG Sudakov form factor*:

$$\Delta_{NLO}(p_T) \equiv \exp \left(- \int d\text{PS}_{rad} \frac{\mathcal{R}_{n+1}}{\mathcal{B}_n} \theta(p_T^n - p_T^{n+1}) \right) \quad . \quad (3.25)$$

Using this, we can now write the *POWHEG master formula* for an NLO-exact cross section that can be matched to a PS:

$$\sigma = \int d\text{PS}_n \tilde{\mathcal{B}}_n \Delta_{NLO}(p_T^{\min}) + \int d\text{PS}_{n+1} \tilde{\mathcal{B}}_n \Delta_{NLO}(p_T) \frac{\mathcal{R}_{n+1}}{\mathcal{B}_n} \theta(p_T^n - p_T^{n+1}) \quad , \quad (3.26)$$

with

$$\tilde{\mathcal{B}}_n := \mathcal{B}_n + \mathcal{V}_n + \int d\text{PS}_{rad} \mathcal{C}_{n+1} + \int d\text{PS}_{rad} (\mathcal{R}_{n+1} - \mathcal{C}_{n+1}) \quad . \quad (3.27)$$

If this implementation is matched to a shower with any additional radiation not having a harder p_T than the first emission, it is guaranteed that no double-counting appears and the first emission is generated with NLO accuracy.

Chapter 4

The EW Hjj Production Process

In the SM, the Higgs boson can be produced by several different modes at colliders (see Fig. 4.1). However, since the Higgs only has significant couplings to the W and Z bosons as well as to the top quark t , the number of production channels with significant production rates is very limited. At a proton-proton collider, e.g. the LHC, the production is largely dominated by gluon fusion processes (ggF) of the form $gg \rightarrow H$, accounting for a cross section of $\sigma_{ggF} = 54.67 \text{ pb}_{-6.7\%}^{+4.6\%}$ ¹ at a hadronic center of mass energy $\sqrt{S} = 14 \text{ TeV}$. The second most important production mode is vector boson fusion (VBF), an electroweak production mode of the form $pp \rightarrow Hjj$ where the two partons scatter via the t - or u -channel exchange of a vector boson, which accounts for $\sigma_{\text{VBF}} = 4278 \text{ fb}_{-0.3\%}^{+0.5\%}$ at the same collision energy. In this notation, j stands for a partonic jet. Other contributions with sizeable cross sections are Higgsstrahlung processes (HV) of the form $pp \rightarrow HV$, where a Higgs is produced in association with a W ($\sigma_{HW} = 1513 \text{ fb}_{-0.7\%}^{+0.4\%}$) or a Z boson ($\sigma_{HZ} = 842 \text{ fb}_{-0.7\%}^{+0.4\%}$ ²), as well as associated production with a pair of top quarks, $pp \rightarrow t\bar{t}H$, contributing with a total cross section of $\sigma_{t\bar{t}H} = 614 \text{ fb}_{-9.2\%}^{+6\%}$. From this listing, it may seem that the EW production of a Higgs, consisting of the VBF and the HV production modes, only plays a minor role in comparison to the QCD-induced production modes. However, these processes have strongly benefited from the higher center-of-mass energy of the LHC recently, and they are expected to become even more important with the ongoing upgrade of the LHC for even higher luminosities (HL-LHC). More importantly, as will be explained in this chapter, they benefit from a very good signal to background ration in detectors if appropriate cuts are applied, and they prove to be a useful tool in the exploration of BSM physics in the Higgs sector.

Usually, VBF is defined as a class of processes where a quark or anti-quark scatters with another (anti-)quark via the space-like exchange of a vector boson $V = W^\pm, Z$. The Higgs boson is then emitted from this t - or u -channel (see Fig. 4.2 for the definition of t ,

¹The cross sections in this paragraph are theoretical predictions at N3LO, if available, or at NNLO otherwise, rather than experimentally measured values. The relative errors indicate the theoretical uncertainty. All values taken from [91] for a Higgs mass of 125 GeV.

²This does not include loop induced gluon fusion contributions to $gg \rightarrow HZ$, which account for an additional cross section of $\sigma_{ggF+Z} = 144 \text{ fb}_{-18.8\%}^{+25.1\%}$.

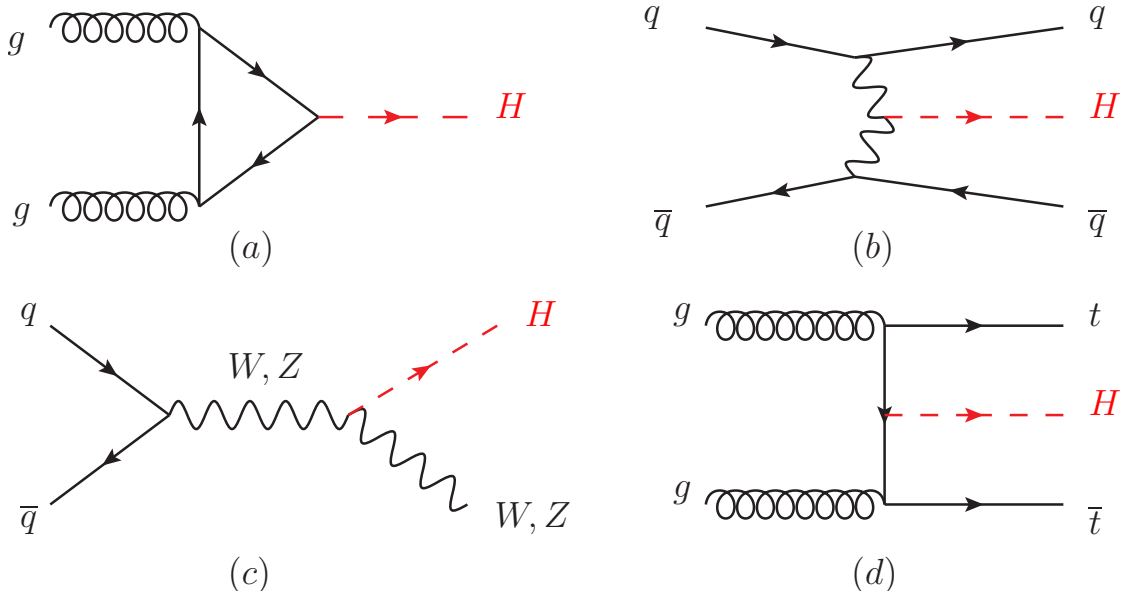


Figure 4.1: The four most important Higgs production modes at the LHC from upper left to lower right: gluon fusion (a), (weak) vector boson fusion (b), Higgsstrahlung (c), and associated production with top quarks (d). Picture taken from [90].

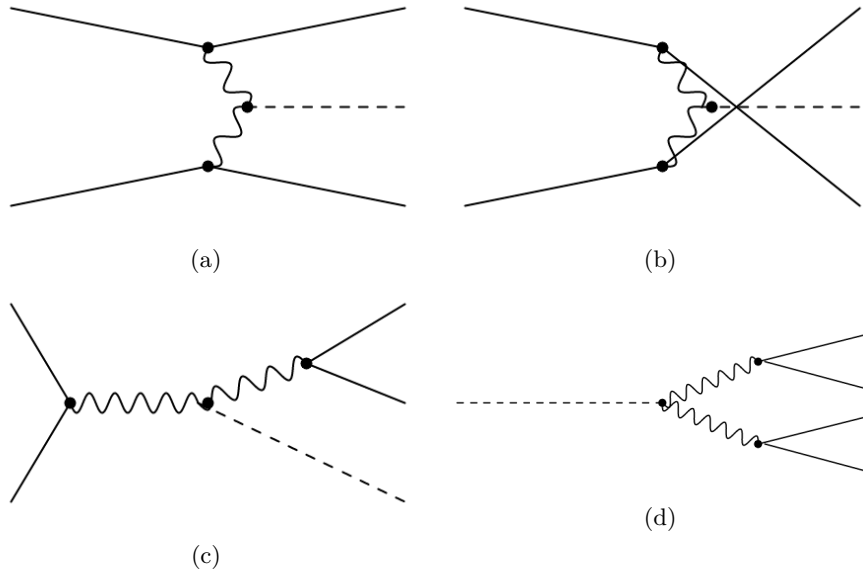


Figure 4.2: Generic Feynman diagrams for the EW production of the Hjj final state in the t - (a), u - (b) and s -channel (c). All diagrams can be obtained from the decay process $H \rightarrow q\bar{q}q\bar{q}$ (d) by crossing two (anti-)quark lines to the initial state and the Higgs line to the finale state in some way. In the stricter sense, the term VBF corresponds to the first two diagrams squared, whereas the third diagrams is known as Higgsstrahlung.

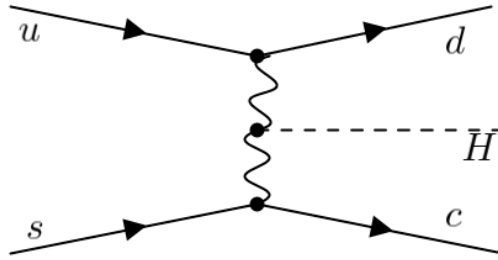


Figure 4.3: The only diagram contributing to the EW process $us \rightarrow dcH$ at $\mathcal{O}(\alpha^3)$.

u and s -type processes). It has to be noted that the term VBF is also used for processes with the same topology, but where an electroweak gauge boson is radiated instead of a Higgs boson. In some publications, also the emission of two gauge bosons is labeled as VBF, which will be referred to by the more unambiguous term *vector boson scattering* (VBS) in this thesis.

However, the VBF process cannot be completely disentangled from the other EW production mode of Higgsstrahlung: As is also visible in Fig. 4.2, the t - and u -channel diagrams for VBF can be obtained from the corresponding decay amplitude $H \rightarrow q\bar{q}q\bar{q}$, but so can an s -channel diagram with the same initial and final states [43, 92, 93]. Commonly, this process is not regarded as part of the VBF class, but rather as a HV production process with subsequent decay of the vector boson into a quark/anti-quark pair. While this distinction may seem a bit arbitrary and even unphysical, it is in fact justified by the features of the two process classes: the amplitudes of the HV process, which already has a comparably small cross section with respect to the VBF process, peak in very different kinematic regions than the t - and u -channel contributions to the VBF process. As we will show, the process is enhanced by the vector boson propagators when the bosons receive only a small momentum transfer. Thus, the VBF process leaves a very distinct experimental signature, where the two final state quarks appear as hadronic jets in the forward region of the detector, called *tagging jets*. The distinct signature is also employed to separate the VBF process from QCD induced background processes with the same final state. This can be seen already from the matrix elements of the process [94, 95, 96]: consider a Born-level process of the type $pp \rightarrow Hjj$ at $\mathcal{O}(\alpha_{em}^3)$, a definition which generally includes both the HV and the VBF process. For simplicity, we will consider a combination of external quark flavours that only allows for W exchange in the VBF channel, e.g. $u(p_1)s(p_2) \rightarrow d(p_3)c(p_4)H(p_5)$ with the p_i denoting the momenta of the particles. The only contributing diagram at $\mathcal{O}(\alpha^3)$ is depicted in Fig. 4.3. The analytic evaluation of the squared matrix element (see [94]) yields

$$|\mathcal{M}_{fi}|^2 \propto \frac{(p_1 \cdot p_2)(p_3 \cdot p_4)}{(q_1^2 - M_W^2)^2(q_2^2 - M_W^2)} \quad , \quad (4.1)$$

where we denote the momenta of the two virtual W bosons with $q_1 = p_1 - p_3$ and $q_2 = p_2 - p_4$, respectively. It has to be noted that the partons are considered to be

massless and the beam axis (i.e. the orientation of \vec{p}_1 and $-\vec{p}_2$) is taken to be the z -axis. In order to maximise the term in Eq. (4.1), we have two options: increasing the numerator or decreasing the denominator. The former simply means that either the partonic center of mass energy $\sqrt{\hat{s}} = \sqrt{(p_1 + p_2)^2} = \sqrt{2 p_1 \cdot p_2}$ or the invariant mass of the tagging jet system $m_{jj} = \sqrt{(p_3 + p_4)^2} = \sqrt{2 p_3 \cdot p_4}$ has to be large. For a closer examination of the latter case, where the denominator is small, let us first rewrite the momentum transfer to the W boson in the partonic centre-of-mass system as follows:

$$q_1^2 = (p_1 - p_3)^2 = -2 p_1 \cdot p_3 = -2 E_1 E_3 (1 - \cos \theta_3) = -\frac{2}{1 + \cos \theta_3} \frac{E_1}{E_3} p_{T,3}^2 < 0 \quad . \quad (4.2)$$

Here, θ_3 denotes the angle between \vec{p}_3 and \vec{p}_1 (which is equivalent to the angle between \vec{p}_3 and the beam axis), and $p_{T,3}$ is the absolute value of the transverse momentum of \vec{p}_3 , given by $p_{T,3} = \sqrt{p_{x,3}^2 + p_{y,3}^2} = E_3 \sin \theta_3$. Since $q_1^2 < 0$, the momentum transfer q_1^2 is bound from above by zero, which means that the expression in Eq. (4.1) will reach its maximum for $q_1^2 \rightarrow 0$. This configuration corresponds to a small scattering angle θ_3 , and we can thus rewrite q_1^2 according to Eq. (4.2) as $q_1^2 \approx -\frac{E_1}{E_3} p_{T,3}^2$, leading to the expression

$$(q_1^2 - M_W^2) \approx -\left(\frac{E_1}{E_3} p_{T,3}^2 + M_W^2\right) \quad (4.3)$$

for the inverse propagator from Eq. (4.1). We therefore expect the process to favour small transverse boson momenta (which are directly related to the tagging jet transverse momenta), and to be significantly suppressed for values of $p_{T,3}$ reaching the scale of the W mass. Also, the scattering angle should be small, which is equivalent to saying that the tagging jets have a high rapidity. Typically, the boson just carries enough energy to produce the Higgs ($\sim m_H/2$ per boson).

In conclusion, we can see that we expect a Higgs boson from VBF production to be accompanied by two tagging jets with large energies and high (pseudo-)rapidities, i.e. being back to back in the forward regions of the detector, and with a high invariant mass of the jet system, m_{jj} . For the s -channel production of the Higgs boson, corresponding to the HV process, however, the invariant mass will likely peak around the masses of the vector bosons and the tagging jets will only have a small separation in rapidity.

Using the same argument, we can also see that interferences between t - and u -channel diagrams can be safely neglected in VBF: they do include the same propagators peaking at small momentum transfer, but the regions in phase space where the peaks appear correspond to very different kinematic configurations (forward or backward scattering). To obtain the t -channel from the u -channel is equivalent to exchanging q_1 by $q_3 = p_1 - p_4$ and q_2 by $q_4 = p_2 - p_3$. Hence, interference between the two channels is suppressed.

This calculation also helps understanding why the VBF process comes with a relatively small rate in comparison to e.g. gluon fusion [96], although this difference can also be attributed to the different sizes of the relevant couplings.

Nevertheless, it is possible to take advantage of the distinct signature of the VBF process by imposing appropriate analysis cuts and to probe it in a phase space region where it dominates over the QCD and HV induced background processes. Usually, one

requires a minimal invariant mass of the tagging jet pair of e.g. $m_{jj} \geq 500 \text{ GeV}$. In most cases, also a minimal separation of the two jets in rapidity with a typical value of $|\Delta y_{jj}| := |y_{j_1} - y_{j_2}| \geq 4.5$ or similar is required (see e.g. [97]). Finally, the two jets are sometimes required to appear in opposite hemispheres of the detector, implying $y_{j_1} \cdot y_{j_2} < 0$. However, it has to be noted that the VBF process – in contrast to VBS processes such as VBS-WW – yields a finite contribution without any cuts on the tagging jets.

When neglecting s -channel contributions and the interference between t - and u -channel, the LO VBF process can be considered as a ‘double deep inelastic scattering’. This approach, known as the VBF approximation, proves to be very helpful when applying NLO-QCD corrections. Since there is no colour exchange between the two quark lines at LO in the VBF approximation, interference with virtual correction diagrams where an additional gluon connects the two quarks is completely suppressed after colour summation and the NLO-QCD corrections can be computed in a structure function approach [22]. Thanks to the form of the real emission corrections to VBF in comparison to other production modes of the same final state, the distinct experimental signature of the process persists in NLO-QCD. Numerical calculations show [94] that the emission of a third jet in the central rapidity region is suppressed similarly to the behaviour of the two tagging jets in LO. As I will show in Chap. 6.2, this *central rapidity gap* becomes even more pronounced when the position of the third jet with respect to the tagging jets is considered. Analogously to LO simulations, where vetoing events with the two tagging jets appearing in the same hemisphere can significantly enhance the signal to background ratio of VBF, the same effect can be achieved for events with three or more jets if only those are accepted where the additional jets are outside of the tagging jet pair in terms of rapidity (*central jet veto*).

If the aforementioned VBF approximation is applied, the process can no longer be identified by the coupling order $\mathcal{O}(\alpha^3)$ and the flavour structure $pp \rightarrow Hjj$ in an unambiguous way. In practice, some automated amplitude generators offer the possibility to exclude intermediate states in the s -channel, thus allowing to restrict the calculation to t - and u -channel (and possibly their interference). If this is not the case, one can define the process by assuming that $SU(3)_C$ exists in two copies: one parton is colour charged only under the first copy, the other parton only under the second one. Thus, no colour exchange between the parton lines is possible. If a diagonal Cabibbo-Kobayashi-Maskawa (CKM) matrix is assumed and at least the first two quark generations are taken to be massless, this can be done by a relatively simple workaround: For the calculation of amplitudes, any flavour combination that would give rise to contributions from more than one kinematic configuration (s , t , and u -channel) is replaced by a flavour combination that is limited to exactly the diagrams that are supposed to be kept. An example for this procedure is the process $u\bar{u} \rightarrow Hu\bar{u}$, which can be part of both VBF (in the t -channel) as well as HV (in the s -channel). Of course, also interference between the diagrams can appear in this case. However, if this flavour combination is replaced by $u\bar{c} \rightarrow Hu\bar{c}$ and the CKM matrix is taken to be diagonal, that process will be restricted to a t -channel diagram which yields exactly the same amplitude as the corresponding t -channel diagram

of the original process. However, it is important that in a calculation for the full hadronic process, the PDF of the \bar{u} is not replaced, since the PDFs generally differ for different flavours. This procedure and its extension to NLO-QCD, where only the possible crossing of quarks in the final state for gluon-initiated processes has to be added, is commonly employed in many numerical tools to simplify the calculation and restrict it to VBF contributions only (see e.g. [48, 25]).

The validity of this VBF approximation given appropriate cuts has been confirmed by numerous studies [98, 99]. A very important common conclusion of these studies is the importance of restricting the phase space to those regions where other contributions are actually negligible. This can also be seen in Sec. 6.2 of this thesis, where I show LO and NLO-QCD results of our process in comparison with existing numerical calculations performed with and without the VBF approximation.

Although the VBF approach has proven very useful at LO and when employing NLO-QCD corrections, it breaks down when NLO-EW corrections are introduced. It is easy to see at the level of Feynman diagrams that virtual corrections with a gauge boson V connecting the quark lines in the t - or the u -channel can indeed interfere with LO diagrams, since charge and colour conservation do not suppress these processes. For this reason, it can make sense to include the whole EW production process of Hjj at $\mathcal{O}(\alpha^3)$ in a calculation, especially if the EW corrections ($\mathcal{O}(\alpha^4)$) are supposed to be part of the calculation as well. For these reasons, and also since the amplitude generator used for this study (presented in Sec. 5.2) does not offer a simple exclusion of specific topologies, we decided to include the full EW contribution to the Hjj final state in our calculation. As a result, the process considered in this thesis is (at LO) fully characterised by the flavour structure $pp \rightarrow Hjj$ and the coupling order. Our choice of focusing on the VBF production mode is motivated by the abundance of studies on VBF, but also by the fact that this part of the phase space also gives rise to less QCD induced background. However, a detailed study of the process in a region where the HV contributions are dominant can be useful in some cases: some theories for physics beyond the Standard Model (BSM) propose a momentum dependent term in the VVH vertex [100, 101, 102], which can be probed at high momentum transfer via the s -channel production of a Higgs boson in association with a vector boson. The HV process is the only tree-level process at LHC energies where the Higgs boson is produced in the s -channel and thus ideally suited for this purpose.

At state-of-the-art colliders such as the LHC, we can expect experimental results with an accuracy at the per cent level for VBF processes [94]. To keep up with this level of precision on the theoretical side, LO calculations are not enough and higher orders of the perturbation series have to be taken into account. The first precision calculations of the VBF process at NLO-QCD have been presented in [22] using the aforementioned structure function approach. Later, more exclusive calculations became available [23, 24], which were then incorporated in public Monte-Carlo generators such as VBFNLO [25, 103, 104] and MCFM [26]. The results showed corrections at a level of several percent to the LO result. To further enhance the precision of these calculations, either higher orders of QCD corrections or EW corrections have to be taken into account. In [28], as a first

step towards full next-to-next-to-leading order (NNLO) QCD predictions, the NLO-QCD corrections to the VBF production of $H + 3j$ have been presented. This is equivalent to the one-loop virtual and double-real corrections to the VBF production of Hjj . Later, NNLO corrections to inclusive VBF production in the structure function approach [29, 30] and a fully differential NNLO-QCD calculation using the so-called ‘projection-to-Born’ technique [31] became available. The latter one was later on extended to include even three-loop corrections in [40, 41]. An alternative approach to NNLO-QCD corrections was presented in [32]. The common finding of these studies was that the effect of higher order QCD corrections on inclusive cross sections is relatively small. It amounts to less than 0.5% for NNLO-QCD and even half this size for the next order in perturbation theory [94]. However, a comparative study in [105] showed that certain kinematic cuts can enhance the influence of the corrections significantly.

Similarly to the VBF process, higher order corrections to the electroweak production of HV have been known for some time. In [34, 35], NNLO-QCD corrections for both the HW and the HZ final state have been calculated and have later been implemented together with NLO-EW corrections in the numerical program `vh@nnlo` [27]. Further corrections of $\mathcal{O}(\alpha_s^2)$ were published in [33]. Later, differential results which also included the decays of the V boson were calculated in [36, 37, 38, 39].

Very naively, by only looking at the size of the relevant coupling constants, one would expect the NLO-EW corrections to be about one order of magnitude smaller than the NLO-QCD corrections. However, while this somehow handwaving approximation might work for QCD-induced processes, it turns out to be fully untrue for processes mediated by the electroweak interaction. The EW radiative corrections to HV production and to the VBF process, which have first been computed in [42, 46] and [43, 44, 45], respectively, account for sizable effects already at the level of inclusive cross sections at typical LHC energies of up to $\sqrt{S} = 14$ TeV. At these collision energies, calculations with the public parton-level Monte Carlo generator `HAWK` [47, 44, 43, 46, 106] show that the NLO-EW corrections are of the order of 5% or larger and only slightly smaller than NLO-QCD corrections within typical VBF cuts. It can be shown that, with increasing collision energies, the EW corrections become even more pronounced. This effect, which will play a role at future collider facilities operating at much higher energies, can be attributed to so-called *Sudakov logarithms*: these are terms of the form $\log \frac{s}{M_{W,Z}^2}$ which arise from gauge bosons emitted by initial or final state particles. This corresponds to the soft and collinear singularities known in theories with massless gauge bosons (see Sec. 3.2.1). Unlike in that case, the soft and collinear singularities between the virtual and real emission corrections do not cancel out for massive gauge bosons (which is why the inclusion of real W and Z emissions is not necessary in the calculation of NLO-EW corrections), and the large logarithms become physically significant [107]. From the form of the Sudakov logarithms, we can easily see that their size will increase with the partonic collision energy \sqrt{s} .

In Sec. 3.3, I explained the importance of parton showers (PS) and non-perturbative effects for the comparison of differential distributions with experimental findings. Accordingly, both the VBF and the HV process have been matched to parton showers at NLO-QCD accuracy. Indeed, VBF was one of the first processes to be implemented in the

framework of the POWHEG BOX (see Sec. 3.3.1), an implementation which has later been ported to the POWHEG BOX V2 and is still being maintained [48]. Later, similar implementations at the NLO-QCD+PS level [49, 50] for the generators MadGraph5_aMC@NLO [108] and HERWIG7 [109] followed. Using these implementations, our work [1] and other recent studies [105, 110] showed that the matching and shower uncertainties for the VBF process cannot be neglected even when the PS is matched to NLO-QCD calculations. We found that a subtle choice of the PS algorithm is necessary to avoid the unphysical population of the rapidity region between the tagging jets with additional radiation by the shower. The reason for this is the global distribution of recoil by some generators, which is unphysical for processes without colour flow between the incoming (outgoing) parton lines, as is the case in the VBF approximation. To reproduce coherence effects in these processes faithfully, dipole-recoil parton showers seem to be a more appropriate choice (also see remarks at the end of section 3.3). One of our key findings was that these implementations agree very well with each other and with fixed order calculations for $H + 3j$, indicating smaller matching uncertainties. The set of available NLO+PS implementations of VBF has been completed by a process in the POWHEG BOX V2, simulating the $H + 3j$ VBF production channel at NLO-QCD+PS [111].

For the HV process, a POWHEG BOX implementation at NLO-QCD+PS has first been published in [51], also including $HV + J$ production. Later, an implementation in the more recent POWHEG BOX RES followed [52], including QCD and EW corrections and leptonic decays of the gauge bosons.

As outlined above, EW corrections to the full electroweak production of the Hjj final state are available also in automated tools for the calculation of integrated and differential cross sections [47, 44, 43, 46, 106], as well as matchings of NLO-QCD calculations for HV and VBF to a PS. However, there is no public NLO-EW calculation of the full process available that can be matched to a (QED) parton shower. In our work, we wish to follow up on that count and close this gap with the NLO-EW+PS generator in the POWHEG BOX RES presented in this thesis.

Chapter 5

Implementation

5.1 The POWHEG-BOX-RES

The POWHEG method described in Sec. 3.3.1 has been implemented into a generic Monte Carlo generator, the POWHEG BOX [53]. This general framework in principle allows interfacing arbitrary NLO-QCD calculations to various SMCs, as long as the generators provide a p_T -ordered shower or the possibility for a vetoed angular-ordered shower. The original program version is nowadays considered obsolete, and two updated versions have been published:¹ POWHEG BOX V2 and POWHEG BOX RES [112]. While the POWHEG BOX V2 is only maintained for backward compatibility and new processes may be implemented in this version, the authors recommend to develop new processes for the POWHEG BOX RES only. Consequently, this version has also been used for the calculations that this thesis is based on, and the main differences with respect to the previous versions will be explained later on in this section.

In general, the POWHEG BOX provides all process-independent ingredients that are needed for an NLO-calculation of (hadronic) cross sections with the POWHEG method. In particular, that is a Monte Carlo integration machinery that implements the VEGAS algorithm [113], an implementation of the FKS subtraction scheme that was discussed in Sec. 3.2.2, and all the parts necessary for generating *events* with the real radiation generated according to the POWHEG method. These events are datasets which correspond to the kinematical configurations of scattering events at a collider facility and contain information about the scattering process and the particles which are involved, e.g. their flavours and momenta. The events can either be associated with a weight corresponding to the contribution of the respective configuration to the total cross section (‘weighted events’), or they are generated with uniform weights, but with a generation probability proportional to this weight. The events, which already contain the hardest emission generated with the POWHEG Sudakov form factor, are written to a file according to the *Les Houches* standard format [114]. This format can be interpreted by most modern PS generators and therefore allows for a simple and universal matching. This feature

¹In this thesis, I will use the name POWHEG BOX for describing general features that are common to every version of the program, not necessarily referring to its original version V1.

makes use of the fact that, in contrast to other methods like MC@NLO, the POWHEG method does not need to be adapted to different SMCs. The POWHEG BOX can also be used to generate arbitrary inclusive and differential cross sections at fixed-order as well, offering either LO or NLO precision. In this case, if NLO corrections are activated, they do not contain a Sudakov form factor, but the real emission is generated according to the standard NLO formula of Eq. (3.15).

While the POWHEG BOX provides the process-independent parts for the calculation, the implementation of specific scattering processes is left to the community of users. For implementing a new process, such as the EW Hjj production process in this case, the user has to provide a list of ingredients which are, according to [53]:

- A complete list of the flavour structures contributing to both the Born and the real emission process.
- A parametrisation of the Born phase space.
- The relevant scattering amplitudes, which are
 - the squared Born amplitudes \mathcal{B} .
 - the colour-correlated Born amplitudes \mathcal{B}_{ij} , and the spin-correlated ones $\mathcal{B}_{\mu\nu}$. These are needed for the FKS subtraction method.
 - the squared real matrix element \mathcal{R} .
 - the finite part of the virtual correction matrix element, which can be calculated in either dimensional regularisation or *dimensional reduction*.
- The Born colour structure of the process in the large N_C limit.
- An analysis routine.

In our case, the list of Born flavour structures is simply given by the set of all structures of the form $q_1q_2 \rightarrow Hq_3q_4$ that are allowed by charge and flavour conservation laws, where the $q_i = \{u, d, c, s, b, \bar{u}, \bar{d}, \bar{c}, \bar{s}, \bar{b}\}$ can be any of the five (anti-) quarks that we assume to be massless. The real emission flavour structures are of the form $qq \rightarrow Hqqq$ or $qg \rightarrow Hqqq$ (plus trivial permutations of the final or the initial states) for the QCD corrections, and of the form $qq \rightarrow Hqq\gamma$ for EW corrections, which means that photon-induced contributions are not taken into account (see the next chapter 6.1 for details). For the Born phase space, which had to be provided by the user in earlier versions of the POWHEG BOX, the POWHEG BOX RES now offers the possibility of using a generic routine that is supposed to generate the phase space based on the flavour structures alone. Some details are discussed at the end of this section, where I focus on the differences of the POWHEG BOX RES with respect to older versions.

The simplest way to set up the basic building blocks of a new process in the POWHEG BOX framework is to use an automated script that comes as part of the POWHEG BOX RES. It invokes an interface to MadGraph [115] that generates all necessary tree-level matrix elements in the form of FORTRAN code. However, any loop amplitudes as well as EW

real emission corrections cannot be generated this way and have to be obtained from other sources. For this purpose, we originally intended to use pre-generated code by the matrix element generator NLOX [116] and developed an interface for its implementation in the POWHEG BOX framework. This generator provides fully renormalised QCD and EW one-loop corrections at the squared-amplitude level in the form of pre-generated code archives for a selection of SM processes. It employs the complex-mass scheme for the evaluation of virtual amplitudes, which the pre-generated code by MadGraph does not support. We therefore decided to obtain all matrix elements from NLOX, in order to achieve a consistent implementation. Thus, we had to implement the correlation matrices for the spin- and colour-correlated matrix elements manually. This reduces to the colour-correlated amplitudes for the EW Hjj process, since the spin-correlated amplitudes vanish. However, during an extensive testing phase (see Sec. 5.3 for details), it turned out that the numerical evaluation of the amplitudes, especially the squared real matrix elements, in the framework of NLOX took an unreasonable amount of computation time for the process at hand. We therefore decided to change to a different amplitude provider, namely RECOLA, which is described in more detail in Sec. 5.2.

The colour structure of the Born events, as needed by the POWHEG BOX, is not unambiguous for our process, since we include both the actual VBF and the HV topologies. Thus, for some of the flavour structures in our list of sub-processes, two or three distinct colour flows are possible, corresponding to the t , u and s channels. This is overcome by a routine which selects one of the possible colour structures with a probability proportional to the squared Born matrix element that corresponds to this colour structure. For this routine, we make use of the trick described in Chap. 4, which is to project a sub-process with ambiguous colour structure onto a corresponding one with the quark generations chosen in a way that only one colour structure contributes.

Finally, the last element missing for a complete process in the framework of the POWHEG BOX is an analysis routine. This consists of some functions to implement cuts on the final state kinematics, and some functions to fill histograms of observables depending on the final state momenta. For example, to define the differential cross section with respect to the transverse momentum of the Higgs boson $p_{T,H}$ in the language of a SMC, one would implement the histogram as a set of products of θ -functions $\theta(p_{T,H} - p_{T,H,i}) \cdot \theta(p_{T,H,i+1} - p_{T,H})$, corresponding to the bins of the histograms.

When a process is fully set up in the POWHEG BOX framework, the program can be used to generate the events in the LHE format that can be fed to a SMC afterwards. This computation is split into four subsequent stages:

1. The grids for the importance sampling of the \tilde{B} function of Eq. (3.27) are set up. This stage can be iterated multiple times, starting with the result of previous iterations, to obtain smoother grids, if desired.
2. At this stage, the NLO cross section is computed, and upper bounding envelopes of the \tilde{B} functions are set up, which are used for the generation of underlying Born configurations. This stage can also be iterated multiple times. If the POWHEG BOX is set up to generate histograms of NLO distributions, this is also performed at this

stage.

3. The upper bounding envelopes for the generation of the hardest radiation, given a Born event, are set up.
4. Events in the Les Houches event (LHE) file format are generated and stored.

These stages can either be carried out in one run, or step by step. The latter choice is used if the runs are supposed to be parallelised, i.e. the numerical effort should be distributed among several processes. The POWHEG BOX can then be run, stage by stage, with an arbitrary number of statistically independent processes. For every stage, the combined output of all runs of the previous stages is used as input to every single process.

The POWHEG BOX RES also allows to change some physical parameters even after the fourth stage of event generation and to then re-weight the events accordingly. This can be especially useful for the variation of the renormalisation and factorisation scales as it is sometimes performed for estimating the theoretical uncertainty.

5.1.1 The Treatment of Resonances

In [112] the POWHEG BOX RES was introduced as an updated version of the POWHEG BOX, which offered ‘the treatment of resonances in NLO calculations matched to a PS’. The reasoning behind this treatment can be summarised as follows: if a process involves decaying resonances, as it is the case in HV production of Hjj , radiation from the decay products of this resonance does not necessarily preserve the virtuality of this resonance. This can affect the calculation in the POWHEG framework in two ways: both for the FKS subtraction scheme, as well as for the modified Sudakov form factor, the framework relies heavily on a mapping from the real emission phase space $PS_{n+1} = PS_{n+1}(PS_n, PS_{rad})$ to the phase space of the underlying Born configurations. Due to momentum reshuffling that becomes necessary when an additional radiation from one of the resonance decay products occurs, the virtuality of the resonant particle can differ by an order of m^2/E [112] between the real emission kinematics and the underlying Born configuration, with E being the energy and m the invariant mass of the merged-parton² system. If the condition $m^2/E \ll \Gamma$ is not satisfied, i.e. the possible deviation in the resonance virtuality is larger than the width of the resonant particle, it cannot be on the resonant peak in both the Born and the real emission configuration at the same time. This may spoil both the FKS subtraction scheme, as well as lead to possibly unphysical values of the \mathcal{R}/\mathcal{B} ratio in the POWHEG Sudakov factor of Eq. (3.25).

For the implementation of the resonance-aware POWHEG method in the POWHEG BOX RES, it is necessary to provide the program with a list of *resonance histories*. These are effectively extensions of the flavour structure arrays that the POWHEG BOX is

²Here, ‘parton’ may refer not only to colour-charged particles, but also to particles with electric charge, if QED or EW radiation is considered. More generally speaking, the reasoning here is valid for any resonance decaying into particles of which at least one is charged under the interaction that is considered in the respective implementation of the POWHEG framework. In the original work cited here, only QCD corrections were considered.

provided with, now including all intermediate resonances and information about which particles stem from the decay of these resonances. For the example of the HV process $u\bar{u} \rightarrow Hc\bar{c}$, this would correspond to information that the process is actually proceeding via the resonance structure $u\bar{u} \rightarrow Z \rightarrow H(Z \rightarrow c\bar{c})$, including two intermediate resonant Z bosons. It is worth noticing that in this formalism, a subprocess that corresponded to only one flavour structure in the old `POWHEG BOX` language can now correspond to several resonance histories. For our process, this is the case whenever the flavour structure allows for t or u channel structures (corresponding to no intermediate resonances being present) as well as for s channel structures, corresponding to two resonant bosons (W^\pm or Z) in the structures. In principle, the `POWHEG BOX RES` was provided with a subroutine in [117] that should be able to generate all possible resonance structures based on the flavour structures and the coupling orders alone. However, we found that this mechanism may fail in its current implementation for some specific NLO-QCD configurations, as well as for NLO-QED corrections where the real emission process differs by powers of the coupling α instead of α_s from the Born configuration. For this reason, we have developed and implemented our own tools for providing the Born and real emission resonance histories.

As I explained above, our process may indeed contain intermediate resonant states which profit from the resonance-aware formalism of the `POWHEG BOX RES`. However, our main motivation to use this new version of the `POWHEG BOX` is another new feature that is closely related to the fact that some (sub-) processes can actually correspond to several different resonance structures. Usually, the kinematic structures of these different resonance histories might also be very distinct. In the case of the EW production of the Hjj state via HV or VBF, I explained in Sec. 4 how we expect the two contributions to peak in very different parts of the phase space. This behaviour can prove to be very difficult for numerical integration. Briefly said, if an adaptive Monte Carlo algorithm with importance sampling is used (e.g. `VEGAS`, the algorithm employed in the `POWHEG BOX` [113]) and the function to be integrated has a complex structure with several maxima, then it is a very involved task to guarantee that the importance sampling is appropriate around each maximum. Consequently, the convergence of the phase space integration in the `POWHEG BOX` might not be as good as desired for processes with several possible resonance structures. The `POWHEG BOX RES` offers a solution to this problem by offering an automated phase space generation with appropriate, separate importance sampling for each resonance structure [118].

5.1.2 EW Corrections and the `POWHEG-BOX-RES`

While the `POWHEG BOX` framework has originally been developed for NLO-QCD calculations only, several implementations of processes involving EW corrections or even combined NLO-EW+QCD corrections became available over time [52, 119, 120, 121, 122, 123]. However, the generalisation of the program for combined NLO-QCD+EW corrections only works when the underlying Born process to any real emission process is defined solely by the flavour structures. In particular, that means that any real emission flavour structure with coupling powers $\mathcal{O}(\alpha^m \alpha_s^n)$ may not correspond to the $\mathcal{O}(\alpha)$ correction

to a $\mathcal{O}(\alpha^{(m-1)}\alpha_s^n)$ Born process and to the $\mathcal{O}(\alpha_s)$ correction to a $\mathcal{O}(\alpha^m\alpha_s^{(n-1)})$ process at the same time. Moreover, even when this condition is fulfilled, the generation of the hardest generation according to the POWHEG formula turns out to be problematic. The reason is the ‘highest-bid’ procedure that is used in the POWHEG BOX RES to determine which kind of radiation is generated by the program. By default, only one emission is stored in the LHE event file and thus passed on to the shower.³ In this part of the event generation, QED and QCD emissions would compete with each other, and, due to the larger coupling, the chance of QCD emission being generated would be much higher. As a result, only a small fraction of the QED emissions would actually be generated with NLO accuracy, while most of the photon radiation would come from the showering process. For this reason, we decided to consider the NLO-QCD and NLO-EW corrections to our process completely separately and leave their simultaneous treatment for future work.

5.1.3 The Matching and Vetoing Procedure

The POWHEG BOX can in principle be matched to any shower that allows for a p_T ordered or a vetoed shower, e.g. HERWIG [124, 109], SHERPA [125] or PYTHIA [56]. For our study, we used the POWHEG BOX RES along with the SMC PYTHIA8 [126]. Due to its origin as a generator for NLO-QCD calculations matched to a PS, the matching and vetoing of calculations in the POWHEG BOX framework in the presence of photon radiation is not completely straightforward. In the case of pure QCD radiation, the POWHEG BOX framework relies on the hardest gluon emission being generated according to the POWHEG formula, so a QCD shower is either started at the p_T of this radiation (if it is ordered in p_T), or harder gluon emissions are vetoed. A QED shower must not be vetoed in the same way if only QCD emission are considered in the POWHEG BOX, since this would correspond to an unphysical limitation of the phase space of photon emissions. The same is of course true for the phase space of gluon emissions by a QCD shower if only photon radiation is considered by the fixed-order calculation.

If PYTHIA is used, the most straightforward matching of a POWHEG BOX calculation is to run the showers for initial and final state with the option `pTmaxMatch = 1` [127]. In this case, the shower is started at the scale written to the variable `scalup` in the LHE file, which is the hardness of the POWHEG BOX emission. However, the definition of the hardness in POWHEG BOX and PYTHIA differ, so small mismatches could occur. For this reason, PYTHIA8 offers a plug-in, the so called `PowHegHooks`, for a fully consistent matching and vetoing of the two programs. If NLO-QCD corrections are selected and matched to a QCD shower in our code, this is the default option used for the matching to PYTHIA8. The QED shower is not affected in this case.

If QED radiation is present at the level of the fixed order calculation (i.e. if EW corrections are computed), we only match it to a QED shower to stick to the completely separate treatment of QCD and EW effects in our calculation. Consequently, the

³The POWHEG BOX RES offers the possibility to store several emission in the LHE file: one from each resonance, and one from the ‘production part’ of the process, which means that such a photon cannot be associated to any resonance. A prescription on how to activate this and other features of the code is given in the appendix A

obstacle of unphysically restricting the QCD shower by vetoing any emission harder than the hardest photon does not exist in our case. However, a correct vetoing of photon emissions in the `PYTHIA8` shower is not part of the program and its plug-ins and had to be implemented by ourselves. To that end, we follow the idea presented in [52] for electroweak corrections to the HV process with leptonic decays: the events from the LHE file are showered by `PYTHIA8`, using the full phase space for QED radiation. We scan the `PYTHIA` event record for photons generated by the `POWHEG BOX RES` and sort them according to their origin from the production part (see footnote 3) of the process or from a resonance. The same is done with the photons produced by `PYTHIA8` after showering. An event is then vetoed if any of the following conditions applies:

- A photon from the production part of the process, i.e. one radiated from any particle that is not a decay product of a resonance, was generated by the shower that is harder than a photon emission from production by the `POWHEG BOX`.
- A photon from a resonance decay is produced by the PS which, *with respect to any of the decay products*, has a larger p_T than a photon from the same decay, generated by the `POWHEG BOX`.
- No photon is present in the LHE file, i.e. the `POWHEG BOX RES` was not able to generate a photon emission harder than the minimal value of p_T for photon radiation⁴ in the program, and a photon harder than this value was generated by the PS.

Any vetoed event is showered again for up to 20 times in our implementation, until it fulfils these criteria.

5.2 RECOLA

The matrix elements required by the `POWHEG BOX` for our calculation were obtained from `RECOLA` [128, 129], a generator for SM matrix elements at tree level and one-loop precision. It generates and numerically computes the scattering amplitudes for arbitrary processes with up to 7 external particles in the SM with the option to obtain NLO-QCD and NLO-EW corrections. Unlike some other matrix-element generators like `MadGraph` [108], it generates the processes on-the-fly in memory instead of generating process source code that can be embedded in a Monte Carlo generator. `RECOLA` is able to provide all the matrix elements for EW Hjj production necessary for the `POWHEG BOX`, i.e. the squared Born and real amplitudes, the colour- and spin correlated Borns and the finite part of the virtual amplitudes. It uses DREG for both UV and IR singularities. Unstable particles are treated according to the complex-mass scheme. The evaluation of tree-level amplitude is not based on a diagrammatic approach, but uses a recursive algorithm [130]. For NLO

⁴This value, determined by the square root of the parameter `rad_ptsqmin_em`, is set to 1 MeV per default. It can be set in the input to every run of the program, see appendix A for details.

calculations, RECOLA includes the tensor integral library COLLIER [131]. The electroweak input parameters can be given either by the α_0 , the α_Z or the G_F scheme.⁵

For the implementation of our process, we used the updated version RECOLA2. While the main difference from this to the previous version concerns the inclusion of BSM models which are of no relevance to our process, it also offers a memory optimisation for crossing related processes. It often happens in the calculations of scattering amplitudes that many of the sub-processes under consideration are related by *crossing symmetries*, meaning that their amplitudes correspond to the same analytical expressions, but with switched momenta. This is also the case in the EW Hjj production process considered here, and RECOLA2 can employ the crossing symmetries to generate related processes only once, thus saving a considerable amount of memory on runtime.

There does not exist a customised interface between POWHEG BOX RES and RECOLA, but the structure of RECOLA allows for a very flexible invocation of the code. For the case at hands this implies that the list of processes in the POWHEG BOX format has to be converted to a format that can be interpreted by the generator to set up all processes in the desired order of the couplings. Moreover, the physics parameters, such as masses, coupling constants and renormalisation scales, have to be transferred to RECOLA. To allow for a dynamical scale, the scales of the POWHEG BOX and RECOLA even have to be synchronised at every phase space point (PSP). We furthermore decided not to use the implementation of the running of α_s in RECOLA, but perform the running in the framework of the POWHEG BOX. This ensures full consistency between every part of the code and furthermore allows to switch between performing a native implementation of the running of the strong coupling in the POWHEG BOX or obtaining the value of α_s at any scale from the PDF set that is being extracted from the LHAPDF library.

5.3 Tests

To prove the validity of our implementation, we performed a whole range of tests against existing codes. These spanned from comparisons of amplitudes at the level of single PSPs to comparisons of cross sections and differential distribution at the level of integrated results.

We first validated the tree level amplitudes of our calculation against several other well established matrix element generators. First and foremost, we compared the Born and real emission QCD amplitudes from NLOX that were used for an earlier version of our implementation (see remarks in Chap. 5) to the MadGraph matrix elements that can be generated by the respective script in the POWHEG BOX RES. Here, we found full agreement within the numerical precision if the complex-mass scheme was not employed in NLOX. To also validate the implementation with complex masses, we compared NLOX to amplitudes based on the ones used in the program VBFNLO [25, 103, 104], again finding full agreement

⁵Since the physical parameters of the EW sector, such as M_W , M_Z , α and G_F are not independent, it is necessary to select a minimal set of input parameters among them. It is useful to chose an input scheme that minimizes universal EW corrections for the process at hand. Usually, the set of input parameters consists of the weak boson masses M_Z and M_W and either $\alpha(0)$, $\alpha(M_Z)$ or G_F .

with and without the complex mass scheme, for Born and QCD real emission amplitudes.

After having decided to use amplitudes from `RECOLA2` throughout the whole program code, we checked our implementation of this generator against the previous, `NLOX` based implementation, finding full agreement for Born, real emission and virtual amplitudes.

To also validate the numerical integration and the implementation of the subtraction scheme in the `POWHEG BOX RES`, we decided to compare our results at the level of integrated and differential cross sections as well. As a reference, we chose the Monte Carlo generator `HAWK` [47, 44, 43, 46, 106], a dedicated program for Hjj production via the HV and VBF channels. This integrator is able to include the NLO-EW and NLO-QCD corrections and offers flexible options to include or exclude several specific contributions. This made it an ideal tool to validate our implementation. Within the numerical accuracy limited by the integration, we found full agreement for calculations at LO and NLO-EW, both within a typical VBF analysis cut set, as well as within loose cuts corresponding to an inclusion of both HV and VBF topologies. The NLO-QCD results only agreed within numerical precision when we manually excluded any sub-channels with initial or final state bottom quarks, since b quark contributions are only implemented at LO precision in `HAWK`.

A detailed check of the full code at NLO+PS accuracy was not possible due to our implementation being the first public program that offers results at NLO-EW+PS accuracy, as well as the only `POWHEG BOX` implementation matching the NLO corrections of the full VBF+acshv process to a PS. However, we used the `POWHEG BOX` implementations of the VBF process at NLO-QCD+PS accuracy [48] and of the HV process with leptonically decaying vector bosons at NLO-EW+PS accuracy [52] to get an estimate of the shower effects that were to be expected. We found that the corrections on differential distributions modelled by our code behaved reasonably in size and form.

Chapter 6

Phenomenology

We used the `POWHEG BOX RES` process code that we developed and that has been described extensively in the previous chapter for a first experimental study that has been published in [2]. In this chapter, I will introduce the setup of this study before presenting its results in an extended form, supplemented by a few results from one of our earlier studies [1].

6.1 Setup

For the phenomenological results that will be presented in the next Sec. 6.2 of this thesis, and in the corresponding publication [2], we run our code to generate events in a setup that mimics the conditions at the LHC. In particular, that means we consider pp collisions at a hadronic centre-of-mass energy $\sqrt{S} = 13$ TeV, which was the value that was reached during the LHC run II between 2015 and 2018. We use the `NNPDF3.1luxQED-NLO` set [132] of PDFs as implemented in the `LHAPDF` package [133], where it has the identifier 324900. This set corresponds to a value of the strong coupling constant $\alpha_s(M_Z) = 0.118$. The renormalisation and factorisation scale are set dynamically at every PSP based on the kinematics of the underlying Born event. More precisely, we use the arithmetic mean of the transverse momenta of the two outgoing partons i_1, i_2 :

$$\mu_R = \mu_F = \frac{p_{T,i_1} + p_{T,i_2}}{2} .$$

For Born events, the partons i_1, i_2 can be identified with the two tagging jets. This choice of scale is relatively close to the actual momentum transfer from the partons to the vectors bosons and at the same time, it is relatively robust to one of the jets becoming soft. This is different, for example, for another common scale choice, the geometric mean of the transverse momenta. Such a scale should only be employed when events with one of the jets becoming soft – which corresponds to this scale approaching zero – can be vetoed already at the generation level, which is not the case in our `POWHEG BOX` implementation. Lastly, our scale choice only depends on the underlying Born kinematics. While this may seem not to be ideal for events with real emission kinematics, it avoids a mismatch of the scales and, subsequently, the value of α_s between a real emission event and its

underlying event. Since our scale changes dynamically at every PSP, we can perform the running of α_s by using the corresponding value at this scale. For the calculations presented in this thesis, these values are taken directly from the PDF set via the interface of the `POWHEG BOX` to `LHAPDF`.

Although it is a very common practice to obtain an estimate of the theoretical uncertainty associated with an NLO-QCD calculation by varying the factorisation and renormalisation scales by constant factors ξ , commonly with $\xi \in \{0.5, 1, 2\}$, we decided against this procedure for the current study. This can be justified by two reasons: first and foremost, we consider the main novelty of our code the inclusion of EW corrections and their matching to a PS. For NLO-EW calculations, the scale dependence is usually not considered. Secondly, we showed in our previous study [1] that even for the NLO-QCD+PS calculations of the VBF process, the dependence on the scales is much smaller than the dependence on the shower matching procedure that is being used. For this reason, only considering the uncertainty associated with the choice of scales would correspond to a significant underestimation of the theoretical uncertainty and would imply a level of precision that the calculation cannot actually guarantee.

A decay of the Higgs boson is not implemented within our code, and the final-state Higgs boson is assumed to be on-shell. We leave an implementation of the Higgs boson decays, for example through the means of a multi-purpose program like `PYTHIA8`, to future work. Consequently, distributions that depend on the Higgs kinematics do not need any reconstruction of its momentum. Jets, on the other side, are reconstructed according to the anti- k_T algorithm (see Sec. 3.2.2) as implemented in the `FastJet` package [134, 135] with the radius parameter set to $R = 0.4$. The algorithm is fed any colour-charged particles, which includes quarks, gluons, and possibly di-quarks in the beam remnant, if present. The remnant is only present if the `PYTHIA8` shower is used, and its exact representation as a system of (anti-)quarks and di-quarks is subject to the implementation of the PS. Since we do not include the effects of hadronisation, hadrons cannot appear and do not play a role in the jet algorithm. I would like to stress that photons do not enter the jet algorithm in the same way colour charged partons do. We also do not show any distributions of real photons, but they nevertheless influence the distributions in two ways: first, the recoil of the emissions is naturally mirrored in the momenta of the other particles. Second, we use a scheme that is known as *dressing* of the partonic jets. This simply means that, after jet reconstruction, any photon that is separated from a jet by less than $\Delta R_{\gamma j} = 0.1$ in the rapidity-azimuthal angle plane, gets recombined with this jet to a dressed jet.

For the EW parameters, we use the G_μ input scheme with the Fermi constant set to $G_\mu = 1.16637 \times 10^{-5} \text{ GeV}^{-2}$. Throughout the whole calculation, `RECOLA2` uses the complex mass scheme [129]. For the masses and widths of the massive vector bosons and the Higgs boson as well as the top quark mass we use pole masses m_P and widths Γ_P , which are related to the on-shell quantities m_{OS} and Γ_{OS} via

$$m_P = \frac{m_{OS}}{\sqrt{1 + \Gamma_{OS}^2/m_{OS}^2}}, \quad \Gamma_P = \frac{\Gamma_{OS}}{\sqrt{1 + \Gamma_{OS}^2/m_{OS}^2}} \quad .$$

The values used in our calculation for the masses of the vector bosons W and Z , the Higgs boson H and the top quark t correspond to the latest values of the on-shell quantities of the particle data group (PDG) [61], which are:

$$\begin{aligned} m_W &= 80.379 \text{ GeV}, & \Gamma_W &= 2.085 \text{ GeV}, \\ m_Z &= 91.1876 \text{ GeV}, & \Gamma_Z &= 2.4952 \text{ GeV}, \\ m_H &= 125.25 \text{ GeV}, & \Gamma_H &= 3.2 \times 10^{-3} \text{ GeV}, \\ m_t &= 172.76 \text{ GeV}, & \Gamma_t &= 1.42 \text{ GeV} \quad . \end{aligned}$$

We assume any quark apart from the top quark t and their anti-quarks to be massless. Contributions with external top quarks are disregarded, whereas the top quark can enter through massive fermion loops in the virtual EW corrections. The CKM matrix is regarded to be diagonal, which reduces the number of sub-channels to be considered due to the absence of a mixing between the quark generations. We also neglect contributions from initial state photons, which were found to yield a correction of roughly one percent to the EW production of the Hjj final state and can therefore be considered subleading w.r.t. quark-initiated channels [44].

For the PS, we use the version 8.240 of the PYTHIA8 SMC. The shower is always tuned to the Monash 2013 tune [136]. Per default, we use the global recoil scheme of PYTHIA8. Only if explicitly stated otherwise, we use the more recent dipole recoil scheme for the space-like initial state shower instead. The simulation of underlying event, hadronisation and multi-parton interaction in PYTHIA8 is switched off throughout. As explained in the previous chapter, we consider NLO-EW and NLO-QCD corrections separately, and we only match NLO-QCD calculations to a pure QCD shower and NLO-EW calculations to a pure QED shower. Consequently, we denote as NLO-QCD+PS or NLO-EW+PS a matching of the fixed-order calculations with the respective PS.

For our numerical studies, we consider three experimental scenarios with different cuts. In the first setup, which I will call the *HV setup*, we apply cuts to enhance the Higgsstrahlung contributions, i.e. the s -channel contributions with possibly resonant vector bosons. The second cut selection, dubbed *VBF setup*, is aimed at enhancing the (t - and u -channel) VBF contributions, whereas in the third, *inclusive setup*, only very basic selection cuts are applied. With this cut set, we require the presence of at least two jets, fulfilling the following minimal requirements on transverse momentum and rapidity:

$$p_{T,j} > 25 \text{ GeV}, \quad |y_j| < 4.5 \quad . \quad (6.1)$$

The two hardest jets which fulfil these requirements are identified with the “tagging jets”. They have to satisfy an additional cut on their invariant mass of

$$m_{jj} > 60 \text{ GeV} \quad . \quad (6.2)$$

In the VBF cut set, we impose the same cuts on the jets, i.e.

$$p_{T,j} > 25 \text{ GeV}, \quad |y_j| < 4.5 \quad , \quad (6.3)$$

but the two hardest jets (again dubbed the tagging jets) have to fulfil a more restrictive cut on the invariant mass,

$$m_{jj} > 600 \text{ GeV} \quad , \quad (6.4)$$

and have to be well separated in rapidity,

$$\Delta y_{jj} > 4.5 \quad . \quad (6.5)$$

Furthermore, we require the two tagging jets to be located in opposite hemispheres of the detector, which corresponds to

$$y_{j_1} \cdot y_{j_2} < 0 \quad . \quad (6.6)$$

For the HV cut set, the criteria on the jets are slightly stricter, namely

$$p_{T,j} > 25 \text{ GeV}, \quad |y_j| < 2.5 \quad . \quad (6.7)$$

In this setup, the system of tagging jets has to exhibit an invariant mass in a window around the weak boson masses:

$$60 \text{ GeV} < m_{jj} < 140 \text{ GeV} \quad . \quad (6.8)$$

As can be easily seen, the inclusive setup corresponds to the union of the HV set and the VBF set, plus the part of the phase space corresponding to an invariant dijet mass $140 \leq m_{jj} \leq 600 \text{ GeV}$.

In any cut set, we require at least two jets fulfilling the requirements on the tagging jets of the respective set to be present. If additional jets are present, this has no consequence on the event selection. However, for distributions related to a third jet or to even higher jet multiplicity n , we only consider those jets which pass the following cuts on transverse momentum and rapidity:

$$p_{T,j_n} > 25 \text{ GeV}, \quad |y_{j_n}| < 4.5 \quad . \quad (6.9)$$

The only exceptions to these cuts are distributions of the transverse momentum p_{T,j_3} of the third jet, where we decided to include jets when

$$p_{T,j_n} > 0.1 \text{ GeV}, \quad |y_{j_n}| < 4.5 \quad . \quad (6.10)$$

In order to illustrate some effects that were not in the focus of our current study [2], I will also present a few results from a previous study which we already presented in [1]. That work studied the effects of QCD showers on NLO-QCD calculations of the VBF process, with an emphasis on the uncertainties associated with the PS algorithms and their matching to the fixed order calculations. There, the majority of the generators included in the study only covered the VBF contributions to the Hjj final state, and therefore, an appropriate cut set had to be used. That setup corresponds to the VBF setup used for the study in this thesis, but the choice of the scales μ_R and μ_F , as well as the PDFs used differ from our current choice. I will therefore explicitly mark whenever results from this work are presented. For a detailed description of the parameters used, I refer the interested reader to the corresponding publication [1].

Table 6.1: Integrated cross section at LO, NLO-QCD, and NLO-QCD+PS level within the different cut sets, including statistical errors.

Cut set	LO	NLO-QCD	NLO-QCD+PS
Inclusive cuts	3.250(2) pb	3.272(2) pb	3.046(2) pb
VBF cuts	0.9543(6) pb	0.8618(13) pb	0.7890(12) pb
HV cuts	0.6110(14) pb	0.7914(16) pb	0.7581(12) pb

6.2 Numerical Results

Let me begin this section with a presentation of some distributions at NLO-QCD and NLO-QCD+PS level, as compared to the Born approximation. In good accordance with expectations from the literature [43], we find that the NLO-QCD corrections enhance the inclusive LO cross section within the inclusive cut set of Eqs. (6.1)–(6.2) only mildly, accounting for an enhancement of less than 1% (see Tab. 6.1). As expected for very inclusive cuts, the influence of the PS is also relatively mild and accounts for a reduction of the QCD corrected cross section by 7%. The fact that the shower effects are comparably small for inclusive cuts follows almost trivially from the unitarity of the shower: we could expect the integrated cross section of the full process without *any* selection cuts to be unchanged by the PS. The only influence on integrated cross sections can occur when the shower changes the kinematics of an event in such a way that its acceptance by the analysis is changed.

An interesting distribution within the inclusive cut set is that of the invariant mass of the tagging jet pair, m_{jj} , as depicted in Fig. 6.1. Here, we compare the LO predictions to the calculations at NLO-QCD and at NLO-QCD+PS accuracy. At LO, we can relatively clearly separate this distribution into two different parts: a very prominent peak around the masses of the weak gauge bosons at approximately 70 – 100 GeV, which corresponds to the phase space region dominated by *HV* contributions, and the tail of the distribution with a bulk at ~ 300 GeV. As elaborated in Chap. 4, we expect that this latter part is dominated by VBF contributions, especially at larger values of $m_{jj} > 500$ GeV. It can be seen that the NLO-QCD corrections behave very differently between these two parts of the invariant-mass distribution of the tagging jets. While the VBF-dominated tail of the distribution is reduced w.r.t. the Born approximation, the NLO corrections lead to a very strong increase of the peak just below 100 GeV that corresponds to the invariant mass of the vector bosons W and Z . Finally, the region in between this peak and the aforementioned bulk at ca. ~ 300 GeV is smeared out by the NLO-QCD corrections.

In this distribution of the invariant jet mass m_{jj} , we can also see that the influence of the PS on the NLO results is relatively mild. This behaviour is to be expected for distributions of the tagging jets, as the main influence of the shower on them happens indirectly, i.e. via the recoil of the additional radiation or through the momentum reshuffling that is necessarily performed when employing a SMC (see Sec. 3.3). While theoretically, the partonic emissions by the PS are also a source of jet activity, this radiation is soft or collinear by construction and therefore very unlikely to account for

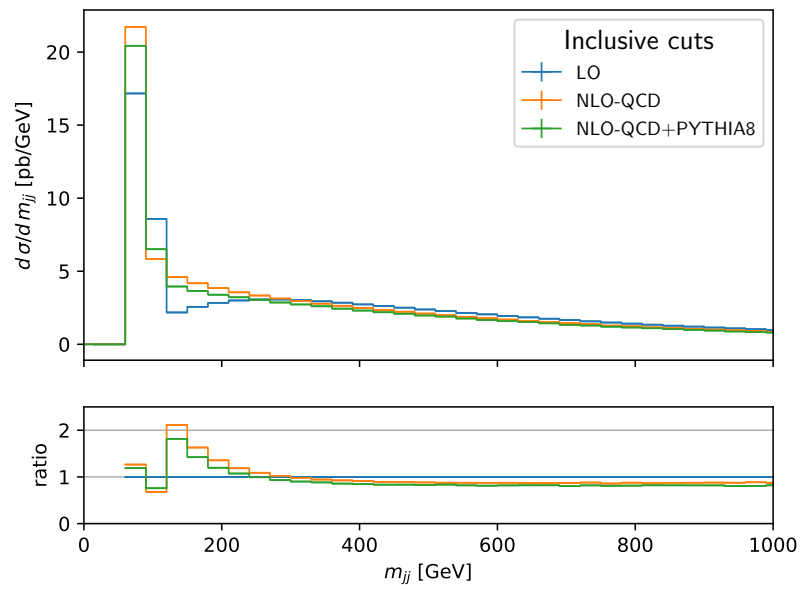


Figure 6.1: Invariant-mass distribution of the tagging jet system at LO (blue), NLO-QCD (orange) and NLO-QCD+PS (green) within the inclusive cuts of Eqs. (6.1)–(6.2). The ratio with respect to the LO results is shown in the lower panel. Error bars indicate statistical errors.

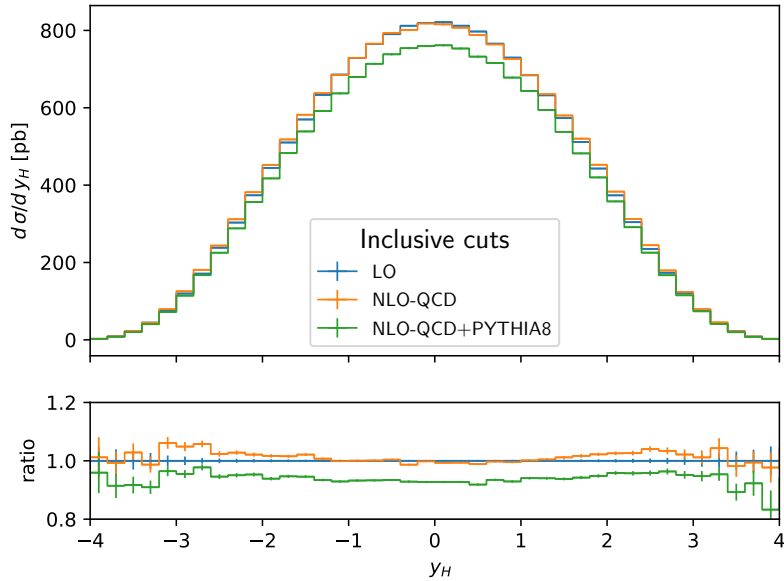


Figure 6.2: Rapidity distribution of the Higgs boson at LO (blue), NLO-QCD (orange) and NLO-QCD+PS (green) within the inclusive cuts of Eqs. (6.1)–(6.2). The ratio with respect to the LO results is shown in the lower panel. Error bars indicate statistical errors.

one of the two hardest jets entering the m_{jj} distribution.

An interesting behaviour can be seen for the distribution of the rapidity of the Higgs boson, y_H , in Fig. 6.2. As expected, this distribution is relatively insensitive to NLO-QCD corrections. Nevertheless, it seems that this distribution is significantly influenced by the PS. However, the lower plot in the same figure reveals that the ratio between the NLO-QCD distribution and the distribution with PS is more or less constant and corresponds to the reduction of the total cross section by about 7% within the inclusive cut set (see Tab. 6.1).

In Fig 6.3, I show the differential cross section w.r.t. number of jets n_j . This distribution shows how the NLO-QCD corrections lead to a reduction of the cross section with only the tagging jets present, while they introduce events with real emission radiation, corresponding to $n_j = 3$. Again, we can see that the influence of the PS on events with no additional radiation is negligible, while the shower leads to a further redistribution of events with one real emission to even higher jet multiplicities, $n_j \geq 4$.

I will now turn to the discussion of the results within the VBF setup of Eqs. (6.3)–(6.6). Within this setup, the NLO-QCD corrections have a more pronounced influence on the integrated cross section, leading to a reduction of almost 10%. This is again in accordance with results from earlier studies [43] and could also be expected from the results shown in Fig. 6.1. There we already saw that the region of high invariant dijet mass m_{jj} , which is predominantly filled by VBF events, experiences a relatively uniform reduction

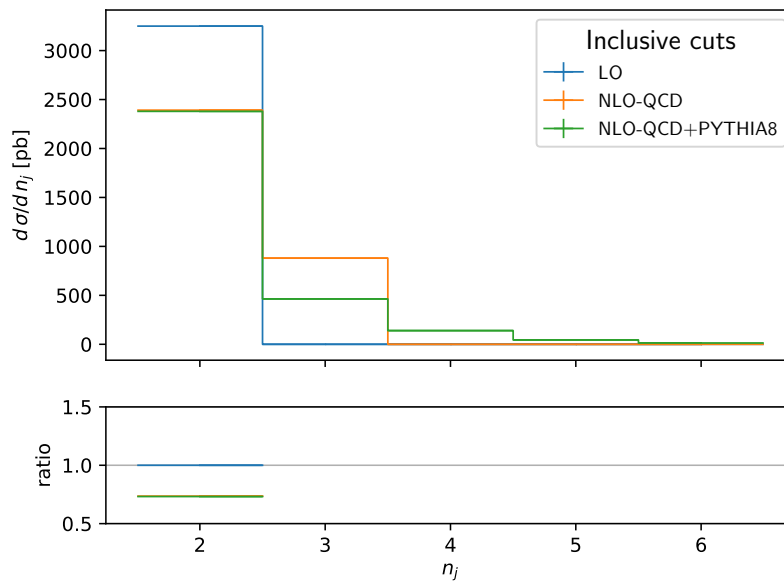


Figure 6.3: Cross section w.r.t. the number of jets at NLO-QCD (blue) and NLO-QCD+PS (orange) within the inclusive cuts of Eqs. (6.1)–(6.2). The ratio with respect to the LO results is shown in the lower panel. Error bars indicate statistical errors.

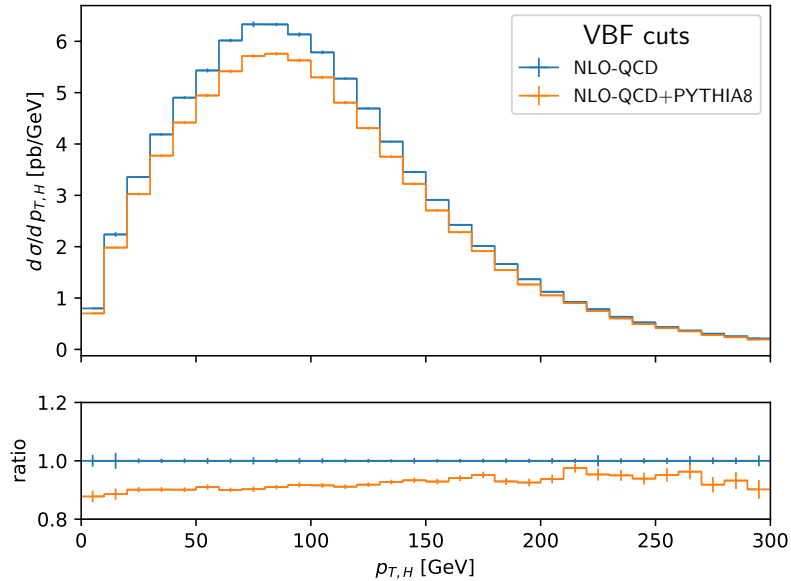


Figure 6.4: Transverse momentum distribution of the Higgs boson at NLO-QCD (blue) and NLO-QCD+PS (orange) within the VBF cuts of Eqs. (6.3)–(6.6). The ratio with respect to the NLO results is shown in the lower panel. Error bars indicate statistical errors.

consistent with the reduction of the integrated cross section within the VBF cut set. The PS reduces the cross section within this cut set even further, accounting for an additional impact of ca. -8% . Again, the shower unitarity dictates that this reduction of the cross section may only stem from a redistribution of events which pass the VBF cuts on the NLO-QCD level, but get rejected after the PS is applied.

As in the inclusive cut set, the influence of the shower on distributions of the Higgs boson and the two tagging jets within the VBF cuts is relatively mild, as shown in Fig. 6.4, where the transverse momentum $p_{T,H}$ of the Higgs boson is depicted. Here, we can see that both the NLO-QCD corrections and the shower act uniformly over the full range of the distribution. In a similar manner, the influence of the QCD corrections on the transverse momentum of the hardest jet, p_{T,j_1} , is only moderate, as can be seen in Fig. 6.5.

However, turning to distributions of the third hardest jet in the same setup, we can see much more pronounced effects of the NLO-QCD corrections and the shower. This can be seen in Fig. 6.6, where we plot the differential cross section w.r.t. the transverse momentum of the third hardest jet p_{T,j_3} . At this point, I remind the reader that additional radiation beyond the two tagging jets has to fulfil only a minimal cut on the transverse momentum p_{T,j_3} for the event to be considered in this distribution (see Eq. (6.10)). The behaviour at very low values of the transverse momentum explains why we decided to include this soft radiation as well: here, the cross section at NLO+PS accuracy drops

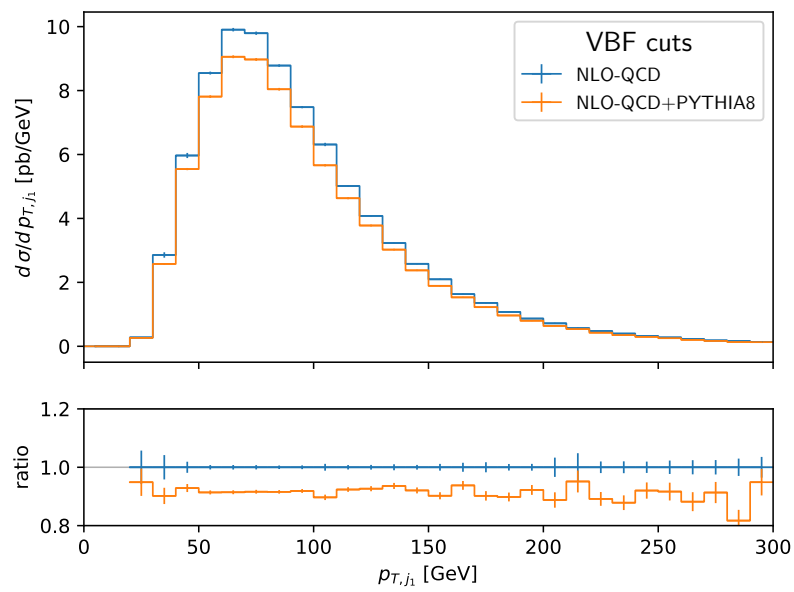


Figure 6.5: Transverse momentum distribution of the hardest jet at NLO-QCD (blue) and NLO-QCD+PS (orange) within the VBF cuts of Eqs. (6.3)–(6.6). The ratio with respect to the NLO results is shown in the lower panel. Error bars indicate statistical errors.

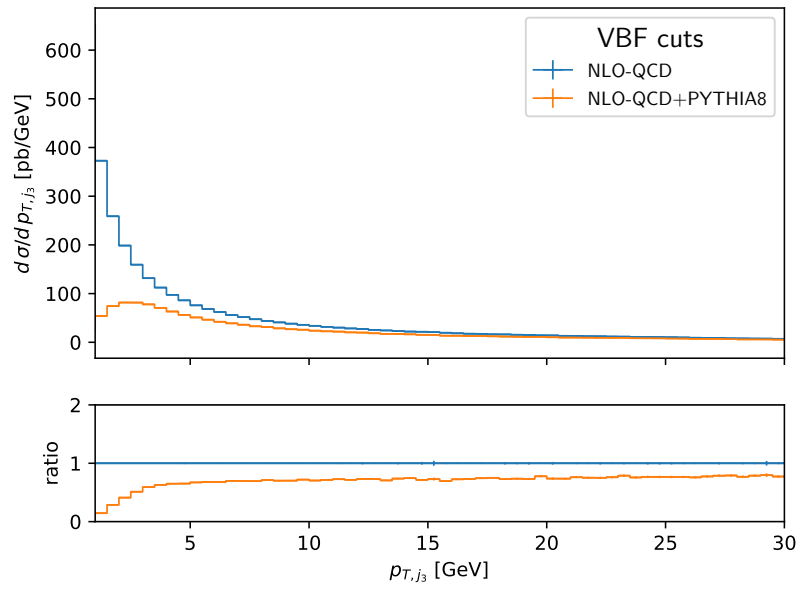


Figure 6.6: Transverse momentum distribution of the third hardest jet at NLO-QCD (blue) and NLO-QCD+PS (orange) within the VBF cuts of Eqs. (6.3)–(6.6). The ratio with respect to the NLO results is shown in the lower panel. Error bars indicate statistical errors.

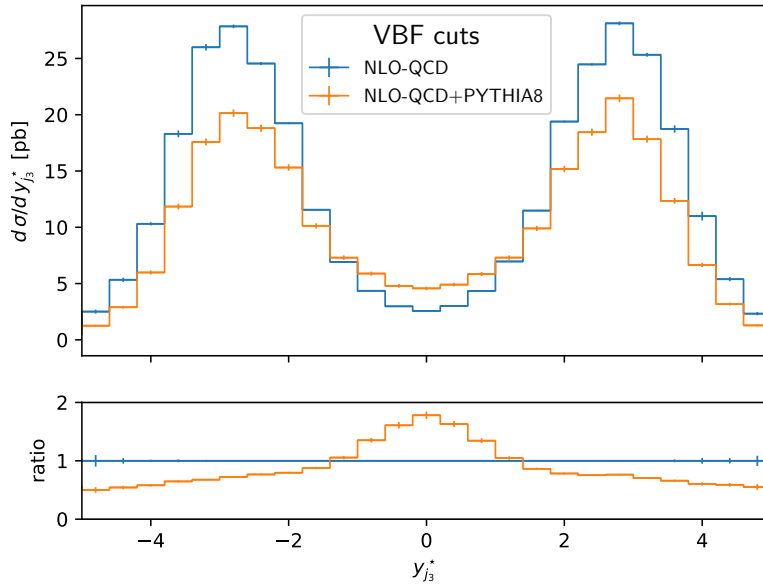


Figure 6.7: $y_{j_3}^*$ distribution of the third jet at NLO-QCD (blue) and NLO-QCD+PS (orange) within the VBF cuts of Eqs. (6.3)–(6.6). The ratio with respect to the NLO results is shown in the lower panel. Error bars indicate statistical errors.

steeply with respect to the distribution at NLO-QCD accuracy which shows the typical divergent behaviour for $p_{T,j_3} \rightarrow 0$. We recall that the hardest radiation as generated by the POWHEG framework already includes a (modified) Sudakov factor, leading to this reduction of very soft radiation. For higher values of p_{T,j_3} , the influence of the PS mainly results in a flat reduction.

In Fig. 6.7, the distribution of $y_{j_3}^*$ is plotted. This observable encodes the relative rapidity position of the third jet with respect to the arithmetic average of the rapidities of the two tagging jets and is defined as

$$y_{j_3}^* = y_{j_3} - \frac{y_{j_1} + y_{j_2}}{2} \quad .$$

Consequently, a value of $y_{j_3}^*$ close to zero correspond to the third jet located right in the centre of the tagging jet system, while high absolute values correspond to radiation outside of the tagging jet system. In this plot, we can see a very pronounced enhancement of additional radiation in the central region between the two tagging jets by the shower. This corresponds to the effect that was discussed in Sec. 3.3. As explained there, the description of the third jet in the central rapidity region by a shower with a global recoil scheme is not entirely suitable for the VBF process.

To illustrate this, in Fig. 6.8 I show two plots taken from our earlier paper [1], where we compared the rapidity distribution of the third jet between different shower recoil

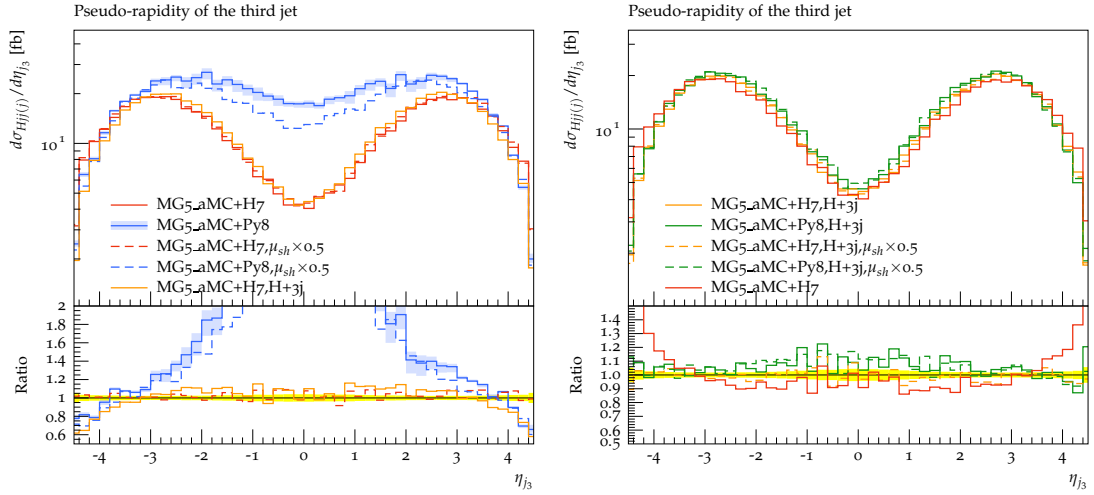


Figure 6.8: Left plot: Rapidity distribution of the third jet at NLO-QCD+PS, generated by MadGraph5_aMC@NLO and matched to showers by HERWIG7 (red lines) and PYTHIA8 (blue lines, with global recoil). The results of a $H + 3J$ calculation are depicted in orange.

Right plot: predictions for the $H + 3j$ VBF process matched to HERWIG7 (orange) and PYTHIA8 (green). The red line again shows the result for the Hjj VBF process matched two HERWIG and is therefore identical to the solid red line in the left plot.

The dashed lines are the results of a variation of a characteristic scale of the shower matching, whereas the error band for the solid blue line shows the theoretical uncertainty connected to the variation of μ_F and μ_R . See the original publication [1] for details.

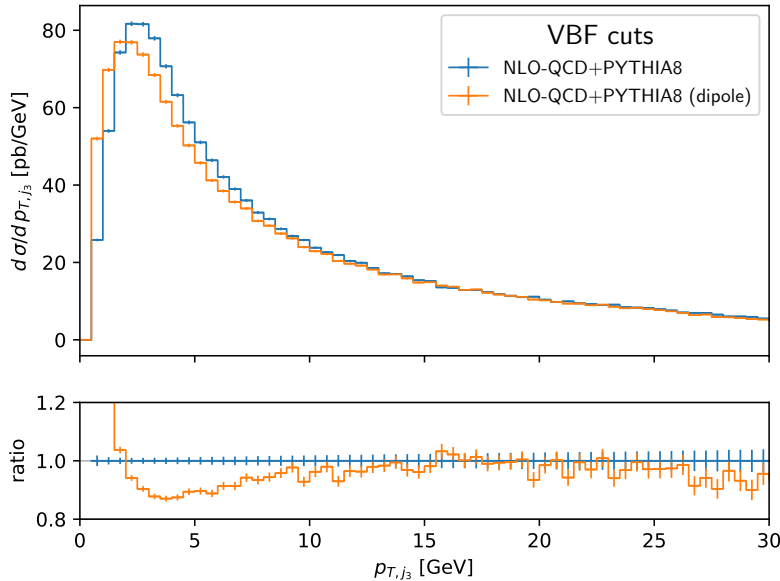


Figure 6.9: Transverse-momentum distribution of the third-hardest jet at NLO-QCD+PS accuracy with the default global recoil scheme (blue) and the dipole recoil scheme (orange) of PYTHIA8 within the VBF cuts of Eqs. (6.3)–(6.6). The ratio of the dipole to the default shower result is shown in the lower panel. Error bars indicate statistical errors.

schemes matched to a NLO-QCD calculation by `MadGraph5_aMC@NLO` [108, 137]. For that study, we were able to compare our results to an implementation of the VBF production of $H + 3J$ as well, i.e. to an implementation the same process with an additional jet in the final state. The left plot clearly shows that the parton shower by `HERWIG7` [138], using a dipole recoil, agrees very well between the Hjj and the $H + 3J$ implementation, whereas the PYTHIA8 program with the global recoil matched to the Hjj process predicts much more radiation in the central region. The right plot confirms that, if the global recoil shower is being matched to the $H + 3J$ process, it also matches the predictions obtained with a dipole recoil scheme.

At this point, I want to remind the reader that our calculation does not rely on the VBF approximation, but that it includes the full EW production of the Hjj final state. For this reason, the assumption that there is no colour flow between the quark lines in the initial state does not hold any more. Consequently, a global distribution of the shower recoils would not be unphysical per se. However, within the VBF cut set, we expect a strong domination of VBF events over the HV production, and the enhancement of the radiation in the central rapidity region might still be due to this very effect.

To verify this behaviour with our implementation, we matched the NLO-QCD calculations to the dipole recoil shower of PYTHIA8 as well. Its influence on distributions of the third hardest jet in the VBF setup is shown in Fig. 6.9–6.10, where we compare

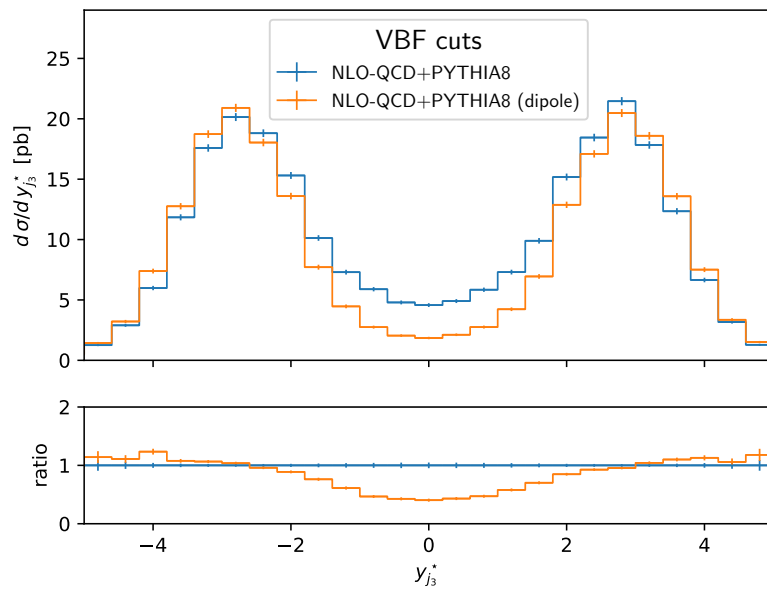


Figure 6.10: $y_{j_3}^*$ variable of the third-hardest jet at NLO-QCD+PS accuracy with the default global recoil scheme (blue) and the dipole recoil scheme (orange) of `PYTHIA8` within the VBF cuts of Eqs. (6.3)–(6.6) and the extra requirements of Eq. (6.9) on the third jet. The ratio of the dipole to the default shower result is shown in the lower panel. Error bars indicate statistical errors.

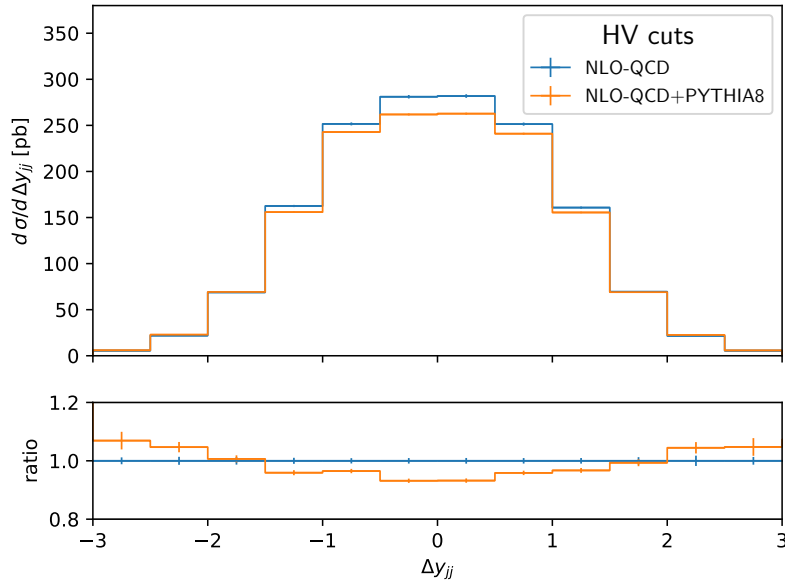


Figure 6.11: Rapidity difference of the two tagging jets at NLO-QCD (blue) and NLO-QCD+PS (orange) within the HV cuts of Eqs. (6.7)–(6.8). The ratio with respect to the NLO results is shown in the lower panel. Error bars indicate statistical errors.

the two matching schemes. The first figure mapping the transverse momentum p_{T,j_3} of the third jet shows only very little differences between the two schemes. Both seem to reproduce the same Sudakov behaviour for small transverse momenta and agree within the numerical uncertainty especially in the tail of the distribution. However, a much more pronounced difference between dipole and global recoil can be seen, as expected, for the relative rapidity $y_{j_3}^*$ of the third jet, where we can see that the former suppresses the unphysical radiation in the central region significantly.

I now discuss the results at NLO-QCD and at NLO-QCD+PS precision in the HV cut set of Eqs. (6.7)–(6.8). In this setup, the NLO-QCD corrections enhance the cross section by about 29%. This is partly compensated by the PS, which reduces the NLO cross section by ca. 4% (see Tab. 6.1). Interestingly, a very different behaviour of the jets can be seen in this setup as compared to the VBF setup, as depicted in Fig. 6.11. Here, I show again the rapidity separation of the tagging jets Δy_{jj} . In contrast to the VBF setup of the previous paragraphs, the HV setup imposes no direct cuts on this observable and its whole range, including the central region corresponding to the two jets being very close in rapidity, can be filled. Theoretically, the cuts on $|y_j| < 2.5$ should allow for this distribution to be filled just up to $\Delta y_{jj} = 5$, but the distribution approaches zero at even lower values. This is a very typical behaviour for the HV production of the Hjj final state. In the present case, the VBF contributions are suppressed by the upper cut on the invariant jet mass m_{jj} of the HV cut set and the distribution is therefore dominated

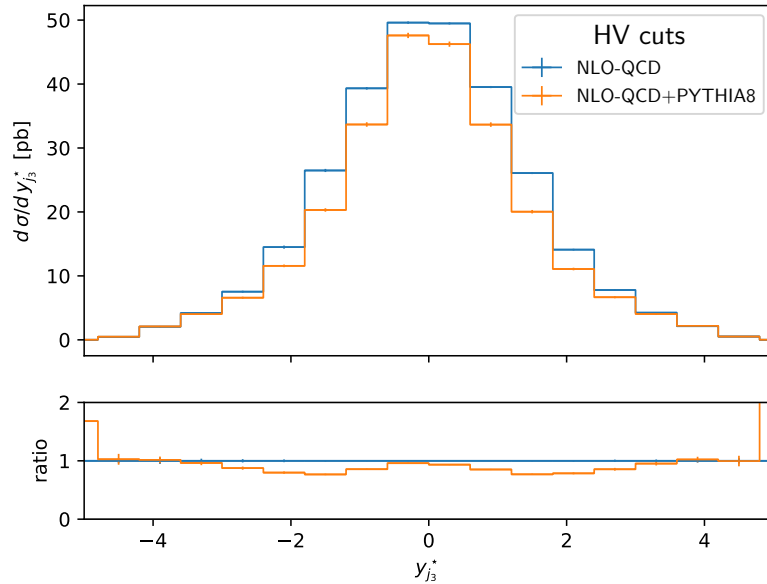


Figure 6.12: $y_{j_3}^*$ variable of the third jet at NLO-QCD (blue) and NLO-QCD+PS (orange) within the HV cuts of Eqs. (6.7)–(6.8). The ratio with respect to the NLO results is shown in the lower panel. Error bars indicate statistical errors.

by s -channel contributions. In the past, both m_{jj} and Δy_{jj} have proven to be excellent discriminators between VBF and HV events individually, and it therefore comes as no surprise that they are correlated very strongly.

The plot in Fig. 6.12 shows an even more striking difference compared to the VBF setup. Here, the relative rapidity $y_{j_3}^*$ of the third jet is plotted again, revealing a very different radiation pattern. Rather than being close to one of the tagging jets, the third jet is now located preferably at the centre of the two jet system. For this very reason, some experimental analyses for the VBF process employ a *central jet veto*, which means that they reject any events with additional radiation between the two tagging jets to improve the ratio of the signal process (VBF) to the background induced by the HV process or other production modes, for instance QCD-initiated processes.

We recall that within the VBF setup, this distribution, which seems to experience only a relatively uniform reduction by the shower in the HV setup, was affected most by the choice of a particular recoil scheme for the PS. For this reason, I show the same distribution with the NLO-QCD calculation matched to both recoil schemes of `PYTHIA8` in Fig. 6.13. It turns out that the dipole shower gives rise to a relatively flat reduction within the HV cuts, but that we cannot observe strong shape differences as they were to be seen for the VBF cuts. Since the VBF-induced production is strongly suppressed by the HV cuts, we cannot simply reject the results with the global recoil shower as unphysical any more. Instead, our code might be used for a more detailed assessment

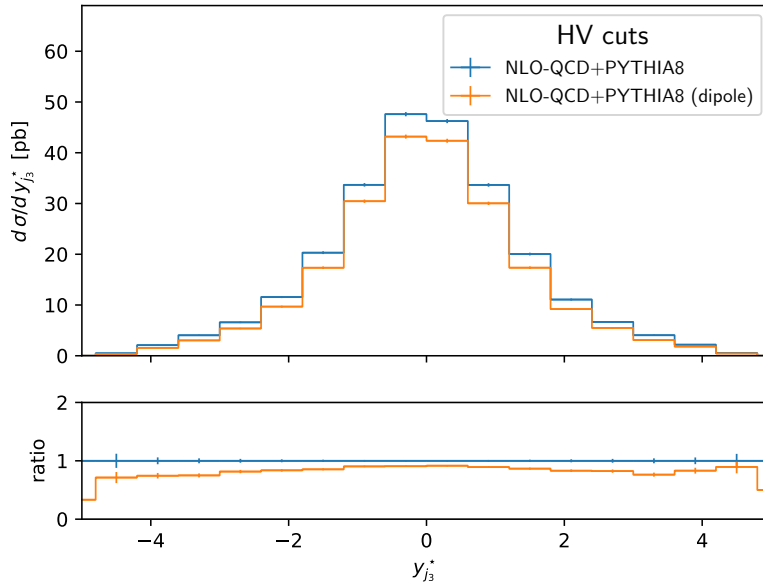


Figure 6.13: $y_{j_3}^*$ variable of the third-hardest jet at NLO-QCD+PS accuracy with the default global recoil scheme (blue) and the dipole recoil scheme (orange) of `PYTHIA8` within the HV cuts of Eqs. (6.7)–(6.8) and the extra requirements of Eq. (6.9) on the third jet. The ratio of the dipole to the default shower result is shown in the lower panel. Error bars indicate statistical errors.

of this effect in the future, eventually leading to a general recommendation for a recoil scheme in the analysis of the full EW Hjj process.

I will now turn to a discussion of the results with NLO-EW corrections and QED shower effects. Again, I start with some results within the inclusive cut set of Eqs. (6.7)–(6.8). Here, the NLO-EW corrections modify the integrated cross section by -6% (see Tab. 6.2), which agrees with the expectation from related work in the literature [43]. This number also supports the statement that the NLO-EW corrections to the EW production of Hjj are as important as the QCD corrections or can be even more important. In contrast to the NLO-QCD corrections, only very small differences between the effects of the NLO-EW corrections within the different cut sets can be observed: for the VBF setup, our calculation shows NLO-EW effects of -9% , whereas the cross section in the

Table 6.2: Integrated cross section at LO, NLO-EW, and NLO-EW+PS level within the different cut sets, including statistical errors.

Cut set	LO	NLO-EW	NLO-EW+PS
Inclusive cuts	3.250(2) pb	3.0520(9) pb	3.0520(14) pb
VBF cuts	0.9543(6) pb	0.8708(4) pb	0.8693(12) pb
HV cuts	0.6110(14) pb	0.5703(7) pb	0.5704(10) pb

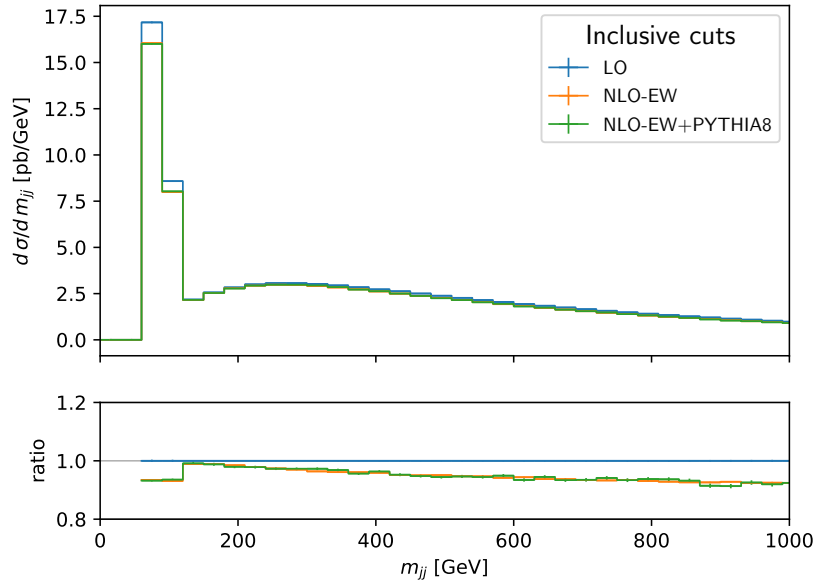


Figure 6.14: Invariant-mass distribution of the tagging jet system at LO (blue), NLO-EW (orange) and NLO-EW+PS (green) within the inclusive cuts of Eqs. (6.1)–(6.2). The ratio with respect to the LO results is shown in the lower panel. Error bars indicate statistical errors.

HV setup is reduced by 7% due to the NLO-EW corrections.

However, it turns out that the effects of the QED shower on the results of NLO-EW are only very small and nearly negligible: they reach from only +0.01% within the inclusive cut set over +0.02% for the HV cut set to -0.2% for the VBF cuts. Given the size of the QED coupling constant α_{em} , which is roughly one order of magnitude smaller than the QCD coupling constant α_s , this was to be expected. For this reason, I will focus on the effects of the NLO-EW corrections when discussing the results.

In Fig. 6.14, I show again the the familiar distribution of the invariant mass of the two jets m_{jj} , now with NLO-EW corrections and within the inclusive setup. We can see here that the LO curve slightly exceeds the NLO-EW curve over the whole range of the distribution, but especially at very large values of m_{jj} . This is the region where Sudakov suppression effects as described in Chap. 4 become important. I will come back to this behaviour when discussing the results within the more exclusive VBF cut set.

The relatively flat reduction of the cross section over the whole phase space by the NLO-EW corrections can also be seen in Fig. 6.15, where I show the distribution of the rapidity difference of the two tagging jets, Δy_{jj} . We had seen during the above discussion of the NLO-QCD result that the central region of this plot is dominated by s -channel contributions of the HV type, whereas the VBF process mainly contributes to the two peaks at $|\Delta y_{jj}| \gtrsim 4.5$. The fact that both parts of the distribution are affected by the NLO-EW corrections to similar extent fits well with the observation that the integrated

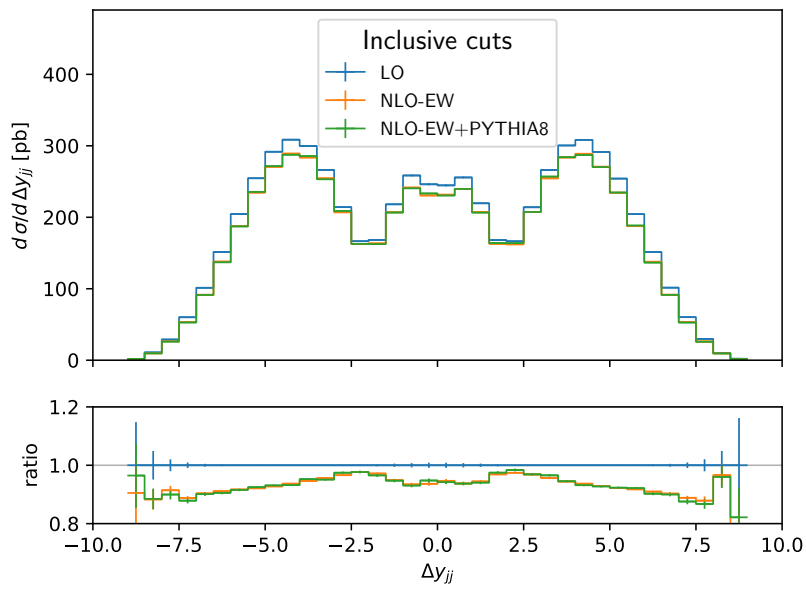


Figure 6.15: Rapidity difference of the two tagging jets at LO (blue), NLO-EW (orange) and NLO-EW+PS (green) within the inclusive cuts of Eqs. (6.1)–(6.2). The ratio with respect to the LO results is shown in the lower panel. Error bars indicate statistical errors.

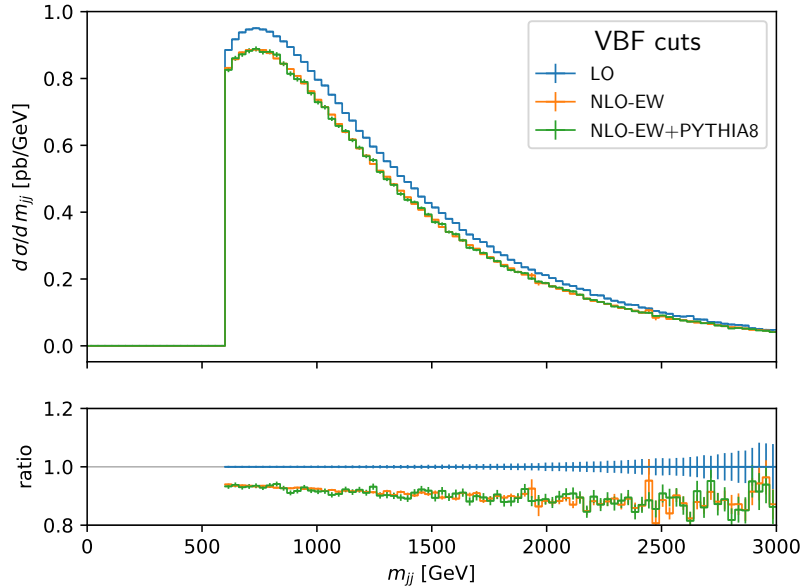


Figure 6.16: Invariant-mass distribution of the tagging jet system at LO (blue), NLO-EW (orange) and NLO-EW+PS (green) within the VBF cuts of Eqs. (6.3)–(6.6). The ratio with respect to the LO results is shown in the lower panel. Error bars indicate statistical errors.

cross section both within the HV and the VBF cut set was reduced by nearly the same amount by these corrections.

In Fig. 6.16, I again show the distribution of the invariant mass of the tagging jet system, m_{jj} , now within the VBF cut set of Eqs. (6.3)–(6.6). Here, the ratio plot in the lower panel confirms that the reduction by the NLO-EW corrections is slightly more pronounced at higher invariant masses where the Sudakov effects play a more important role. Similarly, the largest effect on the distribution of the transverse momentum of the hardest tagging jet p_{T,j_1} can be seen at large values of p_{T,j_1} , as shown in Fig. 6.17. Both plots show that, even within the VBF cut set where the shower effects on the integrated cross section are the most pronounced, the curve with NLO-EW and shower effects lies nearly perfectly on top of the one without shower effects.

For the rapidity distributions of the tagging jets, we can barely observe differences between the NLO-EW and the NLO-EW+PS results either. This can be seen for example in the rapidity distribution of the hardest jet, y_{j_1} , or the rapidity difference between the two tagging jets, Δy_{jj} , which are shown in Fig. 6.18 and Fig. 6.19, respectively.

Moving on to the effect of NLO-EW corrections and a QED PS in the HV setup of Eqs. (6.7) - (6.8), we see a similar pattern as within the VBF cut set before: the NLO-EW corrections usually yield negative contributions over the whole range of the distribution, leading to a flat reduction in normalisation by 5% – 10%. This can be seen for example in Fig. 6.20, where the transverse momentum of the Higgs boson is depicted,

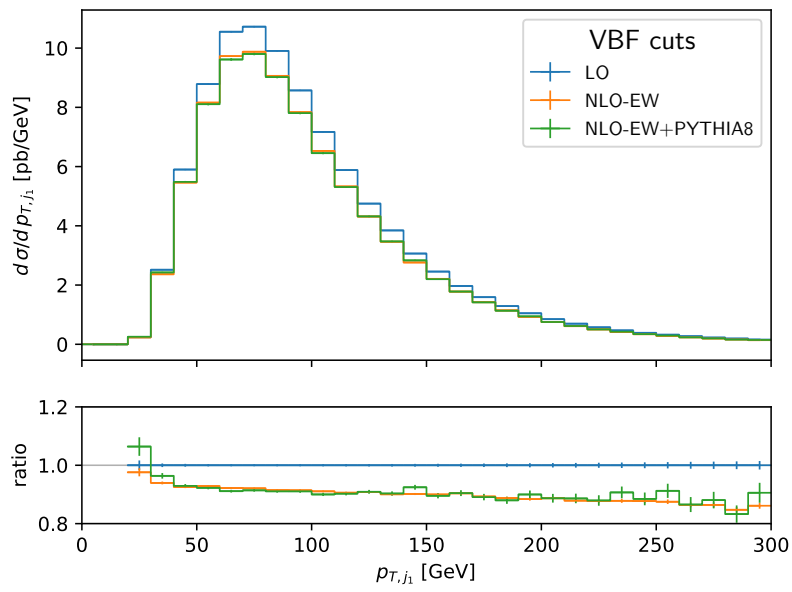


Figure 6.17: Transverse momentum distribution of the hardest tagging jet at LO (blue), NLO-EW (orange) and NLO-EW+PS (green) within the VBF cuts of Eqs. (6.3)–(6.6). The ratio with respect to the LO results is shown in the lower panel. Error bars indicate statistical errors.

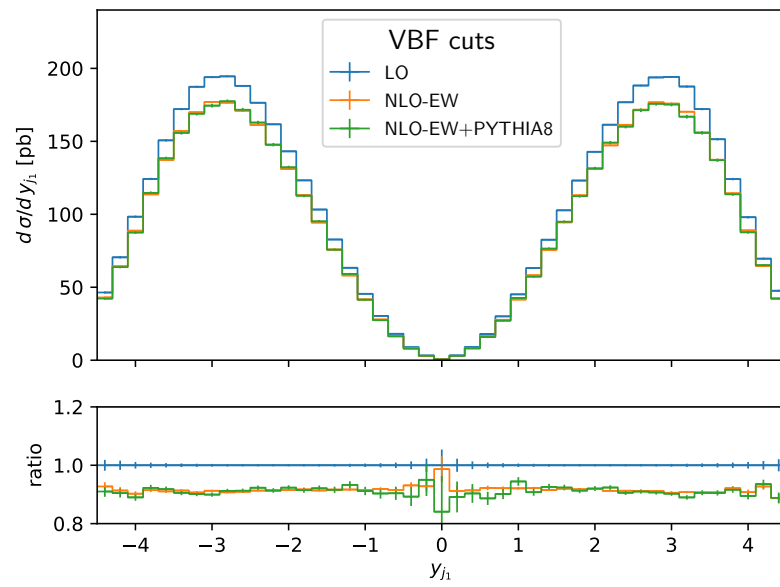


Figure 6.18: Rapidity distribution of the hardest tagging jet at LO (blue), NLO-EW (orange) and NLO-EW+PS (green) within the VBF cuts of Eqs. (6.3)–(6.6). The ratio with respect to the LO results is shown in the lower panel. Error bars indicate statistical errors.

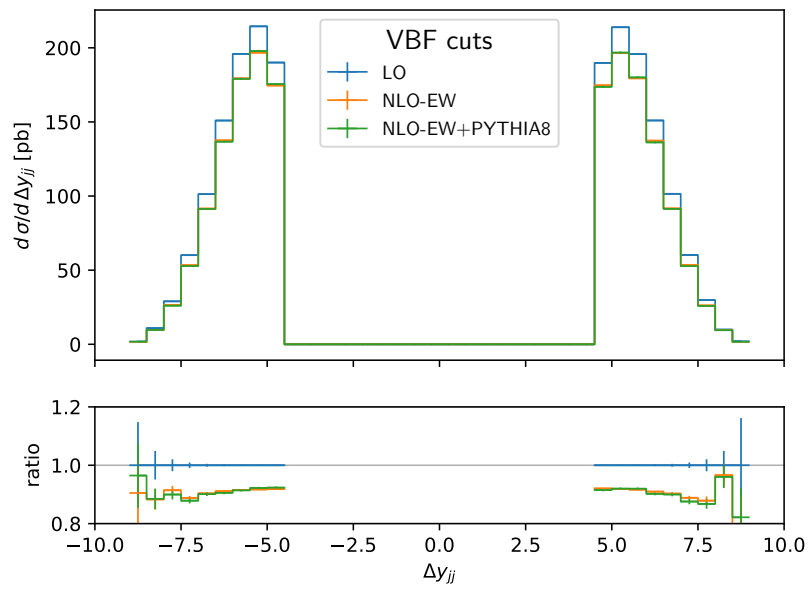


Figure 6.19: Rapidity difference of the tagging jets at LO (blue), NLO-EW (orange) and NLO-EW+PS (green) within the VBF cuts of Eqs. (6.3)–(6.6). The ratio with respect to the LO results is shown in the lower panel. Error bars indicate statistical errors.

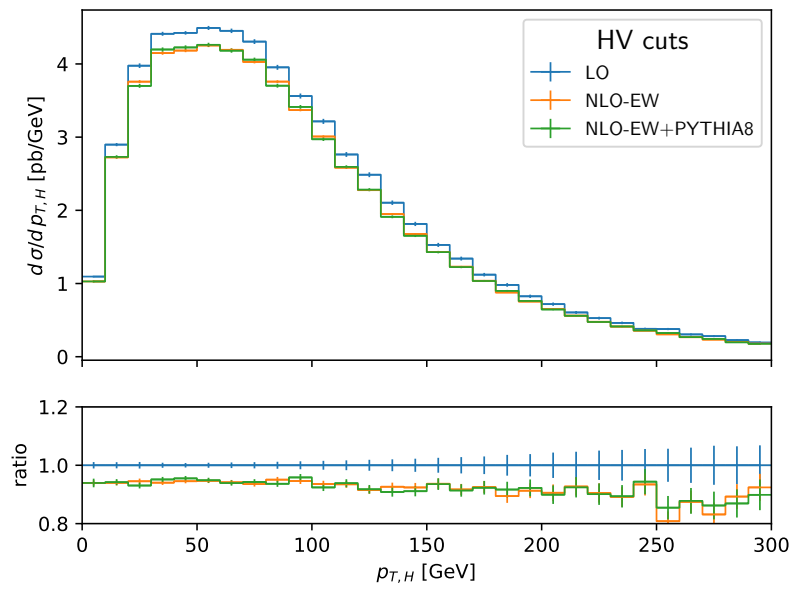


Figure 6.20: Transverse momentum distribution of the Higgs boson at LO (blue), NLO-EW (orange) and NLO-EW+PS (green) within the HV cuts of Eqs. (6.7)–(6.8). The ratio with respect to the LO results is shown in the lower panel. Error bars indicate statistical errors.

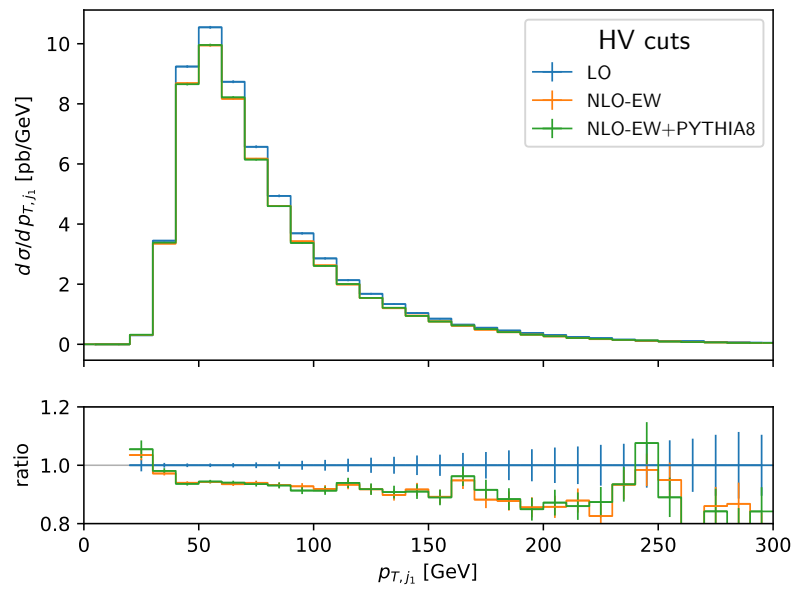


Figure 6.21: Transverse momentum distribution of the hardest tagging jet at LO (blue), NLO-EW (orange) and NLO-EW+PS (green) within the HV cuts of Eqs. (6.7)–(6.8). The ratio with respect to the LO results is shown in the lower panel. Error bars indicate statistical errors.

and in the distribution of the transverse momentum p_{T,j_1} of the hardest jet in Fig. 6.21.

In contrast to the QCD PS considered before, there is no need for a dipole recoil when employing a QED shower with the EW Hjj production process. While conservation laws suppress a colour flow between the quark lines in the VBF process, no similar limitation applies for EW corrections to both the VBF and the HV process. For this reason, and since the QED shower effects are already very limited, there is no need for comparing the two shower schemes for the QED shower.

Chapter 7

Conclusions and Outlook

In this thesis, I presented a study of the EW Hjj production process including NLO-QCD and NLO-EW corrections as well as QCD and QED shower effects. I started by a recap of the basic features of QFT in general and the SM of particle physics in particular, with a strong emphasis on the EW sector the SM and the so-called Higgs mechanism. By discussing the limitations of the SM and describing the search for new physics described by BSM theories, I illustrated one of the main motivations for high precision calculations within the SM. In Chap. 3, I elaborated on how precision calculations are performed in the frameworks of NLO calculations and parton showers. The POWHEG method was introduced as one of the most successful methods to combine the two different approaches.

In Chap. 4, I described the process of EW Hjj production, which actually consists of two sub-processes: the VBF process and the HV process. I explained why the two processes are of particular interest for the search for new physics, establishing the importance of precision calculations for the VBF and the HV process. I also explained why especially the VBF process, while not being the dominating production mode for the Higgs boson, can still be examined very well experimentally. In the same chapter, by using the argument of Sudakov enhanced NLO EW corrections, I showed why these corrections should not be neglected in comparison to the NLO-QCD ones for the EW Hjj production process. I then concluded the chapter by summarising that the experimental and theoretical features of the process, as well as the importance of the EW corrections, call for an implementation of the process at NLO-EW precision that allows for a matching to an SMC.

Following up on that account, we developed an implementation of the EW Hjj production within the POWHEG framework to allow for the matching to the PYTHIA8 shower that includes both the NLO-QCD corrections as well as, for the first time ever, the NLO-EW corrections. This implementation was described in Chap. 5, where I also introduced the programs and software frameworks that were used for our implementation. I elaborated on the particular difficulties that are connected to EW corrections within the POWHEG BOX framework, and why the phase space structure of the EW Hjj production process calls for a special treatment of the phase space integration. The chapter was concluded by a description of the extensive tests that we performed on our code in order

to verify its correct behaviour, especially by comparing intermediate results to existing calculations.

In the final Chap. 6, I finally discussed the phenomenology of the EW Hjj production process by showing numerical results that have been generated by using the new implementation described before. These results were supplemented by results from an earlier study, where we compared different implementations of the VBF process at the NLO-QCD+PS level.

As illustrated in that chapter, our code is able to reproduce existing results at NLO-QCD and NLO-QCD+PS accuracy very well, including subtle features such as the sensitivity of the VBF contributions to specific PS recoil schemes. Our results including the NLO-EW corrections clearly confirmed their importance, as they accounted for reductions of the cross section by almost 10% and are thus comparable in size to the NLO-QCD corrections. However, our results showed that the impact of a QED shower is only very moderate.

The significance of the tool we developed extends far beyond the exemplary phenomenological study that we performed. It can serve as a tool for experimentalists to refine the analysis of the VBF and the HV processes and leaves room for a whole range of follow-up work. For example, it would be possible with reasonable effort to combine the NLO-EW corrections with a full QCD+QED shower. However, since this would mean to combine a QCD shower with a fixed-order calculation that is effectively at LO w.r.t. QCD, one would spoil the potential of the NLO matching that the POWHEG method allows for. For this reason, we suggest that our tool be extended in the future by combining the QCD and EW NLO corrections simultaneously.

We also suggest to use the POWHEG BOX RES process that was presented in this thesis to perform a study of the ideal setup of the QCD shower for the full EW Hjj process with a special emphasis on the shower matching scheme. Moreover, one could make use of the versatility of the RECOLA amplitudes that our program is based on to examine the influence of BSM physics, e.g. in the framework of anomalous couplings.

In conclusion, our tool has filled a prominent gap in the precision calculations for an important Higgs production process, and paves the ground for a variety of possible follow-up studies and extensions to continue the research on the EW Hjj production.

Acknowledgments

I am grateful for generous financial and non-material support by the *German Academic Scholarship Foundation* (Studienstiftung des deutschen Volkes). Our work has been supported by the state of Baden-Württemberg through *bwHPC*. We furthermore acknowledge support by the German Federal Ministry for Education and Research (BMBF) under grant number 05H18VTCA1 and the German Research Foundation (DFG) through Grant no INST 39/963-1 FUGG for the work on [1], as well as support by the DFG through grant no. JA 1954/2-1 for [2].

We are grateful for valuable discussions with Margherita Ghezzi, Alexander Karlberg, Seth Quackenbusch and Laura Reina. I want to express my special gratitude to M.G. for extensive support especially in the early stadium of my Ph. D. studies and for proofreading my thesis, as well as to A.K. for being a very reliable and patient two-time co-author to me.

I especially want to thank my supervisor, Prof. Barbara Jäger, who has supported me since my late bachelor studies and whom I will remember as a very supportive, fair and caring supervisor. I am very grateful to her for motivating and enabling me to pursue my academic career up until this point.

Furthermore, I want to express my gratitude to Marco Stratmann, who gave me the possibility to discover my passion for teaching physics to younger students and to work as a tutor for the *Grundkurs Physik* in Tübingen, which were always excellently organised by M.S. I also want to thank all the colleagues at the Institute for Theoretical Physics, who not only supported me through valuable discussions, but have become real friends: Santiago Lopez Portillo Chavez, who also agreed to proofread this thesis, Gabriele Coniglio, Christoph Borschensky, Robin Feser, Felix Reichenbach, Felix Kunzelmann, Melih Gül, Julien Baglio, and many more. I am also grateful for valuable discussions with the other professors on our floor, especially Werner Vogelsang, Thomas Gutsche, who accompanied me through my studies from the very first lecture, and Jan-Philipp Burde.

Finally, I want to thank Hannes Jung from DESY in Hamburg, who sparked my interest in particle physics as early as in my 11th high school year.

Last but not least, I am very grateful for the important support that I received from my family throughout the last years and months, especially from my wife Ella.

Appendix A

Installing and Compiling the Code

The program `POWHEG_BOX_RES` can be downloaded via `SVN` from the project's web site at <https://powhegbox.mib.infn.it/> by executing the command

```
$ svn checkout --username anonymous --password anonymous \  
svn://powhegbox.mib.infn.it/trunk/POWHEG-BOX-RES
```

By adding the option `--revision n`, a specific revision number `n` can be checked out. Our subprocess was tested and found to work with revision 3923, which was also used to produce the results presented here.

We intend to get the process code available for download via `SVN` under the name `HJJ_ew` from the `POWHEG_BOX_RES` site as well. The code can then be downloaded by executing the following command inside the `POWHEG_BOX_RES` directory:

```
$ svn checkout --username anonymous --password anonymous \  
svn://powhegbox.mib.infn.it/trunk/User-Processes-RES/HJJ_ew
```

The process code depends on `RECOLA2` and `COLLIER` being installed. We tested our program against version 2.2.2 of `RECOLA2` and version 1.2.5 of `COLLIER`, which were the most recent versions at the time of publication. The path to the installation directory of `RECOLA2` has to be specified in the `Makefile` of the process by setting the variable `RCLPATH`. The code furthermore depends on `PYTHIA8` (8.240), `FastJet` (3.3.0) and `LHAPDF` (6.2.1) being installed. The numbers in brackets indicate the respective program versions that were used for this thesis.

For this thesis, the code was run on `CentOS 7.9, Rev 21`, but we expect it to work with little or no modifications necessary on any `UNIX*` system. The main program can be compiled by executing the command `make` inside the project directory, and the `PYTHIA8` interface by running `make main-PYTHIA8-lhef`. Per default, `make` will then invoke `gfortran` and, in case of the command `make main-PYTHIA8-lhef`, `g++` for compilation and linking. We found the code to be compilable with the version 7.3.0 of the `gnu` compiler package, whereas we found a software bug in the versions 8.1.0 and 8.2.0 that will lead to the `POWHEG_BOX_RES` terminating on execution when compiled with any of these versions. It is important to note that our code was never tested with the proprietary `Intel® Fortran Compiler` and we cannot guarantee compatibility with this compiler.

After successful compilation, the main program is invoked in the usual way of the POWHEG BOX by running the executable `pwhg_main` inside any directory containing an input file under the name `powheg.input`. We will provide an example for such an input file in the directory `testrun-lhc`, and the main features are also explained in the next part of the Appendix B. After generating an `.lhe` event file with the main process, this can be showered with PYTHIA8 by running `main-PYTHIA8-lhef`. For more details, the reader is referred to the program manual.

Appendix B

Input Parameters

In this chapter, I will list and explain the input parameters that are necessary for running our process code or can be used in order to control the calculation. According to the standard input scheme of the `POWHEG BOX`, all input parameters are given in a single file (usually named `powheg.input`), where each line contains one parameter following the syntax

```
parameter_name  value ! optional comment
```

Everything behind a `!` until the end of the line is regarded as a comment and thus ignored by the program. Unless stated otherwise, the exemplary values in this section correspond to the actual values that have been used for the calculation presented in this thesis.

I begin with the very basic parameters that need to be set for every `POWHEG BOX` run. Amongst them, the most important are the parameters to control the hadronic part of the simulated collision, i.e. the collision energy, the type of colliding hadrons, and the PDF sets to be used. For the latter, the user can choose between using the `LHAPDF` sets or an internal PDF set.

```
! Basic collider parameters
ih1      1                ! hadron 1 (1 for protons ,
                        ! -1 for antiprotons)
ih2      1                ! hadron 2 (1 for protons ,
                        ! -1 for antiprotons)
ebeam1   6500d0          ! energy of beam 1
ebeam2   6500d0          ! energy of beam 2
!
! Parameters corresponding to the PDF sets
! ndns is to be set only if using internal (mlm) pdfs
! ndns1 131              ! pdf set for hadron 1 (mlm numbering)
! ndns2 131              ! pdf set for hadron 2 (mlm numbering)
! lhans is to be set only if using LHA pdfs
lhans1   324900          ! pdf set for hadron 1 (LHA numbering)
```

```
lhans2 324900      ! pdf set for hadron 2 (LHA numbering)
!
```

The POWHEG BOX also needs to know the level of statistics that the user wishes to have, i.e. the number of iterations and the number of calls per iteration for the different stages of the calculation. If the user wishes, the program can also re-use existing grid and upper bounding data to save computation time. At this point, I want to emphasize that the parameters concerning the level of statistics correspond to the calls and iterations *per seed* if the calculation is parallelised using the `manyseeds` option (see below). Thus, the exemplary numbers in this file are not sufficient for satisfactory results with only one seed.

```
! Parameters to control the statistics ,
! i.e. number of calls and iterations
ncall1      80000      ! number of calls for initializing
                ! the integration grid
itmx1       5          ! number of iterations for initializing
                ! the integration grid
ncall2      80000      ! number of calls for computing
                ! the integral and finding
                ! upper bounding envelope
itmx2       5          ! number of iterations for computing
                ! the integral and finding
                ! upper bounding envelope
foldesi     2          ! number of folds on csi integration
foldy       2          ! number of folds on y integration
foldphi     2          ! number of folds on phi integration
nubound     10000     ! number of calls to set up the
                ! upper bounding norms for radiation
numevts     5000      ! number of events to be generated
!
! Parameters to allow or not the use of stored data
use-old-grid 1        ! if 1, use old grid if file
                ! pwggrids.dat is present;
                ! <> 1 regenerate
use-old-ubound 1     ! if 1, use norm of upper
                ! bounding function stored
                ! in pwgubound.dat, if present;
                ! <> 1 regenerate
```

With this input, the user could in principle already start a full run of the program. However, it is recommended to refine the settings with optional parameters. Some of them are universal to every POWHEG BOX process and mainly steer technical details of the program. However, three of them deserve special attention: the flag `bornonly` has to be set to 1 if LO calculations are desired and to 0 otherwise, the flag `nores` can be

used to switch off the resonance-aware mechanism of the tool, and `alphas_from_lhapdf` tells the program to obtain the value of α_s from the LHAPDF pdf set instead from an internal calculation. Finally, in the version `POWHEG BOX RES`, the user can also activate the feature `allrad` here to allow for multiple radiation from different radiation regions within one event.

```
! OPTIONAL POWHEG PARAMETERS
withnegweights      1          ! if 1, use negative weights
!xupbound           2d0        ! increase upper bound
                                ! for radiation generation
alphas_from_lhapdf  1          ! obtain the value of alpha_s
                                ! from the PDF set
!renscfact          1d0        ! ren. scale factor:
                                ! muren = muref * renscfact
!facscfact          1d0        ! fac. scale factor:
                                ! mufact = muref * facscfact

fastbtlbound        1
storemintupb        0
check_bad_st2       1          ! Discard 'bad' seeds after stage 2
bornonly            0          ! Do Born only
nores               0          ! DO NOT use resonance histories
withdamp            1          ! Use Born-zero damping factor
testplots           1          ! Do NLO and PWHG distributions
allrad              0
```

Additionally, the optional parameters can be used to control the internal random number generator of the `POWHEG BOX`, and to run the program on multiple cores in parallel. I refer to Sec. 5 for details of this feature. If the user wants to activate this feature, the run directory has to contain a file named `pwgseeds.dat`, containing one individual integer number per line. The program, when run with the option `manyseeds` activated, will then ask for an integer j , and the integer at line j in `pwgseeds.dat` is used as seed for the random number generator. The output files of this run, including the event file, then will contain the integer j in the file names for identification. As explained in Sec. 5, the program will perform only one iteration of one stage when invoked in parallel mode. The number of the next stage and iteration is also set in the input file. If the user starts multiple runs, they should wait for every process of one iteration/stage to be finished before starting the next. This enable the program to combine the outputs of the last runs as input for the new runs.

```
!
! RNG input
iseed  1337          ! Start the random number generator
                                ! with seed iseed
!rand1  0            ! skipping rand2*100000000+rand1 numbers.
!rand2  0            ! (see RM48 short writeup in CERNLIB)
```

```

!
! For running on multiple cores in parallel
manyseeds      1      ! Used to perform multiple runs
parallelstage  1      ! Select stage of the calculation
                  ! (when parallelised)
xgriditeration 1      ! Select iteration (when parallelised)
maxseeds 1000      ! max. number of seeds

```

Finally, we come to the input parameters specific to our process. Most of them concern physical input such as masses. Here, it is worth noticing that the values used for the calculation in this thesis and the accompanying publication correspond to the default parameters of the program. Consequently, the user does not to explicitly enter them via the input file if they wish to keep these values.

```

! Physical parameters
!hmass      125d0      ! Higgs boson mass
!hwidth     0d0        ! Higgs boson width
!wmass      80.352d0   ! W boson mass
!wwidth     2.084d0   ! W boson width
!zmass      91.153d0   ! Z boson mass
!zwidth     2.494d0   ! Z boson width
!tmass      172.754    ! top quark mass
!gfermi     1.1663787d-05 ! Fermi constant

```

With the help of the option `runningscales`, the user can select different kinematic invariants to derive the renormalisation and factorisation scales, and by setting the flag `fakevirt`, the virtual amplitudes are approximated based on the Born amplitudes to save computation time. It is highly recommended to use the latter flag only in the first stage of a parallelised calculation! Activating this flag at a later stage will spoil the NLO accuracy of the results. The user can also select by employing the flag `qed_qcd` whether they want to perform calculations with NLO-QCD or with NLO-EW corrections.

```

! Parameters for NLO calculations
runningscales      1      ! 0: use fixed scale ,
                    ! 1: use  $\sum_{i=1}^{n_{\text{partfin}}}$ 
                    !  $(p_{t_i} + \sqrt{M_H^2 + p_{t_i}^2})/2$  ,
                    ! 2: use  $(P_T(p_1) + P_T(p_2))/2$ 
fakevirt           0      ! Approximate virtuals by
                    !  $\alpha * \text{Born}$  or  $\alpha_s * \text{Born}$ 
qed_qcd            1      ! 0: NLO-QCD only , 1: NLO-EW only

```

Appendix C

List of Abbreviations

ABEGHHK'tH	Anderson-Brout-Englert-Guralnik-Hagen-Higgs-Kibble-'t Hooft
ATLAS	A Toroidal LHC Apparatus
BSM	Beyond the Standard Model
CERN	Conseil européen pour la recherche nucléaire
CMS	Compact-Muon-Solenoid
DIS	Deep inelastic scattering
DOF	Degree of freedom
DREG	Dimensional regularisation
EFT	Effective field theory
EW	Electroweak
HL-LHC	High luminosity LHC
HV	Higgs-boson + vector boson (undecayed final state of the Higgsstrahlung process)
IR	Infrared
KLN	Kinoshita-Lee-Nauenberg (theorem)
LHC	Large Hadron Collider
LHE	Les Houches event
LO	Leading order
MS	Minimal subtraction (scheme)

$\overline{\text{MS}}$	Modified minimal subtraction (scheme)
MSSM	Minimal supersymmetric extension of the Standard Model
NLO	Next-to-leading order
NNLO	Next-to-next-to-leading order
N³LO	Next-to-next-to-next-to-leading order
PDF	Parton distribution function
PS	Parton shower
PSP	Phase space point
QCD	Quantum chromodynamics
QED	Quantum electrodynamics
QFT	Quantum field theory
SM	Standard Model
SMC	Shower Monte Carlo generator
SUSY	Supersymmetry
UV	Ultraviolet
VBF	Vector boson fusion

Bibliography

- [3] J.W. von Goethe, *Faust. Eine Tragödie*, Cotta, Tübingen (1808).
- [4] J. Dalton, *A New System of Chemical Philosophy*, R. Bickerstaff, Manchester (1808).
- [5] J.J. Thomson, M.A. F.R.S., *XL. Cathode Rays*, *The London, Edinburgh, and Dublin Philosophical Magazine and Journal of Science* **44** (1897) 293.
- [6] J.J. Thomson, M.A. F.R.S., *XXIV. On the structure of the atom: an investigation of the stability and periods of oscillation of a number of corpuscles arranged at equal intervals around the circumference of a circle; with application of the results to the theory of atomic structure*, *The London, Edinburgh, and Dublin Philosophical Magazine and Journal of Science* **7** (1904) 237.
- [7] E. Rutherford, F.R.S., *LXXIX. The scattering of α particles by matter and the structure of the atom*, *The London, Edinburgh, and Dublin Philosophical Magazine and Journal of Science* **21** (1911) 669.
- [8] N. Bohr, *I. On the constitution of atoms and molecules*, *The London, Edinburgh, and Dublin Philosophical Magazine and Journal of Science* **26** (1913) 1.
- [9] A. Sommerfeld, *Zur Quantentheorie der Spektrallinien*, *Annalen der Physik* **356** (1916) 1.
- [10] C.N. Yang and R.L. Mills, *Conservation of Isotopic Spin and Isotopic Gauge Invariance*, *Phys. Rev.* **96** (1954) 191.
- [11] S.L. Glashow, *Partial-symmetries of weak interactions*, *Nuclear Physics* **22** (1961) 579.
- [12] F. Englert and R. Brout, *Broken Symmetry and the Mass of Gauge Vector Mesons*, *Phys. Rev. Lett.* **13** (1964) 321.
- [13] P. Higgs, *Broken symmetries, massless particles and gauge fields*, *Physics Letters* **12** (1964) 132.
- [14] P.W. Higgs, *Broken Symmetries and the Masses of Gauge Bosons*, *Phys. Rev. Lett.* **13** (1964) 508.

- [15] G.S. Guralnik, C.R. Hagen and T.W.B. Kibble, *Global Conservation Laws and Massless Particles*, *Phys. Rev. Lett.* **13** (1964) 585.
- [16] S. Weinberg, *A Model of Leptons*, *Phys. Rev. Lett.* **19** (1967) 1264.
- [17] A. Salam, *Weak and Electromagnetic Interactions*, *Conf. Proc. C* **680519** (1968) 367.
- [18] ATLAS collaboration, *Observation of a new particle in the search for the Standard Model Higgs boson with the ATLAS detector at the LHC*, *Phys. Lett. B* **716** (2012) 1 [1207.7214].
- [19] CMS collaboration, *Observation of a New Boson at a Mass of 125 GeV with the CMS Experiment at the LHC*, *Phys. Lett. B* **716** (2012) 30 [1207.7235].
- [20] J. Elias-Miro, J.R. Espinosa, E. Masso and A. Pomarol, *Higgs windows to new physics through $d=6$ operators: constraints and one-loop anomalous dimensions*, *JHEP* **11** (2013) 066 [1308.1879].
- [21] H. Rzehak, “Looking through the Higgs window for new physics.” Talk given at the University of Vienna, https://physik.univie.ac.at/fileadmin/user_upload/f_physik/04_Events/2019/Heidi_Rzehak_24.05.2019.pdf, 2019.
- [22] T. Han, G. Valencia and S. Willenbrock, *Structure function approach to vector boson scattering in $p p$ collisions*, *Phys. Rev. Lett.* **69** (1992) 3274 [hep-ph/9206246].
- [23] T. Figy, C. Oleari and D. Zeppenfeld, *Next-to-leading order jet distributions for Higgs boson production via weak boson fusion*, *Phys. Rev. D* **68** (2003) 073005 [hep-ph/0306109].
- [24] E.L. Berger and J.M. ll, *Higgs boson production in weak boson fusion at next-to-leading order*, *Phys. Rev. D* **70** (2004) 073011 [hep-ph/0403194].
- [25] K. Arnold et al., *VBFNLO: A Parton level Monte Carlo for processes with electroweak bosons*, *Comput. Phys. Commun.* **180** (2009) 1661 [0811.4559].
- [26] J.M. Campbell and R.K. Ellis, *Next-to-Leading Order Corrections to W^+ 2 jet and Z^+ 2 Jet Production at Hadron Colliders*, *Phys. Rev. D* **65** (2002) 113007 [hep-ph/0202176].
- [27] O. Brein, R.V. Harlander and T.J.E. Zirke, *vh@nnlo - Higgs Strahlung at hadron colliders*, *Comput. Phys. Commun.* **184** (2013) 998 [1210.5347].
- [28] T. Figy, V. Hankele and D. Zeppenfeld, *Next-to-leading order QCD corrections to Higgs plus three jet production in vector-boson fusion*, *JHEP* **02** (2008) 076 [0710.5621].

- [29] P. Bolzoni, F. Maltoni, S.-O. Moch and M. Zaro, *Higgs production via vector-boson fusion at NNLO in QCD*, *Phys. Rev. Lett.* **105** (2010) 011801 [1003.4451].
- [30] P. Bolzoni, F. Maltoni, S.-O. Moch and M. Zaro, *Vector boson fusion at NNLO in QCD: SM Higgs and beyond*, *Phys. Rev. D* **85** (2012) 035002 [1109.3717].
- [31] M. Cacciari, F.A. Dreyer, A. Karlberg, G.P. Salam and G. Zanderighi, *Fully Differential Vector-Boson-Fusion Higgs Production at Next-to-Next-to-Leading Order*, *Phys. Rev. Lett.* **115** (2015) 082002 [1506.02660].
- [32] J. Cruz-Martinez, T. Gehrmann, E.W.N. Glover and A. Huss, *Second-order QCD effects in Higgs boson production through vector boson fusion*, *Phys. Lett. B* **781** (2018) 672 [1802.02445].
- [33] B.A. Kniehl, *Associated production of higgs and z bosons from gluon fusion in hadron collisions*, *Phys. Rev. D* **42** (1990) 2253.
- [34] O. Brein, A. Djouadi and R. Harlander, *NNLO QCD corrections to the Higgs-strahlung processes at hadron colliders*, *Phys. Lett. B* **579** (2004) 149 [hep-ph/0307206].
- [35] O. Brein, R. Harlander, M. Wiesemann and T. Zirke, *Top-Quark Mediated Effects in Hadronic Higgs-Strahlung*, *Eur. Phys. J. C* **72** (2012) 1868 [1111.0761].
- [36] G. Ferrera, M. Grazzini and F. Tramontano, *Associated WH production at hadron colliders: a fully exclusive QCD calculation at NNLO*, *Phys. Rev. Lett.* **107** (2011) 152003 [1107.1164].
- [37] G. Ferrera, M. Grazzini and F. Tramontano, *Associated ZH production at hadron colliders: the fully differential NNLO QCD calculation*, *Phys. Lett. B* **740** (2015) 51 [1407.4747].
- [38] J.M. Campbell, R.K. Ellis and C. Williams, *Associated production of a Higgs boson at NNLO*, *JHEP* **06** (2016) 179 [1601.00658].
- [39] G. Ferrera, G. Somogyi and F. Tramontano, *Associated production of a Higgs boson decaying into bottom quarks at the LHC in full NNLO QCD*, *Phys. Lett. B* **780** (2018) 346 [1705.10304].
- [40] F.A. Dreyer and A. Karlberg, *Vector-Boson Fusion Higgs Production at Three Loops in QCD*, *Phys. Rev. Lett.* **117** (2016) 072001 [1606.00840].
- [41] A. Karlberg, *At the Frontier of Precision QCD in the LHC Era*, Ph.D. thesis, Merton Coll., Oxford, 2016. 1610.06226.
- [42] M. Ciccolini, S. Dittmaier and M. Kramer, *Electroweak radiative corrections to associated WH and ZH production at hadron colliders*, *Phys. Rev. D* **68** (2003) 073003 [hep-ph/0306234].

- [43] M. Ciccolini, A. Denner and S. Dittmaier, *Electroweak and QCD corrections to Higgs production via vector-boson fusion at the LHC*, *Phys. Rev. D* **77** (2008) 013002 [0710.4749].
- [44] M. Ciccolini, A. Denner and S. Dittmaier, *Strong and electroweak corrections to the production of Higgs + 2jets via weak interactions at the LHC*, *Phys. Rev. Lett.* **99** (2007) 161803 [0707.0381].
- [45] T. Figy, S. Palmer and G. Weiglein, *Higgs Production via Weak Boson Fusion in the Standard Model and the MSSM*, *JHEP* **02** (2012) 105 [1012.4789].
- [46] A. Denner, S. Dittmaier, S. Kallweit and A. Muck, *Electroweak corrections to Higgs-strahlung off W/Z bosons at the Tevatron and the LHC with HAWK*, *JHEP* **03** (2012) 075 [1112.5142].
- [47] A. Denner, S. Dittmaier, S. Kallweit and A. Mück, *HAWK 2.0: A Monte Carlo program for Higgs production in vector-boson fusion and Higgs strahlung at hadron colliders*, *Comput. Phys. Commun.* **195** (2015) 161 [1412.5390].
- [48] P. Nason and C. Oleari, *NLO Higgs boson production via vector-boson fusion matched with shower in POWHEG*, *JHEP* **02** (2010) 037 [0911.5299].
- [49] S. Frixione, P. Torrielli and M. Zaro, *Higgs production through vector-boson fusion at the NLO matched with parton showers*, *Phys. Lett. B* **726** (2013) 273 [1304.7927].
- [50] F. Campanario, T.M. Figy, S. Plätzer and M. Sjödaahl, *Electroweak Higgs Boson Plus Three Jet Production at Next-to-Leading-Order QCD*, *Phys. Rev. Lett.* **111** (2013) 211802 [1308.2932].
- [51] G. Luisoni, P. Nason, C. Oleari and F. Tramontano, *$HW^\pm/HZ + 0$ and 1 jet at NLO with the POWHEG BOX interfaced to GoSam and their merging within MiNLO*, *JHEP* **10** (2013) 083 [1306.2542].
- [52] F. Granata, J.M. Lindert, C. Oleari and S. Pozzorini, *NLO QCD+EW predictions for HV and HV +jet production including parton-shower effects*, *JHEP* **09** (2017) 012 [1706.03522].
- [53] S. Alioli, P. Nason, C. Oleari and E. Re, *A general framework for implementing NLO calculations in shower Monte Carlo programs: the POWHEG BOX*, *JHEP* **06** (2010) 043 [1002.2581].
- [54] P. Nason, *A New method for combining NLO QCD with shower Monte Carlo algorithms*, *JHEP* **11** (2004) 040 [hep-ph/0409146].
- [55] S. Frixione, P. Nason and C. Oleari, *Matching NLO QCD computations with Parton Shower simulations: the POWHEG method*, *JHEP* **11** (2007) 070 [0709.2092].

- [56] T. Sjostrand, S. Mrenna and P.Z. Skands, *PYTHIA 6.4 Physics and Manual*, *JHEP* **05** (2006) 026 [[hep-ph/0603175](#)].
- [57] cush (Wikimedia user), *Standard model of elementary particles*, last retrieved on 05th June, 2022. https://commons.wikimedia.org/wiki/File:Standard_Model_of_Elementary_Particles.svg.
- [58] SUPER-KAMIOKANDE COLLABORATION collaboration, *Evidence for Oscillation of Atmospheric Neutrinos*, *Phys. Rev. Lett.* **81** (1998) 1562.
- [59] H.E. Haber, *Introductory low-energy supersymmetry*, in *Theoretical Advanced Study Institute (TASI 92): From Black Holes and Strings to Particles*, pp. 589–686, 4, 1993 [[hep-ph/9306207](#)].
- [60] S. Dawson, *Electroweak Symmetry Breaking and Effective Field Theory*, in *Theoretical Advanced Study Institute in Elementary Particle Physics: Anticipating the Next Discoveries in Particle Physics*, pp. 1–63, 12, 2017, DOI [[1712.07232](#)].
- [61] PARTICLE DATA GROUP collaboration, *Review of Particle Physics*, *PTEP* **2022** (2022) 083C01.
- [62] R. Wolf, K. Köneke and H. Rzehak, *Wegweiser zu neuer Physik*, *Physik-Journal* **10** (2021) 42.
- [63] F. Abu-Ajamieh, *The Scale of New Physics from the Higgs Couplings to gg* , [2203.07410](#).
- [64] R.K. Ellis, W.J. Stirling and B.R. Webber, *QCD and Collider Physics*, Cambridge Monographs on Particle Physics, Nuclear Physics and Cosmology, Cambridge University Press (1996), [10.1017/CBO9780511628788](#).
- [65] S. Bethke, *Experimental tests of asymptotic freedom*, *Prog. Part. Nucl. Phys.* **58** (2007) 351 [[hep-ex/0606035](#)].
- [66] V. Bertone, S. Carrazza and J. Rojo, *APFEL: A PDF Evolution Library with QED corrections*, *Comput. Phys. Commun.* **185** (2014) 1647 [[1310.1394](#)].
- [67] V.N. Gribov and L.N. Lipatov, *Deep inelastic $e p$ scattering in perturbation theory*, *Sov. J. Nucl. Phys.* **15** (1972) 438.
- [68] Y.L. Dokshitzer, *Calculation of the Structure Functions for Deep Inelastic Scattering and $e+ e-$ Annihilation by Perturbation Theory in Quantum Chromodynamics.*, *Sov. Phys. JETP* **46** (1977) 641.
- [69] G. Altarelli and G. Parisi, *Asymptotic Freedom in Parton Language*, *Nucl. Phys. B* **126** (1977) 298.
- [70] G. Altarelli, *QCD evolution equations for parton densities*, *Scholarpedia* **4** (2009) 7124.

- [71] G.C. Wick, *The Evaluation of the Collision Matrix*, *Phys. Rev.* **80** (1950) 268.
- [72] M.D. Schwartz, *Quantum Field Theory and the Standard Model*, Cambridge University Press (2013), 10.1017/9781139540940.
- [73] G. 't Hooft and M.J.G. Veltman, *Regularization and Renormalization of Gauge Fields*, *Nucl. Phys. B* **44** (1972) 189.
- [74] A. Denner and S. Dittmaier, *Electroweak radiative corrections for collider physics*, *Physics Reports* **864** (2020) 1.
- [75] S. Frixione, Z. Kunszt and A. Signer, *Three jet cross-sections to next-to-leading order*, *Nucl. Phys. B* **467** (1996) 399 [[hep-ph/9512328](https://arxiv.org/abs/hep-ph/9512328)].
- [76] F. Bloch and A. Nordsieck, *Note on the Radiation Field of the Electron*, *Phys. Rev.* **52** (1937) 54.
- [77] T. Kinoshita, *Mass Singularities of Feynman Amplitudes*, *Journal of Mathematical Physics* **3** (1962) 650 [<https://doi.org/10.1063/1.1724268>].
- [78] T.D. Lee and M. Nauenberg, *Degenerate Systems and Mass Singularities*, *Phys. Rev.* **133** (1964) B1549.
- [79] T. Mc Cauley, “Displays of tttt candidate events.” Image from CMS Collection. <https://cds.cern.ch/record/2680395>, Jun, 2019.
- [80] M. Cacciari, G.P. Salam and G. Soyez, *The anti- k_t jet clustering algorithm*, *JHEP* **04** (2008) 063 [[0802.1189](https://arxiv.org/abs/0802.1189)].
- [81] G.P. Salam, *Elements of QCD for hadron colliders*, in *2009 European School of High-Energy Physics*, 11, 2010 [[1011.5131](https://arxiv.org/abs/1011.5131)].
- [82] S. Frixione, *A General approach to jet cross-sections in QCD*, *Nucl. Phys. B* **507** (1997) 295 [[hep-ph/9706545](https://arxiv.org/abs/hep-ph/9706545)].
- [83] B. Webber, *Parton shower Monte Carlo event generators*, *Scholarpedia* **6** (2011) 10662.
- [84] B. Cabouat and T. Sjöstrand, *Some Dipole Shower Studies*, *Eur. Phys. J. C* **78** (2018) 226 [[1710.00391](https://arxiv.org/abs/1710.00391)].
- [85] B. Andersson, G. Gustafson, G. Ingelman and T. Sjöstrand, *Parton fragmentation and string dynamics*, *Physics Reports* **97** (1983) 31.
- [86] G. Marchesini, B. Webber, G. Abbiendi, I. Knowles, M. Seymour and L. Stanco, *HERWIG 5.1 - a Monte Carlo event generator for simulating hadron emission reactions with interfering gluons*, *Computer Physics Communications* **67** (1992) 465.

- [87] M.A. Dobbs et al., *Les Houches guidebook to Monte Carlo generators for hadron collider physics*, in *3rd Les Houches Workshop on Physics at TeV Colliders*, pp. 411–459, 3, 2004 [[hep-ph/0403045](#)].
- [88] S. Höche and S. Prestel, *Designing your parton shower simulation*, talk given at SLAC summer school in August 2016.
- [89] S. Frixione and B.R. Webber, *Matching NLO QCD computations and parton shower simulations*, *JHEP* **06** (2002) 029 [[hep-ph/0204244](#)].
- [90] K. Olive, *Review of particle physics*, *Chinese Physics C* **40** (2016) 100001.
- [91] M. Cepeda et al., *Report from Working Group 2: Higgs Physics at the HL-LHC and HE-LHC*, *CERN Yellow Rep. Monogr.* **7** (2019) 221 [[1902.00134](#)].
- [92] A. Bredenstein, A. Denner, S. Dittmaier and M.M. Weber, *Precise predictions for the Higgs-boson decay $H \rightarrow WW/ZZ \rightarrow 4$ leptons*, *Phys. Rev. D* **74** (2006) 013004 [[hep-ph/0604011](#)].
- [93] A. Bredenstein, A. Denner, S. Dittmaier and M.M. Weber, *Radiative corrections to the semileptonic and hadronic Higgs-boson decays $H \rightarrow WW/ZZ \rightarrow 4$ fermions*, *JHEP* **02** (2007) 080 [[hep-ph/0611234](#)].
- [94] M. Rauch, *Vector-Boson Fusion and Vector-Boson Scattering*, [1610.08420](#).
- [95] D. Zeppenfeld, *Collider physics*, in *Theoretical Advanced Study Institute in Elementary Particle Physics (TASI 98): Neutrinos in Physics and Astrophysics: From 10^{-33} to 10^{28} cm*, pp. 303–350, 2, 1999 [[hep-ph/9902307](#)].
- [96] T. Plehn, *Lectures on LHC Physics*, *Lect. Notes Phys.* **844** (2012) 1 [[0910.4182](#)].
- [97] F. Campanario, T.M. Figy, S. Plätzer, M. Rauch, P. Schichtel and M. Sjödal, *Stress testing the vector-boson-fusion approximation in multijet final states*, *Phys. Rev. D* **98** (2018) 033003 [[1802.09955](#)].
- [98] T. Liu, K. Melnikov and A.A. Penin, *Nonfactorizable QCD Effects in Higgs Boson Production via Vector Boson Fusion*, *Phys. Rev. Lett.* **123** (2019) 122002 [[1906.10899](#)].
- [99] F.A. Dreyer, A. Karlberg and L. Tancredi, *On the impact of non-factorisable corrections in VBF single and double Higgs production*, *JHEP* **10** (2020) 131 [[2005.11334](#)].
- [100] W. Buchmüller and D. Wyler, *Effective Lagrangian Analysis of New Interactions and Flavor Conservation*, *Nucl. Phys. B* **268** (1986) 621.
- [101] K. Hagiwara, S. Ishihara, R. Szalapski and D. Zeppenfeld, *Low-energy effects of new interactions in the electroweak boson sector*, *Phys. Rev. D* **48** (1993) 2182.

- [102] R. Contino, M. Ghezzi, C. Grojean, M. Muhlleitner and M. Spira, *Effective Lagrangian for a light Higgs-like scalar*, *JHEP* **07** (2013) 035 [1303.3876].
- [103] J. Baglio et al., *VBFNLO: A Parton Level Monte Carlo for Processes with Electroweak Bosons – Manual for Version 2.7.0*, 1107.4038.
- [104] J. Baglio et al., *Release Note - VBFNLO 2.7.0*, 1404.3940.
- [105] A. Buckley et al., *A comparative study of Higgs boson production from vector-boson fusion*, *JHEP* **11** (2021) 108 [2105.11399].
- [106] A. Denner, S. Dittmaier and J.-N. Lang, *Renormalization of mixing angles*, *JHEP* **11** (2018) 104 [1808.03466].
- [107] A. Denner and S. Pozzorini, *One loop leading logarithms in electroweak radiative corrections. 1. Results*, *Eur. Phys. J. C* **18** (2001) 461 [hep-ph/0010201].
- [108] J. Alwall, R. Frederix, S. Frixione, V. Hirschi, F. Maltoni, O. Mattelaer et al., *The automated computation of tree-level and next-to-leading order differential cross sections, and their matching to parton shower simulations*, *JHEP* **07** (2014) 079 [1405.0301].
- [109] J. Bellm et al., *Herwig 7.0/Herwig++ 3.0 release note*, *Eur. Phys. J. C* **76** (2016) 196 [1512.01178].
- [110] S. Höche, S. Mrenna, S. Payne, C.T. Preuss and P. Skands, *A Study of QCD Radiation in VBF Higgs Production with Vincia and Pythia*, *SciPost Phys.* **12** (2022) 010 [2106.10987].
- [111] B. Jäger, F. Schissler and D. Zeppenfeld, *Parton-shower effects on Higgs boson production via vector-boson fusion in association with three jets*, *JHEP* **07** (2014) 125 [1405.6950].
- [112] T. Ježo and P. Nason, *On the Treatment of Resonances in Next-to-Leading Order Calculations Matched to a Parton Shower*, *JHEP* **12** (2015) 065 [1509.09071].
- [113] G.P. Lepage, *A new algorithm for adaptive multidimensional integration*, *Journal of Computational Physics* **27** (1978) 192.
- [114] J. Alwall et al., *A Standard format for Les Houches event files*, *Comput. Phys. Commun.* **176** (2007) 300 [hep-ph/0609017].
- [115] J.M. Campbell, R.K. Ellis, R. Frederix, P. Nason, C. Oleari and C. Williams, *NLO Higgs Boson Production Plus One and Two Jets Using the POWHEG BOX, MadGraph4 and MCFM*, *JHEP* **07** (2012) 092 [1202.5475].
- [116] S. Honeywell, S. Quackenbush, L. Reina and C. Reuschle, *NLOX, a one-loop provider for Standard Model processes*, *Comput. Phys. Commun.* **257** (2020) 107284 [1812.11925].

- [117] T. Ježo, J.M. Lindert, P. Nason, C. Oleari and S. Pozzorini, *An NLO+PS generator for $t\bar{t}$ and Wt production and decay including non-resonant and interference effects*, *Eur. Phys. J. C* **76** (2016) 691 [1607.04538].
- [118] P. Nason, *Status of the POWHEG BOX*, talk given at ATLAS-CMS Monte Carlo Generators Workshop, January 11, 2016.
<https://indico.cern.ch/event/454993/contributions/1953124/attachments/1209273/1763261/MCwg-11-1-2016.pdf>.
- [119] C. Bernaciak and D. Wackerroth, *Combining NLO QCD and Electroweak Radiative Corrections to W boson Production at Hadron Colliders in the POWHEG Framework*, *Phys. Rev. D* **85** (2012) 093003 [1201.4804].
- [120] L. Barze, G. Montagna, P. Nason, O. Nicrosini and F. Piccinini, *Implementation of electroweak corrections in the POWHEG BOX: single W production*, *JHEP* **04** (2012) 037 [1202.0465].
- [121] L. Barze, G. Montagna, P. Nason, O. Nicrosini, F. Piccinini and A. Vicini, *Neutral current Drell-Yan with combined QCD and electroweak corrections in the POWHEG BOX*, *Eur. Phys. J. C* **73** (2013) 2474 [1302.4606].
- [122] M. Chiesa, A. Denner, J.-N. Lang and M. Pellen, *An event generator for same-sign W-boson scattering at the LHC including electroweak corrections*, *Eur. Phys. J. C* **79** (2019) 788 [1906.01863].
- [123] M. Chiesa, C. Oleari and E. Re, *NLO QCD+NLO EW corrections to diboson production matched to parton shower*, *Eur. Phys. J. C* **80** (2020) 849 [2005.12146].
- [124] G. Corcella, I.G. Knowles, G. Marchesini, S. Moretti, K. Odagiri, P. Richardson et al., *HERWIG 6: An Event generator for hadron emission reactions with interfering gluons (including supersymmetric processes)*, *JHEP* **01** (2001) 010 [hep-ph/0011363].
- [125] T. Gleisberg, S. Hoeche, F. Krauss, M. Schonherr, S. Schumann, F. Siegert et al., *Event generation with SHERPA 1.1*, *JHEP* **02** (2009) 007 [0811.4622].
- [126] T. Sjöstrand, S. Ask, J.R. Christiansen, R. Corke, N. Desai, P. Ilten et al., *An introduction to PYTHIA 8.2*, *Comput. Phys. Commun.* **191** (2015) 159 [1410.3012].
- [127] C. Bierlich et al., *A comprehensive guide to the physics and usage of PYTHIA 8.3*, 2203.11601.
- [128] S. Actis, A. Denner, L. Hofer, A. Scharf and S. Uccirati, *Recursive generation of one-loop amplitudes in the Standard Model*, *JHEP* **04** (2013) 037 [1211.6316].

- [129] S. Actis, A. Denner, L. Hofer, J.-N. Lang, A. Scharf and S. Uccirati, *RECOLA: REcursive Computation of One-Loop Amplitudes*, *Comput. Phys. Commun.* **214** (2017) 140 [1605.01090].
- [130] F. Berends and W. Giele, *Recursive calculations for processes with n gluons*, *Nuclear Physics B* **306** (1988) 759.
- [131] A. Denner, S. Dittmaier and L. Hofer, *Collier: a fortran-based Complex One-Loop Library in Extended Regularizations*, *Comput. Phys. Commun.* **212** (2017) 220 [1604.06792].
- [132] NNPDF collaboration, *Illuminating the photon content of the proton within a global PDF analysis*, *SciPost Phys.* **5** (2018) 008 [1712.07053].
- [133] A. Buckley, J. Ferrando, S. Lloyd, K. Nordström, B. Page, M. Rüfenacht et al., *LHAPDF6: parton density access in the LHC precision era*, *Eur. Phys. J. C* **75** (2015) 132 [1412.7420].
- [134] M. Cacciari and G.P. Salam, *Dispelling the N^3 myth for the k_t jet-finder*, *Phys. Lett. B* **641** (2006) 57 [hep-ph/0512210].
- [135] M. Cacciari, G.P. Salam and G. Soyez, *FastJet User Manual*, *Eur. Phys. J. C* **72** (2012) 1896 [1111.6097].
- [136] P. Skands, S. Carrazza and J. Rojo, *Tuning PYTHIA 8.1: the Monash 2013 Tune*, *Eur. Phys. J. C* **74** (2014) 3024 [1404.5630].
- [137] R. Frederix, S. Frixione, V. Hirschi, D. Pagani, H.S. Shao and M. Zaro, *The automation of next-to-leading order electroweak calculations*, *JHEP* **07** (2018) 185 [1804.10017].
- [138] J. Bellm et al., *Herwig 7.2 release note*, *Eur. Phys. J. C* **80** (2020) 452 [1912.06509].